Dual Role of Microglial TREM2 in Neuronal Degeneration and Regeneration After Axotomy

Tana S. Pottorf[1], Elizabeth L. Lane[1], Zoë Haley-Johnson[1], Desirée N. Ukmar[1], Veronica Amores- Sanchez[1], Patricia M. Correa-Torres[2], Francisco J. Alvarez[1*]

1 Department of Cell Biology, Emory University School of Medicine, Atlanta, GA, USA.

2 Department of Biology, University of Puerto Rico at Ponce, Puerto Rico.

*Corresponding author.

Francisco J. Alvarez, PhD
Department of Cell Biology
Emory University School of Medicine
Whitehead Research Building, Room 605D
615 Michael Street, Atlanta, GA, 30322-3110

Email: Francisco.j.alvarez@emory.edu

Keywords): Peripheral Nerve Injury, Motoneuron, Microglia, TREM2, CD68, Microglia morphology, Phagocytosis

Main Points (250 characters)

- TREM2 in activated microglia has a dual function around axotomized motoneuron cell bodies after peripheral nerve injuries.
- Within different microglia-motoneuron interactions, TREM2 is involved in the removal of degenerating motoneurons or facilitating regeneration.

Running Title: Microglia-Motoneuron Interactions After Peripheral Nerve Injury

Abbreviation Key: Central Nervous System (CNS), Motoneuron (MN), Peripheral Nerve Injury (PNI), Colony Stimulating Factor 1 (CSF1), CSF1- Receptor (CSF1-R), C-C chemokine receptor 2 (CCR2), Triggering Receptor Expressed on Myeloid Cells 2 (TREM2), DNAX activating protein of 12kDa (DAP12/*tyrobp*), externalized Phosphatidylserine (ePtdSer), 28 intraperitoneal (i.p.), lateral gastrocnemius (LG), Global Knockout (GKO), Conditional Knockout (CKO), Wildtype (WT), enhanced Green Fluorescent protein (eGFP), Immunohistochemistry (IHC), Adeno-Associated Virus serotype 1 tdTomato (AAV1-tdTom), postnatal day 5 (P5), Days Post Injury (dpi), paraformaldehyde (PFA), Phosphate Buffer Solution (PBS), Phosphate Buffer Solution with 0.03% Triton (PBST), artificial Cerebrospinal Fluid (aCSF), Region of Interest (ROI), Neuromuscular Junction (NMJ), α-Bungarotoxin (α-BTx), phosphorylated Spleen Tyrosine Kinase (p-SYK), Weeks Post Injury (wpi), Disease-Associated Microglia (DAM), Choline Acetyltransferase (ChAT), Neuronal Nuclei (NeuN), Kolmogorov-Smirnov (K-S), Neurofilament Heavy Chain (NFH), Vesicular Acetylcholine Transporter (VAChT), alpha Bungarotoxin (α-BTx), Cumulative-Summation (Cum-Sum)

Abstract

After nerve injuries, microglia proliferate and migrate towards injured motoneurons, where they attach to the cell bodies. The significance of microglia enwrapping of axotomized motoneurons remains unclear. We found that within the same motor pools, some motoneurons degenerate while others regenerate, and each is associated with different microglia phenotypes and interactions. Microglia surrounding degenerating motoneurons form tight cell clusters ("death clusters") that fully envelop the cell body and express high TREM2 and large CD68 granules, suggesting a macrophagocyte phenotype. Microglia surrounding motoneurons during the regeneration process are individualized and upregulate TREM2 and CD68; however, the CD68 granules are smaller. These microglia extend processes that scan the motoneuron surface through sweeping motions, sampling contents, and likely incorporating components through microphagocytosis. Removal of TREM2, either globally throughout development or specifically in microglia prior to nerve injuries, reduces p-SYK signaling and CD68 expression in all activated microglia, but with a sex effect: CD68 downregulation is significant in females, but not in males. Lack of TREM2 also prevents motoneuron cell body swelling (in both sexes), characteristic of the early chromatolytic reaction at the start of regeneration. This correlates with delays in muscle reinnervation. We conclude that within the same motor pools, TREM2 directs some microglia to remove degenerating motoneurons while it facilitates the regenerative phenotype of other motoneurons. The signals that direct these different microglia phenotypes over degenerating and regenerating motoneurons, as well as the mechanisms that induce degeneration in some motoneurons while most others regenerate, remain to be investigated.

Introduction

Microglia were initially defined as the phagocytic cells of the Central Nervous System (CNS) in the pioneering studies of del Río-Hortega, but thereafter these cells remained largely unexplored for almost 50 years (see review (Sierra et al., 2016). This changed after the landmark paper by Blinzinger and Kreutzberg (Blinzinger & Kreutzberg, 1968) that reported microglia proliferation and enwrapping of facial motoneurons (MNs) after axotomy following injuries to the facial nerve. They proposed that local activation of microglia in the CNS after a distal peripheral nerve injury (PNI) is a protective mechanism that works through the removal of synapses from the cell bodies of injured MNs. This phenomenon was named “synaptic stripping” because microglia processes were observed interposed between the MN surface and synaptic boutons without synaptic engulfment. Recent studies extended this idea, showing that microglia are widely involved in synaptic pruning during normal developmental circuit refinement and in disease (Hong et al., 2016; Pereira-Iglesias et al., 2025; Piccioni et al., 2021; Rajendran & Paolicelli, 2018; Stevens et al., 2007; Wilton et al., 2019). By contrast to “synaptic stripping”, microglia synapse deletions were frequently reported to occur through complement tagging and synapse phagocytosis, although removal by trogocytosis has been also reported more recently (Vecchiarelli et al., 2024; Weinhard et al., 2018). Even though microglia synapse deletion mechanisms have been thoroughly studied and are well-accepted, the original hypothesis that microglia are involved in the removal of synapses from the cell bodies of axotomized MNs has now been challenged (Berg et al., 2013; Rotterman et al., 2024; Salvany et al., 2021; Svensson & Aldskogius, 1993b). This hypothesis was derived from electron microscopy observations that could not prove causality, while more recent studies using modern methods to interfere with microglia activation after PNI demonstrated that the microglia reaction is not necessary for “synaptic stripping” to occur. This raises important new questions about the significance of microglia surrounding the cell bodies of MNs whose axons are severed after PNI.

Many studies have studied microglia-neuron communication throughout many CNS regions in the context of development, aging, health, and disease (Szepesi et al., 2018). In healthy tissue, microglia are highly dynamic and extensively survey their microenvironments, including frequent contacts with neighboring neurons to assess the neuronal health state (Cserép et al., 2020; Nimmerjahn et al., 2005). Microglia support of neurons can occur through release of trophic factors (Bruce-Keller, 1999; Lai & Todd, 2008) or by cell-cell contacts that modulate metabolic homeostasis in neurons (Cserép et al., 2020; Tagliatti et al., 2024). Further, microglia have been shown to selectively kill and/or remove injured, stressed or dying neurons

during development and disease. They can directly promote apoptosis or be deleterious to neuron survival by enhancing neuroinflammation (Bilimoria & Stevens, 2015; Brown, 2024; Brown & Vilalta, 2015; Butler et al., 2021; Chen et al., 2025; Gibbons & Dragunow, 2006; Marin-Teva et al., 2024). Thus, previous literature emphasizes the importance, heterogeneity, specificity, and intentionality of microglia-neuron interactions in health, disease, or following an injury. These findings prompted us to re-investigate microglia-MN interactions after PNI, beyond "synaptic stripping".

Our previous studies examined microglia mechanisms around spinal MNs sxotomized following different types of injuries to peripheral nerves. Briefly, axotomized MNs upregulate Colony Stimulating Factor 1 (CSF1) that directs both microglia proliferation and the length of time microglia remain activated around injured MNs; more severe injuries inducing prolonged activation (Rotterman et al., 2019; Rotterman et al., 2024). Longer microglial activation, which occurs after nerve transections, promotes microglia to switch towards proinflammatory phenotypes including expression of C-C chemokine ligand 2 (CCL2). We showed that microglia CCL2 is necessary for the removal from the ventral horn of the central axons and synapses of proprioceptive afferents whose peripheral axons are injured in the nerve (Rotterman et al., 2024). The loss of proprioceptive sensory afferents in the ventral horn deprives MNs and premotor circuits of critical proprioceptive information preventing full motor recovery after successful regeneration of peripheral nerves (Alvarez et al., 2010; Alvarez et al., 2020). These previous studies did not specifically address the role of microglia surrounding the cell bodies of MNs but demonstrated that the ventral horn microglia reaction includes a variety of microglia phenotypes that are dynamically regulated by the severity of the injury and the time it takes for MNs to regenerate and reinnervate muscle. Specifically, we reported two distinct microglia-MN interactions after nerve transection injuries (Rotterman & Alvarez, 2020). More commonly, microglia migrate towards the cell bodies of MNs that are in the process of regenerating and surround them. A second, more infrequent, phenotype consists of tight cell clusters of ameboid microglia with retracted processes, which completely surround degenerating MNs. These "death clusters" are common after nerve transections and attract cytotoxic T-cells (CD8+) (Rotterman & Alvarez, 2020). The signals and mechanisms that regulate these two types of microglia-MN interactions and, therefore MN fates, regeneration, or degeneration, are unknown.

We focused on Triggering Receptor Expressed on Myeloid Cells 2 (TREM2) because it was first reported to modulate neuronal phagocytosis by microglia in the absence of inflammation (Takahashi et al., 2005). Additionally, the expression of DNAX Activation Protein of 12 kDa (DAP12), a protein essential for TREM2 signal transduction, is known to be increased

by CSF1 after PNI (Guan et al., 2016). Recently, research has expanded on microglial TREM2/DAP12 mechanisms to include roles in synapse deletion (Filipello et al., 2018; Jay et al., 2019; Matteoli, 2024; Rueda-Carrasco et al., 2023; St-Pierre et al., 2020; Vecchiarelli et al., 2024; Zhong et al., 2023) and providing metabolic support to active microglia and neurons (Tagliatti et al., 2024), in both healthy and diseased states. These functions are crucial for the regeneration and degeneration of MNs following PNI. Therefore, we hypothesized that TREM2, which is known to bind externalized phosphatidylserine (ePtdSer), an “eat me” signal (Rueda-Carrasco et al., 2023; Scott-Hewitt et al., 2020; Shirotani et al., 2019), may orchestrate the switch of microglia properties around regenerating or degenerating MNs. However, our findings turned out to be depict a more complex picture. TREM2 expression increased in activated microglia after PNI, and more so in microglia associated with dying MNs. Still, TREM2 deletion (either globally or specifically in microglia) did not prevent the formation of death clusters or microglia associations with regenerating MNs, although it modulated microglial phagocytic phenotypes in a sex-specific manner. Additionally, TREM2 deletion abolished cellular changes in MNs associated with regeneration (cell body swelling) and delayed muscle reinnervation in both sexes. In conclusion, TREM2 is a key signal that modulates different types of microglia interactions with axotomized MNs, either by promoting regeneration in some MNs or aiding the removal of others that degenerate after PNI. Our work highlights the complexity of TREM2 as a therapeutic target for PNI, which may be translatable to other Motor Neuron diseases.

Materials and Methods

Ethical Statement

All animal procedures were approved by the Institutional Animal Care and Use Committee at Emory (Protocol #201700620) and followed the NIH Guidelines for the use of animals in research. All animal procedures, analyses, and husbandry were performed at Emory University. We followed the ARRIVE guidelines in experimental design and performance.

Experimental Animals

All animals used in this manuscript were from a mixed background (C57Blk/6 J/N). The C57BL/6-Tmem119^{em2Gfng}/J and C57BL/6J- TREM2^{em2Adiuj}/J mice were bred to create a global TREM2 knockout (GKO) mouse with microglia-specific eGFP labeling. The C57BL/6-Tmem119$^{em1(cre/ERT2)Gfng}$/J, C57BL/6J-Trem2$^{tm1c(EUCOMM)Wtsi/Adiuj}$/J, and B6.Cg-Gt (ROSA)

$^{26Sortm9(CAG\text{-}tdTomato)Hze}$/J were bred to create a Tmem119-2A-CreERT2:: TREM2 flox/flox:: Rosa26 tdTomato mouse in which Tmem119-specific microglia were labeled with tdTomato only when TREM2 has been knocked out following tamoxifen injections (conditional knockout: CKO). *B6.129P-Cxcr1^{tm1Litt}/J* mice were bred as heterozygotes. All other mice were bred in homozygosis. Genetic mouse lines and their usage in this study are summarized in **Table 1**. We found no significant difference in the number of ventral horn microglia labeled with IBA1 versus CX3CR1^{eGFP} versus Tmem119^{eGFP} 14 days post sciatic cut-ligation (data not shown), allowing us to confidently use different microglia labels in a methodology-specific manner. Mice were housed with littermates, standard chow, and 12-hour light-dark cycles. CKO mice were housed on static racks following tamoxifen injection. All other mice were housed on auto-water racks.

Table 1. Genetic Mouse Lines

Mouse	The Jackson Laboratory stock #	Description	Usage
B6.129P-Cxcr1^{tm1Litt}/J	005582	These mice have an enhanced green fluorescent protein (eGFP) construct knocked into a coding region of the chemokine receptor “CX3CR1” gene to create a loss of function allele.	Used for 2P live time-lapse imaging and RNAscope experiments
C57BL/6-Tmem119^{em2Gfng}/J	031823	These mice have an enhanced green fluorescent protein (eGFP) reporter gene following a 2A ribosomal skipping signal after the coding region of the transmembrane protein 119 (Tmem119), a microglial specific membrane protein.	Used for IHC experiments
C57BL/6-Tmem119$^{em1(cre/ERT2)Gfng}$/J	031820	These mice have a tamoxifen-inducible cre-ERT2 recombinase inserted following a 2A ribosomal skipping after the coding region of Tmem119.	Used to create TREM2 CKO mouse for IHC experiments

C57BL/6J-Trem2$^{tm1c(EUCOMM)Wtsi/Adiuj}$/J	029853	These are floxed mutant mice with loxp2 sites flanking exons 2 and 3 of TREM2.	Used to create TREM2 CKO mouse for IHC experiments
B6.Cg-Gt (ROSA)$^{26Sortm9(CAG-tdTomato)Hze}$/J	007909	These Ai9 Cre reporter mice are designed to be bred to mice that express a Cre recombinase. The resulting offspring allow expression of the red fluorescent protein variant tdTomato in Cre expressing cells.	Used to create TREM2 CKO mouse for IHC experiments
C57BL/6J-TREM2^{em2Adiuj}/J	027197	These mice have a global TREM2 knock out via a 175 base pair deletion that introduces and early stop code at amino acid 17.	TREM2 GKO for IHC experiments

Tamoxifen Injections

To induce cre recombination, CKO mice were injected with Tamoxifen (Sigma Aldrich, cat: T5648) once daily for five consecutive days starting at postnatal day 28 (intraperitoneal (i.p.) 2 mg/kg, diluted in corn oil (Ward's Science, cat: 470200-112).

Intramuscular Injections for Retrograde Motoneuron Labeling

For all survival surgeries, mice were anesthetized via isoflurane inhalation (4% induction and 2% maintenance) and injected prior to surgery with 0.05 mg/kg buprenorphine subcutaneously to diminish postoperative pain. The left lateral gastrocnemius (LG) muscle was exposed and targeted for injections. For two-photon studies, 1 μL of Adeno-Associated Virus serotype 1 tdTomato (AAV1-tdTom) (Addgene, plasmid #59462) was pressure-injected at postnatal day 5 (P5) using a pulled glass micropipette. For histological studies, 4 μL of 2% Fast Blue (Polyscience, cat# 17740-1) was injected using a 25G Hamilton syringe in two-month-old animals. Skin wounds were closed with Vetbond®, both in neonates and adults.

Sciatic Cut Ligation and Sham Surgeries

Adult mice received nerve surgeries between two to four months of age. When Fast Blue intramuscular injections were used, a minimum of five days was waited before performing nerve

surgeries to allow time for tracer retrograde transport of the tracer. A skin incision was made in the medial left thigh, parallel to the femur. Then the biceps femoris was retracted by blunt fascia dissection to expose the sciatic nerve. The sciatic nerve was isolated and either left intact (sham surgery) or ligated with a 5-0 non-absorbable suture and cut distally (cut-ligation). The muscle was reconnected with absorbable 5-0 sutures, and the skin was closed with non-absorbable 5-0 sutures and Vetbond®. Anesthesia (isoflurane) and analgesia (buprenorphine) were as above.

Sciatic Cut Repair With or Without Fast Blue Nerve Soak

Mice used in time course experiments underwent sciatic nerve cut-repair surgeries, at which time the cut nerve was soaked with Fast Blue. The sciatic nerve was exposed at the mid-thigh in two to four-month-old mice and then partially lifted to insert a 1 mm^2 silastic scaffolding matrix (Dow Corning #501-1) underneath. Fibrin Glue (Akhter et al., 2019) was added to the nerve on the scaffolding mesh and allowed to harden. The nerve was then transected with fine surgical scissors. Fibrin Glue maintained alignment between the nerve stumps, and at this time, 1 μL of 2% Fast Blue was added to the exposed nerve stumps. Additional Fibrin Glue was added on top of the transected nerve before closing. Muscles and skin were repaired and closed as above. Anesthesia (isoflurane) and analgesia (buprenorphine) were as above.

Transcardial Perfusion and Tissue Collection

Mice were anesthetized with a terminal dose of Euthasol (100 mg/kg) at 3, 7, 14, 21, or 28 days post-injury (dpi) and transcardially perfused with 5 mL of heparin pre-perfusion rinse followed by 15 mL of 4% paraformaldehyde (PFA) prepared in 0.1M phosphate buffer (pH=7.4). The spinal cords were harvested and placed in 4% PFA for post-fixation. Spinal cord tissues used for immunohistochemistry were post-fixed for four hours at 4°C, followed by a minimum of 24 hours in 30% sucrose. Spinal cord tissue used for RNAscope was post-fixed for 24 hours at 4°C, followed by 24 hours in 10% sucrose, 24 hours in 20%, and 24 hours in 30% sucrose. Muscle tissue was post-fixed for 4 hours at 4°C, followed by 24 hours in 10% sucrose, 24 hours in 20%, and 24 hours in 30% sucrose.

Immunohistochemistry and Confocal Microscopy

Transverse sections (50 μm thick) from the Lumbar 3 (L3) to the L6 segment were obtained on a freezing sliding microtome and collected free-floating. Free-floating sections were subjected to a one-hour block in 10% Normal Donkey Serum diluted in 0.01M Phosphate Buffer Solution with 0.03% Triton (PBST). The sections were then incubated in different mixtures of

primary antibodies, all diluted in PBST. Primary antibody incubations were carried out overnight at room temperature. The following day, immunoreactive sites were revealed with species-specific secondary antibodies (2-3 hours at room temperature), and after washes in PBS, the sections were mounted on glass slides and cover-slipped with Vectashield with DAPI (Vector Labs, H-1200-10), or without (Vector Labs, H-1000-10). Details of antibodies used, and their concentrations are listed in **Table 2**. Confocal microscopy was performed with 10X (NA 0.4), 20X (NA, 0.7), and 60X (oil, NA 1.35) objectives in a Fluoview FV1000 Olympus microscope. All images were 1024X1024 pixels in size. Digital zoom and z-step sizes varied depending on experiments. Antibody combinations and imaging conditions are described in each analysis.

Table 2. Antibodies and Dyes Used for Immunohistochemistry

Antibody Name	Host	Company	Catalog Number	Dilution	RRID
Anti-eGFP	Chicken	Aves	GFP-1020	1:100	AB_10000240
Anti-TREM2	Sheep	R&D Systems	AF1729	1:100	AB_354956
Anti-CD68	Rat	abcam	AB53444	1:100	AB_869007
Anti-Ki-67	Mouse	BD Biosciences	550609	1:100	AB_393778
Anti-IBA1	Rabbit	FUJIFILM Wako Pure Chemical Corporation	019-19741	1:1000	AB_839504
Anti-VAChT	Guinea Pig	Synaptic Systems	139105	1:500	AB_10893979
Anti-NFH	Chicken	Aves	NFH	1:500	AB_2313552
FITC coupled anti-chicken IgY	Donkey	Jackson ImmunoResearch	703-095-155	1:100	AB_2340356
Cy3 conjugated	Donkey	Jackson ImmunoResearch	703-165-155	1:100	AB_2340363

anti-chicken IgG					
Cy5 conjugated anti-chicken IgY	Donkey	Jackson ImmunoResearch	703-175-155	1:100	AB_2340365
Cy5 coupled anti-sheep IgG	Donkey	Jackson ImmunoResearch	713-175-147	1:100	AB_2340730
Cy3 couple anti-rat IgG	Donkey	Jackson ImmunoResearch	712-165-153	1:100	AB_2340667
Cy3 coupled anti-mouse IgG	Donkey	Jackson ImmunoResearch	715-165-150	1:100	AB_2340813
Cy5 coupled anti-mouse IgG	Donkey	Jackson ImmunoResearch	715-175-150	1:100	AB_2340819
FITC conjugated anti-Guinea Pig IgG	Donkey	Jackson ImmunoResearch	706-095-148	1:100	AB_2340453
Cy3 conjugated anti-Guinea Pig IgG	Donkey	Jackson ImmunoResearch	706-165-148	1:100	AB_2340460
Cy5 conjugated anti-Guinea Pig IgG	Donkey	Jackson ImmunoResearch	706-605-148	1:100	AB_2340476

α Bungarotoxin- 488	-	Invitrogen	B13422	1:100	-
α Bungarotoxin- 647	-	Invitrogen	B35450	1:100	-

Microglia Sholl Analysis

Tmem119^{eGFP} microglia associated with Fast Blue retrogradely labeled MNs were imaged with confocal microscopy (60x 2x digital zoom, 0.5 μm step size) in animals with sham or sciatic nerve cut and ligation surgeries (N=6 shams and 6 injured, equal sex). We divided microglia into four groups according to location: microglia close to retrogradely labeled MNs in animals with 1) sham surgeries or the 2) contralateral spinal cord in animals with nerve injuries, and two locations in the ipsilateral spinal cord, 3) those associated with injured Fast Blue+ motoneurons ("On MN" microglia) and 4) those in death clusters (DC microglia). Note, from here on, "death cluster" will refer to the cluster, and "DC" as the individual microglia. In each animal, we analyzed five microglia per condition (sham, contralateral, On MN, or DC). Individual microglia were semi-automatically traced and skeletonized in IMARIS by thresholding the fluorescent eGFP signal, followed by cell isolation and 3D reconstruction using the filament tracer module (n=5 microglia per animal, 30 per experimental condition). Sholl analyses for microglia processes transecting at 10 μm distance spheres were performed in IMARIS.

Ex Vivo Spinal Cord Slice Preparation and Two-Photon Time Lapse Imaging

Mice were injected with a terminal dose of Euthasol (i.p. 100 mg/kg) and decapitated once they reached a deep plane of anesthesia (unresponsive to tail and paw pinch and no corneal reflex). The animal's back, including rib cage, back muscles, vertebrae, and spinal cord, was removed and transferred to chilled dissecting artificial Cerebrospinal Fluid (aCSF, see formulation in **Table 3**) bubbled with carbogen (95% O_2 and 5% CO_2) for 30 minutes, and then L-ascorbic acid, ethyl pyruvate, and calcium chloride added after bubbling and before use. The solutions were adjusted to pH 7.2 and 355 mOsm. The vertebral column was excised to expose the spinal cord, which was then carefully lifted by dissecting the spinal roots and meninges. Lumbar spinal cord segments 3 through 5 (L3-L5) were blocked and embedded in 2% UltraPure

Low Melting Point Agarose (Invitrogen, cat#16520-100) and placed on a vibratome stage, covered with dissecting aCSF to obtain 300 µm-thick sections. Individual sections were transferred to 30% Polyethylene glycol for 60 seconds, and then to room temperature in imaging aCSF (see formulation in **Table 3**) that was also bubbled with carbogen and prepared like dissecting aCSF. Sections were allowed to acclimate to the imaging aCSF for 15 minutes before being placed in the imaging chamber. Two-photon time-lapse recordings were taken on a Leica SP8 Multi-Photon microscope using a HC-Fluotar-L 25x/0.95 N.A. water objective. The fluorochromes were excited with a Coherent Chameleon Vision II pulse-laser laser tuned to 980 nm and at 2–5% strength to optimally excite eGFP and tdTomato simultaneously with minimal bleaching during time-lapse imaging. Fluorescent signals were acquired through two non-descanned gallium-arsenide HyD detectors in BrightR mode positioned at the back focal plane of the objective for maximum brightness. eGFP and tdTomato fluorescence were separated by a dichroic mirror, and each signal was further selected by emission filters of appropriate wavelengths before reaching the detector. In our image setup, there was extensive eGFP fluorescence entering the tdTomato channel, and therefore, microglia were pseudocolored in white. This also permitted a better definition of small processes. We used a 4.5-7.5x digital zoom and 512X512 pixels images to optimize visualization of microglia-MN interactions while minimizing scanning time; therefore, fields of view were generally small. To capture whole microglia volumes, we used a 1 µm step-size and z-stacks varied between 30 and 80 optical planes, resulting in 1-1.30 minute temporal resolution for each frame after optimizing dwell times and bi-directional line scanning (faster scanning times with minimal loss of intensity). Time-lapses lasted between 30 to 90 minutes, and several fields were imaged in individual sections for three to four hours, or until there were signs of neuronal damage or microglial morphology changes. Recordings were visualized in 4D using IMARIS. All animals were analyzed 14 days post-surgery (shams, N= 3 male, 3 female; or sciatic nerve cut and ligation, N= 6 male, 3 female).

Table 3. Formulation for dissection and imaging artificial cerebral spinal fluid (aCSF) solutions.

Dissecting aCSF	**Imaging aCSF**
65.379 g/L Sucrose	7.07 g/L Sodium Chloride
3.6 g/L Dextrose	2.7 g Dextrose
0.21 g/L Kynerenic Acid	0.172 g/L Sodium Phosphate
0.176 g/L K-Gluconate	2.1 g/L Sodium Bicarbonate

0.170 g/L Potassium Phosphate	0.22 g/L Potassium Chloride
5.2 ml/L 80% Choline Bicarbonate	0.224 g/L Magnesium Chloride
0.986g/L Magnesium Sulfate	0.540 g/L Myo-inositol
0.540 g/L Myo-inositol	1.80 g/L D-glucose
1.80 g/L D-glucose	1 ml/L 1M L-ascorbic acid
1 ml/L 1 M L-ascorbic acid	5 ml/L 98% ethyl pyruvate
5 ml/L 98% ethyl pyruvate	1 ml/L 1M Calcium chloride
1 ml/L 1 M Calcium chloride	

Analysis of TREM2 Immunofluorescence

TREM2 immunofluorescence was performed in Tmem119^{eGFP} mice with Fast Blue MNs retrogradely labeled from the LG muscle (N=8 sham and 8 with sciatic-nerve injury and ligation; equal sex). Animals were analyzed 14 days after surgery. Confocal z-stack images were taken from the triple fluorescent sections with Fast Blue MNs, eGFP microglia (amplified with antibodies), and TREM2 immunofluorescence (Cy5) using the 60x objective, 2x digital zoom, and 1 μm step size. We imaged between 20 to 26 sham, contralateral, and On MN microglia per animal. Fewer DC microglia were sampled per animal. TREM2 protein signal-to-noise ratio was calculated by examining each optical plane through the z-stack and identifying the location of the microglia cell body mid-cross section and where TREM2 is most intense in both the membrane and also juxtanuclear in the Golgi (Sessa et al., 2004). A Region of Interest (ROI) was drawn around the membrane using ImageJ and excluding the strongly stained Golgi. A same-sized ROI was sampled in a background area near each microglia. In each ROI we measured average fluorescence intensity. To estimate the cell body fluorescence intensity over background fluorescence, we use the formula: (sample – background)/(background). Individual microglia outlier estimates were identified via the ROUT method (Q=1%) and removed. If any animal average was considered an outlier, the entire animal was removed from the analyses. The resulting sample sizes are shown in **Supplemental Statistical Table 2**.

To confirm TREM2 protein absence in GKO and CKO mice, we used the same method, microglia identification was also supported by immunolabeling with IBA1 antibodies.

CX3CR1 *trem2* RNAscope Co-detection and Analysis

RNAscope multiplex fluorescent v2 assay (ACDBio, Cat:323100) was performed in CX3CR1^{eGFP} animals and combined with eGFP immunofluorescence-integrated co-detection

workflow on fixed-frozen tissue sections according to the suggested Advance Cell Diagnostics protocol (acdbio.com). Isolated tissues were fixed and cryoprotected as explained above, and then 16µm- thick cryostat sections were obtained from L3 to L5 segments, collected on slides, air-dried, and kept at -20°C until use. The reagents used to perform RNAscope were as follows: RNAscope Intro Pack for Multiplex Fluorestcent Reagent Kit v2- Mm (ACDBio, Cat: 323136), RNA-Protein Co-detection Ancillary Kit (ACDBio, Cat:323180), RNAscope probe-Mm-TREM2 (ACDBio, Cat: 404111), Opal 570 Reagent Pack (Akoya Bioscience, Cat: FP1488001KT). Endogenous eGFP was amplified with primary antibody, chicken anti-eGFP (Aves, 1:50 dilution), and secondary antibody, FITC anti-chicken IgY (1:50 dilution). The sections were mounted with Prolong Gold (Invitrogen, Cat: P36980) and DAPI for nuclei identification. These animals did not contain Fast Blue-labeled MNs; therefore, analyses were directed to known locations of the sciatic motor pool in lumbar 3-5 sections (N=4 sham (equal sex) and 5 sciatic nerve cut and ligation (2 male and 3 female). Animals were analyzed 14 days after surgery.

Microglia at all four locations (sham, contralateral, On MN, and DC) were imaged at 60x, 2x zoom, and 0.5 µm z-steps. Due to the thin tissue section thickness, entire microglia visualization within one section rarely occurs. Microglia were sampled for quantification if the cell body, nucleus, and a couple of processes were visible. *trem2* signal consisted of clumps of individual dots (each supposedly a single mRNA), which were frequently difficult to individualize. Therefore, in IMARIS we obtained the total volume of *trem2* signal and normalized it to the "whole" eGFP microglia volume imaged or the DAPI nucleus volume. In death clusters, it was not possible to individualize microglia, and therefore, *trem2* occupancy of cytoplasm and processes was calculated against the whole death cluster. Therefore, n values for DC microglia were smaller in these comparisons. DAPI-labeled nuclei in DC microglia were easily individualized and thus n is larger. Individual microglia outliers were removed via the ROUT method (Q=1%), and if any animal average was considered an outlier, the entire animal was removed from analyses. The final sample sizes for statistical comparisons are reported in **Supplemental Statistical Tables 4, 5, and 6**.

To confirm *trem2* mRNA absence in GKO and CKO mice, we used the same method except that in this case, microglia were immunolabeled with IBA1 antibodies in GKO mice and genetically with tdTomato in CKO. The tdTomato signal was amplified with antibodies.

P-Syk Immunofluorescence Analysis

In this case, we compared WT (Tmem119^{eGFP}), GKO, and CKO animals that underwent sham or sciatic cut and ligation surgeries and were analyzed 14 days after. We analyzed the following experimental groups: Sham: N=4 WT (4 female), 6 GKO (4 male, 2 female), and 5 CKO (2 male, 3 female); PNI: N=6 WT (4 male, 3 female), 5 GKO (3 male, 2 female) and 7 CKO (4 male, 3 female). In this case, all animals contain Fast Blue MNs retrogradely labeled from the LG muscle. Microglia were detected with eGFP (Tmem119^{eGFP} in WT and GKO) or tdTomato (Tmem119^{CreERT2}:Ai9tdTomato in the CKO). eGFP was amplified with immunohistochemistry in its respective green channel. p-SYK was detected with phosphorylation-specific antibodies (see **Table 2**) in the Cy5 channel. Multiplex fluorescence sections were imaged with confocal microscopy (60x objective, 2x zoom, 1 μm step size), and 17-20 microglia per condition/genotype were randomly selected for quantification. The membrane of each microglia was manually traced in ImageJ, and the traced line width was set to 5 pixels (or ~0.5 μm, wide, images were approximately 0.1 μm/pixel). The integrated pixel density under the line and a similar line was placed outside each cell to obtain a value for the background. Signal-to-noise ratios were calculated thereafter as explained for TREM2 immunofluorescence quantification. Individual microglia outliers were removed via the ROUT method (Q=1%). If the animal average was considered an outlier, the entire animal was removed from the analysis. Final sample sizes are described in **Supplemental Statistical Table 7**.

Ventral Horn Microglia Number and Territories in Sham Animals

For this analysis, we used N=7 WTs (3 male, 4 female), 7 GKO (4 male, 3 female), and 5 CKO mice (1 male, 4 female). Microglia were genetically labeled by eGFP (Tmem119^{eGFP} in WT and GKO) or tdTomato (Tmem119^{CreERT2}:Ai9tdTomato in the CKO). eGFP was amplified with antibodies against its fluorescent protein. For each animal, we imaged five randomly chosen L5 sections with confocal microscopy and a 10x objective, 1x zoom, and 2 μm z-step. Only the ventral horn ipsilateral to the sham surgery was imaged. Analyses were performed in ImageJ on the collapsed z-stack confocal images (Jay et al., 2019). The ventral horn was outlined by tracing a horizontal line from the top of the central canal and outlining the gray-white matter border. Within this ROI, individual microglia were identified and counted using the multi-point selection tool. The ROI area was measured, and a volume was obtained by multiplying by section thickness (50 μm). From here, we calculated the average number of microglia within a volume cube of 100 μm side (10^6 μm^3) and obtained an average for each animal (n=5 sections per animal). Microglia territories were identified with the ImageJ Voronoi plugin and

pseudocolored for optimal definition. The average area of Voroni territories was calculated for each animal (n=five L5 sections per animal). No outliers were identified via the ROUT method (Q=1%). Exact sample sizes are reported in **Supplementary Statistical Tables 8 and 9**.

Time course of microglia proliferation and TREM2 expression in WT, GKO, and CKO

These analyses were performed in animals that underwent a sciatic-nerve cut and repair injury to allow regeneration and analyze microgliosis at 3-, 7-, 14-, 21-, and 28-days post-injury (dpi). N=4 mice (equal sex) per condition (time after injury/genotype) except for CKO animals at 21 dpi, in which N=2 females. All animals received a Fast Blue nerve soak at the axotomy location such that all axotomized MNs were retrogradely labeled. Serial sections were immunolabeled with Ki-67 or TREM2 antibodies in the Cy5 channel. Microglia were genetically labeled and fluorescent signals amplified with antibodies against eGFP (Tmem119^{eGFP} in WTs and GKO). For microglia cell counts, we obtained confocal images from five random L5 sections with a 20x objective, 1x zoom, and 1 µm z-step. Microglia were manually identified and counted in Neurolucida. Animal averages were obtained from five L5 sections per animal.

Ki-67 analysis was performed in the same sections. In this case, Ki-67 nuclear immunoreactivity was identified by a naïve observer blinded to the animal conditions, and a percentage of the total microglia detected was obtained for each section. Animals' averages were obtained from five L5 sections per animal. Further analyses re-classified microglia according to location: On MN, in death clusters, in the white matter, and not contacting MNs in the gray matter (different from On MN and DC microglia). Percentages of Ki-67+ cells for each microglia category were calculated.

TREM2 quantification was performed in WT cut-repair animals following the same method explained above (**Figure 3, Supplemental Statistical Table 3**).

Number of Death Clusters comparison in WT, GKO, and CKO.

We used the same time course mice to compare the number of death clusters at 3-, 7-, 14-, 21-, and 28-dpi. In addition, we compared the 14-dpi cut-repair time point with animals that underwent sciatic nerve cut and ligation surgery with no regeneration allowed. The data were compiled from animals used in previous analyses; N=12 WT, 12 GKO, and 8 CKO, all of equal sex. An independent observer used a 20x objective on an Olympus BX60 epifluorescent microscope coupled to a RealTime Digital camera to count all death clusters throughout all recovered sections of the entire lumbar spinal cord in each animal. Only sections with microgliosis were counted. Quantification occurred blind to genotype and on serial sections to

ensure death clusters were not double-counted or biased. The number of death clusters was divided by the number of sections to obtain a value per 50 µm-thick section in each animal. This value was multiplied by 100 to estimate the number of death clusters contained within 5 mm of rostro-caudal spinal cord length corresponding to the distribution of the lumbar region containing sciatic MNs from L4 to L6 segments.

Microglia morphologies in GKO mice

We reconstructed microglia morphologies for Sholl analyses as described above. N=6 animals and 5 microglia/animal reconstructed and skeletonized for each location: sham, contralateral, On MN and DC microglia (n=30 microglia per experimental condition). In this case, the nerve injury was a sciatic nerve cut and ligation, and the analyses were performed at 14 dpi. Microglia tracings underwent Sholl analyses (as above), and at each microglia location, data from GKO were compared to WT microglia data from **Figure 1**.

Microglia-Motoneuron Interactions

The number of microglia cells contacting a MN or composing a death cluster was quantified by randomly selecting seven to ten Fast Blue-labeled MNs or up to ten death clusters per animal in 60x confocal images. To be selected, the entire MN and/or death cluster had to be visible within one confocal z-stack, which limited the total quantifiable MNs/death clusters. Not every animal had seven or more death clusters, so in those cases, we quantified as many as were present. The number of microglia was manually quantified by going plane-by-plane through the z-stack by a naïve observer blinded to experimental conditions and genotype. No outliers were identified via the ROUT method (Q=1%). Final numbers of sampled MNs and death clusters are reported in **Supplementary Statistical Table 14**.

CD68 Quantification

We compared WT and GKO animals that underwent sham or sciatic cut and ligation surgeries and were analyzed 14 days after. We analyzed the following experimental groups: Sham: N=8 WT (equal sex), 7 GKO (4 male/ 3 female); PNI: N=7 WT (4 male / 3 female), 5 GKO (4 male / 4 female). In all animals, MNs were retrogradely labeled from the LG muscle with Fast Blue. Microglia were detected with eGFP (Tmem119^{eGFP}) amplified with immunohistochemistry. CD68 was detected with specific antibodies (see **Table 2**) in the Cy3 channel. The sections were imaged with confocal microscopy (60x, 2x zoom, and 0.5 µm step size) to sample sham, contralateral, On MN, and DC microglia and associated CD68 granules.

20-26 microglia per experimental condition (sham/injury, microglia type/location, and genotype) were reconstructed in IMARIS to calculate the eGFP-defined microglia volumes. We performed three types of estimates. The volume occupied by CD68 granules was calculated by extracting the total volumes of all objects with a CD68 signal detected in IMARIS and normalized to the total eGFP microglia volume and expressed as a percentage. In the case of death clusters, the total CD68 volume in the whole cluster was normalized to the whole death cluster volume since it was not possible to accurately separate individual microglia volumes in the death clusters. The number of CD68 granules was obtained from IMARIS segmentation of CD68 signals per microglial cell or death cluster. In the case of death clusters, the number of total granules was divided by the number of microglia composing the cluster to find a cell "average," allowing a more appropriate comparison to individualized microglia. Maximum granule size was obtained via automatic detection in IMARIS in the image segmentation for each microglia or death clusters and measured in μm^3. Individual microglia outliers were removed via the ROUT method (Q=1%). If the animal average was considered an outlier, the entire animal was excluded. Final sample sizes are described **in Supplemental Statistical Table 15 (Sampling Data CD68 Analysis, Supplemental Statistical Table 16 (CD68 analysis: Male Vs Female comparison in WTs), Supplemental Statistical Table 18 (CD68 total volume analysis), 19 (total CD68 granule numbers analysis), and 20 (maximum granule size analyses)**.

Analyses of motoneuron cross-sectional areas

To quantify the effects of TREM2 on cell body size changes during the chromatolytic reaction that occurs in response to axotomy we obtained 20x, 1x zoom and 1 µm z-steps confocal images of Fast Blue+ sciatic motor pool MNs at 3-, 7-, 14-, 21- and 28-dpi in WTs, GKO and CKO mice (N=4, 2 male / 2 female at all time points and genotypes, except for GKO at 28 dpi in which N=3, 1 male and 3 females and CKO at 21 dpi N=2 females, total N=57 mice). Confocal images were imported into Neurolucida, and an experimenter blinded to time after injury and genotype traced the outline of every cell body in the image in the optical plane in which the middle cross-section could be identified by finding the middle of the nucleus with an in-focus nucleolus. Five sections were measured per animal, and this represented a total of 7,090 manually traced MN cell body cross-sections or 124.4 ±28.9 (±SD) per animal with no significant differences among genotypes (WT: 118.3 ±26.0; GKO: 132.6 ±33.4; CKO 112.5 ±26.3). The area was measured in each traced Fast Blue+ MN cell body, and a distribution frequency histogram was calculated using 50 μm^2 bin sizes for each animal. Animal averages for each genotype and time point were averaged to obtain one cell size distribution for each

experimental condition (three genotypes X five time points = 15 conditions). Cell size distributions for each condition were then fitted to Gaussian distributions with n=2 (bimodal) using CalmpFit (ver.11, Media Cybernetics). For statistical comparisons, we constructed cumulative-summation (cum-sum) distributions of the percentage of neurons placed in increased size bins for each genotype across different times after injury. We also segmented the data in cells smaller than 450 μm^2 (usual cut off for γ-MNs (Shneider et al., 2009) or larger than 1000 μm^2 for detecting any possible cell swelling at particular time points and genotypes. Further details of sample sizes and organization are in **Supplemental Statistical Tables 25**.

To illustrate the significance of bimodal distributions in MN cell body size distribution, we analyze three naïve animals (1 female and 2 males) in which sections were immunostained for ChAT and NeuN. We measure all ChAT+ neurons in lamina IX of five L5 sections, focusing on the dorsal half of lamina IX corresponding to the sciatic motor pools (145.3 ±3.2 MN cell bodies traced per animal). The traces were then divided into cells with high or low NeuN and broadly corresponding to α- and γ-MNs (n=96.7 ±11.8 high NeuN and 48.7 ±11.8 low NeuN ChAT+ cell bodies traced per animal). The data were fitted to Gaussian distributions as above for the whole MN population and each of the high and low NeuN ChAT+ MN populations. Further details of sample sizes and organization are in **Supplemental Statistical Tables 22**.

Analysis of neuromuscular junction (NMJ) innervation

Ipsilateral LG muscle tissue was isolated and compressed as described in Wood *et al.* (2024) (Wood et al., 2025). Compressed LG muscle was embedded in OCT (Optimal Cutting Temperature Compound) and frozen before cutting 75 μm sections with a cryostat. Sections were allowed to air dry on slides at -20 degrees Celsius for a minimum of overnight and subjected to immunohistochemistry as described above. Sections were mounted on glass slides and cover-slipped with Vectashield with DAPI (Vector Labs, H-1200-10). Antibodies and dyes used, and their concentrations, are in **Table 2.**

20x/0.70 NA images were taken with an Olympus FluoView FV1000 confocal microscope. Thereafter, LG muscle neuromuscular junctions (NMJs) were analyzed manually in ImageJ, blind to surgery condition and sex (genotype cannot be quantified blindly due to tdTomato fluorescence in CKOs). First, the max projection z-stack was collapsed and transformed into a binary image via manual thresholding of each channel. An ROI was drawn around 50 *en face* NMJs per animal. The area of VAChT and α-Bungarotoxin (α-BTx) was measured to acquire the percentage of innervation area *per* NMJ. Fully innervated NMJs had

>50% coverage. The percentage of fully innervated NMJs was calculated per animal. Further details of sample sizes and organization are in **Supplemental Statistical Tables 26**.

Statistics

Each sample was analyzed for normality using Shapiro-Wilk tests. Normally distributed samples were compared using parametric statistics: one-way or two-way ANOVAs, followed by Bonferroni-corrected pair-wise multiple comparisons. Non-normally distributed samples were compared using Kruskal-Wallis ANOVA followed by Dunns' test pair-wise multiple comparisons. In a few cases, we compared only two data sets, and in this case, we used two-way t-tests. For each sample, we performed statistical comparisons for "Animal" and "Cell" data. Both are depicted in all graphs. "Animal" data consisted of comparing the averages of different animals, in which each animal is considered an independent data point. "Cell" data consisted of pooling all the data (microglia cells or MNs) from all animals in the same experimental group. There is significant discussion in the field about which data organization and comparisons are optimal (Dukkipati et al., 2017). "Cell" data preserves the original biological variability and has a large n, reducing sample size errors. "Animal" data losses the original biological variability, and results in smaller n, thus inducing Type I errors, particularly when n is small, like for example when sex differences are taken into consideration, and many multiple comparisons are performed simultaneously. In "Cell" data, not all values are independent (repetitive measures in the same animal). We avoid this problem by obtaining similar sample sizes and repetitions in all animals for each statistical comparison. In our data sets, "Cell" data had always higher variability and was always skewed and non-normally distributed, while "Animal" data was always normally distributed with lower variability. Statistical comparisons of both datasets were performed in parallel, and significance was set at $p<0.05$. In general, there was good agreement between both, and when this was not the case, it is noted in the results. N refers to the number of animals analyzed and n to the number of cells/sections.

In addition, we confirmed statistical conclusions by estimating effect sizes using estimation statistics (Ho et al., 2019). In this case, we calculated mean differences and Hedge's g for each pair-wise comparison and the 95% confidence intervals of estimates performing 5000 bootstrap subsamples with recalculation of both parameters. This allows us to create Gaussian distributed mean differences and Hedges' g estimates, making comparisons independent of original distribution properties on normality and variance. The data are represented by Cumming plots with bootstrap sampling distributions of estimates and dots representing the average estimate and vertical bars the 95% confidence intervals. The null hypothesis is that the

differences between equal samples equal 0. Rejection of the hypothesis occurs when 95% confidence limits do not cross 0 (less than 0.05 probability), in which case we conclude the calculated effect size is significant and conclude that the samples are different. This is then further confirmed with a permutation t-test with $p<0.05$. In general there was good agreement between parametric, non-parametric, and estimation statistics in the different Animal and cell samples, although estimation statistics tended to be more sensitive for detecting significance when n was small or when the number of multiple comparison performed generated corrections in post-hoc comparison that significantly increased the probability of Type I errors, particularly in very stringent Bonferroni tests in "Animal" data. We investigated possible sex effects with two-way ANOVAs for sex and conditions (i.e., sham/PNI; genotype, microglia types) to detect possible interactions. Sex comparisons are reported in supplementary figures, except when sex differences are critical for interpretation, in which case they are included in manuscript figures.

To compare cell size distributions, we used cum-sum plots and Kolmogrov-Smirnov (K-S) statistics. We compared differences in cell size distributions at different survival times within each genotype (WT, GKO and CKO).

Parametric and non-parametric statistics were performed in Prism (GraphPad), cell distribution fits and K-S tests were performed in Clampitt (media Cybernetics) and estimation statistics in the web app (https://www.estimationstats.com/#/). All statistical parameters, sample sizes, and effect sizes calculated are fully reported in a supplementary file named "Supplementary Statistical Tables."

Results

Activated microglia display two morphologically distinct phenotypes 14 days post sciatic nerve transection.

We have previously shown that Colony Stimulating Factor 1 (CSF1) triggers activation of ventral horn microglia following PNI, which leads to microglia proliferation and migration towards injured MN cell bodies (Pottorf et al., 2022; Rotterman et al., 2019), where they exhibit different types of cell-cell interactions (Rotterman & Alvarez, 2020). To study the heterogeneity of microglia-MN interactions, we utilized a Tmem119^{eGFP} reporter mouse in which microglia specifically express enhanced Green Fluorescent Protein (eGFP) without interfering with endogenous genetic programs (*Tmem119-2A-GFP* (Kaiser & Feng, 2019)). For identification of injured MNs, a subset of sciatic nerve MNs were retrogradely labeled with Fast Blue injected into the lateral gastrocnemius (LG) muscle five days before nerve surgeries. Animals were analyzed 14 days post injury (dpi), corresponding to the peak of the microglia reaction in the

ventral horn after PNI (Rotterman et al., 2019; Rotterman et al., 2024) (**Figure 1A**). Microglia eGFP fluorescence was amplified with antibody staining to optimally reveal morphological details. Spinal cords from sham animals contained typical surveying microglia with processes that occupied largely non-overlapping territories throughout the ventral horn. After PNI (in this case, a sciatic nerve cut and ligation), there was a prominent microglia reaction in the ventral horn region containing sciatic MNs (**Figure 1B**). As previously reviewed (Pottorf et al., 2022), following PNI, microglia increased in numbers and changed morphologies, retracting their processes. Individual microglia territories shrink but also greatly overlap during the microglia reaction. Some microglia attached to the cell bodies of MNs. Two distinct types of microglia-MN interactions were observed (**Figure 1C**). More frequently, microglia remained individualized from one another while they partially enwrapped the cell body of MNs with no evidence of degeneration. We refer to this phenotype as "On MN" microglia. A second interaction was less frequent and consisted of ameboid microglia that tightly cluster together, forming what we denote as a "Death Cluster" because it fully surrounds degenerating MNs. To quantify these different morphologies, microglia were semi-automatically reconstructed using IMARIS software and Sholl analyses performed after skeletonization. On MN and Death Cluster (DC) microglia were compared to surveying ventral horn microglia in sham animals or the contralateral ventral horn (**Figure 1D-E**, n=5 microglia per animal; N=6 animals per condition, equal sex numbers, 30 microglia in each experimental group). We found no sex differences (**Supplemental Figure 1A**) and therefore male and female data were pooled together. Surveying microglia in shams and on the contralateral side of PNI mice had ramified processes extending as far as 60 μm from the microglia cell body. Processes were shorter in activated On MN microglia, hardly extending beyond 30 μm from the cell body. DC microglia were the least ramified, with the fewest and shortest processes **(Figure 1D-E**). Two-way ANOVA for Sholl distance and microglia location revealed significant differences among the four experimental groups ($p<0.0001$ for both variables and their interaction, **Supplemental Statistical Table 1**). Post-hoc Bonferroni's pair-wise comparisons demonstrated that Sholl intersections were not significantly different between sham and contralateral control microglia, but both groups demonstrated significant differences with activated On MN and DC microglia (**Figure 1E** and **Supplemental Statistical Table 1**). The number of intersections in On MN and DC microglia was reduced by 78% and 156%, respectively, compared to sham at 20 μm distance and by 156% and 184% at 30 μm distance, with a negligible number of processes reaching the 40 μm distance bin. DC microglia showed fewer processes close to the cell body (10 μm Sholl bin) when compared to any other microglia group ($p<0.0001$ in all cases). The data further show that On MN microglia have significantly

longer and more complex processes 20 µm from their cell body compared to DC microglia ($p<0.0001$) (**Supplemental Statistical Table 1**). In summary, microglia show two distinct activated morphological phenotypes over injured MNs, depending on whether the MNs displayed degeneration features (death cluster) or not. One question is whether death clusters form independently of, or are derived from, the On MN microglia phenotype (**Figure 1F**).

Morphologically distinct phenotypes show different interaction dynamics with motoneurons.

To visualize differences in microglia dynamic interactions with MNs of varying health, we retrogradely labeled a subpopulation of MNs by injecting AAV1-tdTomato into the LG muscle of postnatal day five (P5) CX3CR1^{eGFP} mice. CX3CR1^{eGFP} mice express higher levels of eGFP compared to Tmem119^{eGFP} mice (not quantified) and are better suited for two-photon time-lapse imaging. When mice reached two months of age, they were subject to sham or cut-ligation nerve surgeries and analyzed at 14 dpi. Process dynamics were visualized in 30 to 90-minute-long two-photon time-lapse images using an *ex vivo* spinal cord slice preparation. Slicing the spinal cords was necessary to image labeled MNs inside the gray matter at high magnification (25x objective NA=0.95 and 2x to 4x optical zoom) (Rotterman & Alvarez, 2020).

In sham animals, surveying microglia minimally contacted MN cell bodies, and when microglia processes did contact the MN surface, the interaction was short-lived (**Figure 2A-B**, **Supplemental Video 1**). After PNI, activated On MN microglia had an increased number of processes contacting the cell body surface. These processes also spent longer periods on the surface and frequently performed “sweeping” motions across the cell body. Varicosities in microglia processes move towards the cell body, likely carrying endocytosed materials (**Figure 2C-D**, **Supplemental Video 2**). DC microglia displayed rapidly moving filopodia and minimal processes. Details of fine processes were difficult to resolve in the images because of the strong fluorescence emanating from the microglia cell body cluster. tdTomato debris was visible within death clusters, but defined MN cell bodies were indiscernible (**Figure 2E-F**, **Supplemental Video 3**).

In summary, activated On MN microglia have reduced processes and branches, but the number of contacts and time spent on the MN cell body surface increased compared to surveying microglia. At this location, microglia monitor injured MNs by surface contacts and endocytosis of released and/or microphagocytosed MN components. In contrast, DC microglia are ameboid, with minimal processes and filopodia that rapidly extend and retract. They typically include MN debris, suggesting macrophagocytic activity.

TREM2 expression increases in activated microglia after PNI, with Death Cluster microglia containing the highest levels.

Microglial TREM2 has been involved in neuronal phagocytosis with and without inflammation, synapse pruning during development or after neuropathology, and in regulating metabolic homeostasis (Filipello et al., 2018; Hsieh et al., 2009; Jay et al., 2019; Qu & Li, 2020; Rueda-Carrasco et al., 2023; Scott-Hewitt et al., 2020; Tagliatti et al., 2024; Takahashi et al., 2005; Yu et al., 2023). All these functions are highly relevant for axotomized MNs undergoing regeneration or apoptosis and agree with the "double-edged" properties proposed for TREM2 function in many different conditions (Konishi & Kiyama, 2018). To investigate a possible role of TREM2 in microglia-MN interactions after PNI, we first analyzed TREM2 protein expression on the membrane and cytosol of microglia by performing TREM2 immunohistochemistry on Tmem119^{eGFP} microglia (**Figure 3A**). We estimated average immunofluorescence intensity within microglia, excluding the intense immunofluorescent patch located in the Golgi (Sessa et al., 2004). Male and female data were pooled together because no sex differences were found in TREM2 expression (**Supplemental Figure 1B**). Comparisons were performed with all microglia pooled together ("Cell"; n=160 sham; n=181 On MN; n=52 DC; n=154 contralateral) or on animal averages ("Animal"; N=8 sham and 8 PNI animals, equal sex). "Cell" data preserved the original sample variance, and distributions were always skewed towards the high values exhibited in a proportion of microglia. "Animal" averages blunted cell-to-cell variations and were always normally distributed. Significant increases in expression were detected in activated microglia in both data sets. "Cell" data of On MN and DC microglia showed higher TREM2 content compared to microglia in sham animals ($p<0.0001$, Kruskal-Wallis ANOVA followed by Dunn's post-hoc multiple comparisons; **Figure 3B**, **Supplemental Statistical Table 2**). In addition, DC microglia showed significantly more TREM2 than On MN microglia ($p=0.002$, Dunn's test). Estimation statistics of bootstrapped mean differences, followed by permutation t-tests, confirmed these conclusions (**Supplemental Statistical Table 2**). Comparison of animal averages replicated the significant increases in DC microglia compared to sham or On MN ($p<0.0001$ and $p=0.0125$, respectively; One-way ANOVA followed by Bonferroni pair-wise tests). Estimation statistics of bootstrapped differences confirmed these results ($p<0.0001$ and $p=0.0088$, respectively, permutation t-tests) and in addition uncovered the difference detected in "Cell" data between sham and On MN microglia ($p=0.0012$) and that was not detected with Bonferroni comparisons in "Animal" data (type II error) (**Figure 3C, Supplemental Statistical Table 2**). The effect sizes were large. DC microglia (animal averages) contained 125% higher TREM2 compared to surveying microglia in sham animals (Hedges' g=2.1, 95%CI 1.3 to 3.4)

and 62% higher compared to On MN microglia (g=1.2, 95%CI 0.1 to 1.9) while On MN microglia showed 78% increase TREM2 immunoreactivity compared to sham (g=1.7, 95%CI 0.5 to 2.6). Sham and contralateral microglia showed no significant differences in “Cell” or “Animal” averages in all statistical tests (**Supplemental Statistical Table 2**). A significant amount of immunoreactivity was found outlining the cell bodies in activated microglia (**Figure 3A**), suggesting TREM2 translocation to the plasma membrane.

Next, we analyzed the time course of TREM2 expression after nerve injury. To best interpret the data in the context of regeneration we performed nerve injuries followed by repair with fibrin glue (Akhter et al., 2019) to allow regeneration and analyzed animals at 3, 7, 14, 21, and 28 days post-injury (dpi) (**Figure 3D**) (N=4 animal at each dpi, n=20 microglia analyzed per animal for On MN and contralateral; after removing outliers n varied between 72 and 79 microglia in different post-injury groups for contralateral and On MN microglia). Presence of DC microglia was variable at different times post injury, being rare at 3, scarce at 7 and 28 dpi, and frequent at 14 and 21 dpi. This created variability in the number of microglia (n) and animals (N) analyzed at different time points for DC microglia (3 dpi n=16, N=1; 7 dpi n=29, N=2; 14 dpi n=80, N=4; 21 dpi n=48 N=3; 28 dpi n=37, N=2). Since the number of Animals with recoverable data in death clusters was low at some time points, the data from different animals were pooled into “Cell” data sets for analyses. Two-way ANOVA of differences in TREM2 expression according to time after injury and microglia type (contralateral, On MN and DC) showed significant variations in TREM2 expression according to both variables and their interaction ($p<0.0001$ in all cases, **Figure 3E-F**, **Supplemental Statistical Table 3**). To reduce the incidence of Type II statistical errors, we limited pair-wise comparisons (Bonferroni tests) to first, adjacent dpi data sets within the time course of each microglia type (contralateral, On MN, and DC) and second, independent comparisons of all three microglia types within each time point (results in **Supplemental Statistical Table 3**). Salient results include a significant increase in TREM2 expression at 14 dpi for On MN and DC microglia compared to 7 dpi ($p<0.0001$ in both cases, 68% and 64% increases) that thereafter significantly decreases in microglia On MN at 21 dpi (14 to 21 dpi, $p=0.0083$; 25% reduction) and is further reduced at 28 dpi (21 to 28 dpi, $p=0.0015$; 37% decrease) (**Figure 3E-F**). In contrast, DC microglia partially maintain TREM2 expression at 21 dpi (14 to 21 dpi, $p>0.9999$), being decreased later, at 28 dpi (21 to 28 dpi, $p=0.0035$; 24% decrease) (**Figure 3E-F**). Comparisons among different microglia types at each time point revealed that TREM2 expression in DC microglia is higher at all time points compared to either contralateral (between 66% and 319% increase at different time points) or On MN microglia (63% to 141% higher), while On MN microglia TREM2 expression was significantly

higher than in contralateral microglia at 14 dpi (96% higher) and 28 dpi (74% higher) (**Supplemental Statistical Table 3, Figure 3E-F**). In conclusion, TREM2 expression parallels the time course of the microglia reaction, peaking at 14 dpi ipsilateral to the injury. DC microglia upregulate TREM2 at higher levels than any other ventral horn microglia ipsilateral to the injury throughout the period of microglia activation from 3 to 28 dpi and retain expression for longer after the peak. Moreover, TREM2 expression at 14 dpi was similar after different types of nerve injuries, whether MNs were allowed to regenerate (sciatic nerve cut and repair) or not (sciatic nerve cut and ligation). Finally, TREM2 expression in contralateral microglia did not show the large increase at 14 dpi characteristic of ventral horn microglia located ipsilateral to the injury, although it gradually increased from 3 dpi to a maximum at 21 dpi, before downregulating by 28 dpi. Most regeneration of motor axons and muscle reinnervation is complete by 28 dpi in our nerve injury model (Rotterman et al., 2024).

To investigate whether changes in TREM2 protein and membrane translocation were associated with changes in *trem2* gene expression, we evaluated *trem2* mRNA using RNAscope in CX3CR1^{eGFP} mice at 14 dpi after sciatic nerve cut and ligation (**Figure 4A**). CX3CR1^{eGFP} mice were used because intense endogenous fluorescence was able to withstand quenching from the RNAscope protocol. Robust *trem2* upregulation in activated microglia made accurate quantification of individual mRNA in 2D projections of confocal images difficult. To overcome this problem, we reconstructed *trem2* fluorescence within microglia (delineated by eGFP) or nucleus (marked with DAPI) as 3D objects in IMARIS and calculated *trem2* volume occupancy in each cellular compartment (n=35 sham; n=47 contralateral; n=49 On MN; n=6 DCs; N=4 sham equal sex, and 2 male/3 female PNI animals). It was not possible to individualize microglia in death clusters for IMARIS 3D reconstruction. In this case, we obtained an average occupancy ratio of *trem2* mRNA per whole microglia cluster. This explains the lower n in DC microglia data. A sex difference was found in total *trem2* being significantly higher in female DC microglia vs male, while there were no sex differences in the other types of microglia analyzed (p=0.026, Bonferroni corrected pair-wise comparison, **Supplemental Figure 1C**). Nevertheless, both male and female DC microglia showed the highest *trem2* signal compared to other microglia in both sexes. We pooled data from both sexes together because no differences were found in most microglia, and number of sex-specific death clusters obtained was low. Like TREM2 protein, *trem2* mRNA was evaluated in “Cell” or “Animal” averages (**Figure 4B**). Similarly, “Cell” data was distributed in all experimental groups with a strong skew towards high values, while “Animal” data was distributed normally and showed lower variance. Compared to sham, On MN and DC microglia had significantly higher total *trem2* mRNA, whether compared

in “Cell” or “Animal” data (Cell: p<0.0001; Kruskal Wallis; Animal: p=0.0173 One-way ANOVA). Also, like protein analyses, effect sizes were large. On MN microglia showed 420% and 333% increases in *trem2* mRNA when compared to sham by “Cell” (g=2.1 95% CI 1.7-2.5, p<0.0001, Dunns or permutation t-test) or “Animal” data (g=5.3 95% CI 3.7-6.9, p=0.0519, Bonferroni, 0.0330 permutation t-test). When comparing DC microglia to sham, these values were 540% higher by “Cell” (g=3.0, 95% CI 1.0-5.7, p=0.0003 Bonferroni, p<0.0001 permutation t-test) or 433% by “Animal” (g=1.5, 95% CI -4.0-5.6, p=0.0251 Bonferroni; p=0.0540 permutation t-test). We also found some evidence for a possible small increase in *trem2* mRNA expression in microglia contralateral to the injury compared to sham when compared by “Cell” (**Figure 4C**, p=0.0011 Dunns, 160% increase, g=0.9, permutation t-test p<0.0001) although significance was not reached comparing “Animal” averages (p=0.8532, Bonferroni, 160% increase, g=1.34, permutation t-test p=0.0712) (**Supplemental Statistical Table 4**). Differences in total mRNA were mirrored by differences in *trem2* mRNA inside microglia processes (**Figure 4E, Supplemental Statistical Table 6**). In contrast, nuclear *trem2* content was unchanged among the four experimental groups (Cell: p=0.0501; Kruskal-Wallis; Animal p=0.8716 via One-way ANOVA) (**Figure 4D, Supplemental Statistical Table 5)**. These data suggest that higher TREM2 protein in the cytosol and on the membrane is due to higher expression of *trem2* mRNA in the cell body and processes. Moreover, higher TREM2 protein content in DC compared to On MN microglia, despite similar *trem*2 mRNA levels, suggests post-translational differences in *trem2* mRNA regulation, and/or TREM2 trafficking from Golgi to cytoplasm and membrane, and/or protein half-life. Collectively, we report an increase in *trem2* mRNA and TREM2 protein in activated microglia following PNI, with DC microglia displaying a significantly greater accumulation of TREM2 protein on the membrane and in the cytosol.

TREM2 knock-out validation and suppression of downstream p-SYK

To elucidate TREM2’s role in microglia interactions with MNs, we used two different mouse models to delete *trem2*: a global *trem2* Knock Out (GKO) and a timed and microglia-specific conditional *trem2* Knock Out (CKO). TREM2 is expressed by microglia and in many peripheral tissues (Colonna, 2023; Jay et al., 2017; Lee et al., 2021; Sun et al., 2020; Wang et al., 2025), including peripheral macrophages that also play roles in functional recovery and MN survival following PNI (Cattin et al., 2015; Chen et al., 2019; Gordon, 2020; Olsson & Sjöstrand, 1969; Rios et al., 2021; Tomlinson et al., 2018; P. L. Wang, 2021; P. L. Wang et al., 2020; Witzel et al., 2005; Ydens et al., 2012). Moreover, TREM2 modulates several developmental actions, including synaptic refinement (Matteoli, 2024). By comparing GKO and CKO, we hoped

to distinguish the effects of deleting *trem2* specifically in microglia just before PNI from any global effects of removing *trem2* from all tissues and throughout development. To identify microglia in GKO animals, we crossed these animals with Tmem119^{eGFP} mice. To obtain animals with a microglia-specific deletion of *trem2,* we cross-bred mice with *trem2* floxed alleles with *tmem119-2A-creERT2* mice and the Ai9 R26 *lsl-tdTomato* cre-reporter mice. The triple mutant (CKO) had all three alleles in homozygosis: *tmem119* $^{creERT2/creERT2}$ ::*trem2*$^{flx/flx}$ ::*R26* $^{lst-tdT/lsl-tdT}$. Recombination was induced with five doses of tamoxifen (i.p. 2mg/kg) separated by 24 hours, starting at P28 and before nerve surgeries at two months of age. From here on, Tmem119^{eGFP} animals with wildtype TREM2 will be referred to as "wildtype (WT)."

We first validated successful TREM2 protein KO in microglia via immunohistochemistry and using IBA1 as an independent microglia label (**Supplemental Figure 2A**). TREM2 protein was undetectable with immunofluorescence in IBA1-labeled or in genetically labeled microglia in GKO and CKO mice (microglia genetic labels: eGFP in WT and GKO and tdTomato in CKO). CKO mice express tdTomato in 93.2% of IBA1+ cells, suggesting a high efficiency of induced recombination in our model (n= five L5 sections per animal, N=4) (**Supplemental Figure 2B**). We further validated successful *trem2* KO in both models via RNAscope for *trem2* mRNA (**Supplemental Figure 2C**). Of note, the Tmem119^{eGFP} reporter in the GKO mouse does not have strong enough fluorescence to withstand quenching during RNAscope; therefore, microglia in GKO mice were labeled with IBA1 antibodies. In contrast, the endogenous tdTomato signal in CKO mice endured RNAscope processing when amplified with antibody labeling. CKO mice showed no *trem2* mRNA signal in genetically defined microglia, while GKO mice showed a very reduced signal in IBA1 microglia. This difference may stem from differences in exon preservation in the design of these KO mouse models (see descriptions in methods). The RNAscope method was validated using positive and negative controls. Positive controls encompassed a group of common housekeeping genes (often seen in neurons), whereas the bacterial *Bacillus subtilis dapB* gene was used as a negative control (**Supplemental Figure 2D-E**). Thus, the lack of the *trem2* signal in GKO and CKO mice was not due to poor mRNA preservation in our samples or other technical inefficiencies.

To further show reduced TREM2 microglia function in GKO and CKO mice, we analyzed the accumulation of downstream phosphorylated Spleen Tyrosine Kinase (p-SYK). p-SYK immunolabeling increased in parallel to the increases in TREM2 protein in activated Tmem119^{eGFP} microglia (**Figure 5A**). Since most p-SYK accumulated on the membrane, we outlined the microglia edge and measured p-SYK immunofluorescence integrated pixel density along the cell body membrane and normalized against background (see methods). Using this

method On MN microglia showed 62.5% increase in fluorescence and DC microglia a 737.4% increase compared to surveying microglia in sham controls ($p<0.0001$, Kruskal-Wallis followed by Dunn's multiple comparisons; n=77 sham; n=104 On MN; n=24 DC; N=4 sham; N=6 cut) (**Figure 5B, Supplemental Statistical Table 7**). Interestingly, microglia on the contralateral side of PNI animals also showed a smaller (37%), but statistically significant, increase compared to sham ($p=0.0028$, Dunn's test). This further suggests the possibility of some small but functionally significant TREM2 upregulation in contralateral microglia. In addition, we found a sex effect in that DC microglia in females had 125% more p-SYK than in males ($p<0.0001$, Two-Way ANOVA with Bonferroni's multiple comparisons; n=4 male; n=20 female; N=2 equal sex) (**Supplemental Figure 3**). This result parallels the sex difference encountered between male and female DC microglia in *trem2* mRNA expression (**Supplemental Figure 1C).** No sex differences in p-SYK accumulation were found in contralateral microglia or On MN microglia.

Upon TREM2 ligand binding, phosphorylated DAP12 causes SYK phosphorylation (Pottorf et al., 2022), but numerous other receptors, including but not limited to C-type lectin 7a (CLEC7a), Fc Receptors, CD33, and CD22 (Ennerfelt et al., 2022; Pottorf et al., 2022; Wang et al., 2022), also phosphorylate SYK in activated microglia. Therefore, to corroborate that TREM2 loss resulted in reduced p-SYK signaling, we compared the GKO and CKO mice to our "WTs" (Tmem119^{eGFP} mice). Contralateral, On MN, and DC microglia had reduced p-SYK content in GKO and CKO mice compared to WTs. The results replicated whether analyses were done with "Cell" or "Animal" data sets: 52-53% reduction in GKO ($p<0.0001$ Cell; $p=0.0061$ Animal) and 35-38% in CKO ($p<0.0001$ Cell; $p=0.0335$ Animal) in contralateral microglia; 58-58% reduction in GKO ($p<0.0001$ Cell; $p=0.001$ Animal) and 49-48% in CKO ($p<0.0001$ Cell; $p=0.0335$ Animal) in On MN microglia; 88% reduction in GKO ($p<0.0001$ Cell) and 87% in CKO ($p<0.0001$ Cell) in DC microglia (**Figure 5B, Supplemental Statistical Table 7**). DC microglia were not analyzed in "Animal" data sets because we recovered only n=2 WT mice with measurable death clusters. There was no sex difference in the reduction of p-SYK on GKO and CKO mice (**Supplemental Figure 3**).

In summary, TREM2 is efficiently removed from microglia in both GKO and CKO mice. Moreover, the data demonstrate that the increase in p-SYK accumulation in activated microglia after PNI is dependent on TREM2 expression. p-SYK was more abundant in DC microglia, similar to differences noted for TREM2 protein expression. Sex differences in DC microglia for *trem2* mRNA were paralleled by increased p-SYK.

TREM2 knockout does not affect the number, territories, or process lengths and branching of non-activated surveying microglia in sham animals.

Previously, TREM2 KO was reported to alter surveying microglial morphology, reduce the number of microglia, and collapse microglia territories in one-month-old murine cortex (Jay et al., 2019). We sought to confirm these findings in TREM2 GKO and CKO spinal cord microglia phenotypes compared to Tmem119^{eGFP} "WT" mice (N=7 Tmem119^{eGFP} WT; N=7 Tmem119^{eGFP} GKO; N=5 Tmem119^{creERT2} tdTomato CKO). All animals underwent sham surgery with no evidence of ventral horn microglia activation. No sex differences were found for the number of microglia or average microglia territory size in the L5 ventral horn (WT N=3 male/4 female; GKO N=4 male/3 female; CKO N=4 male/1 female; **Supplemental Figure 4A-B**). Estimated microglia numbers in uninjured WTs were on average 5.3 ±0.8 (SD) microglia per 10^6 μm^3 (a 100 µm side cube volume) and their 2-dimensional projection territories in WTs measured on average 4,007 μm^2 ±707 (SD) corresponding to approximate diameters of 65-77 µm suggesting that processes extending further than 50 µm from the cell body normally partially overlap. Although there was a slight trend (~11-12% change) towards reduced microglia numbers (**Figure 6A-B**) and increased average territory sizes (**Figure 6A,C**) in the ventral horn of GKO and CKO sham mice compared to WT, these differences were not significant (One-way ANOVAs p=0.2246 microglia number, p=0.3871 microglia territories; **Supplemental Statistical Tables 8 and 9**). This conclusion was confirmed with estimation statistics compared to WT (permutation t-tests and Hedges' g for microglia numbers: p=0.1658 g=0.76 GKO; p=0.1362 g=0.86 CKO; for microglia territories: p=0.2748 g=0.58 GKO; p=0.22 g=0.7 CKO, **Supplemental Statistical Tables 8 and 9**). Cell morphology did not change either in GKO sham animals (Sholl analyses of n=5 microglia reconstructed and skeletonized compared to WT reconstructions from Figure 1, N=6 per condition, equal sex; **Figures 8A,B**). Two-way ANOVA for number of intersections at different Sholl distance bins in different genotypes found significant differences with Sholl bin (p<0.0001, as expected) but not according to genotype (p=0.6677) or the interaction of Sholl bin and genotype (p=0.0571) (n=30 reconstructed cells in GKO and WTs, **Supplemental Statistical Table 13**). We could not adequately compare CKO microglia morphologies to WT and GKO microglia because tdTomato filled distal processes less efficiently than eGFP, even after immunocytochemical amplification of tdTomato. In summary, TREM2 deletions had no discernible effects on the morphological properties of ventral horn surveying microglia before any activation or injury.

TREM2 Knockout does not affect microglia proliferation or the time course of microglia activation following PNI.

TREM2 KO has been shown to reduce microglia proliferation and migration in Alzheimer's disease (S. Wang et al., 2020; Zheng et al., 2017) and cuprizone-induced demyelination models (Cantoni et al., 2015). We previously demonstrated that microglial CSF1R activation is critical for microglia proliferation and activation following PNI (Pottorf et al., 2022; Rotterman et al., 2019), and CSF1R downstream actions include augmenting transcription of *tyrobp* (DAP12) and TREM2 signaling (Guan et al., 2016; Pottorf et al., 2022). Therefore, we performed a time-course analysis of ventral horn microglia proliferation by estimating their numbers (**Figure 7A,B**) and the percentage of Ki-67 positive microglia (**Figure 7C-H**) after PNI in both TREM2 KO models (GKO or CKO). The Ki-67 antibody used was made in mouse and cross-reacted with microglial Fc receptors upregulated after activation. Despite this, we were able to distinguish between true versus nonspecific Ki-67 labeling at 20x magnification by focusing on nuclear localization. WT, GKO, and CKO mice underwent sciatic nerve cut repair with a Fast Blue nerve soak to retrogradely label the entire injured sciatic MN population. Mice were euthanized at 3, 7, 14, 21, and 28 dpi (N=4 animals per genotype/time point, 2 male/2 female, except for CKO animals at 21 dpi in which only 2 females were analyzed). Sham mice were not included in these analyses as the Fast Blue nerve soak requires nerve transection and injury.

The number of ventral horn proliferating microglia after PNI (estimated from n=five L5 sections per animal) showed significant differences analyzed via two-way ANOVA for time after injury and genotype (WT, GKO, and CKO) (time after injury $p<0.0001$; genotype $p=0.0157$) (**Figure 7B**, **Supplemental Statistical Table 10)**. In all three genotypes, the number of microglia peaked at 14 dpi and then declined towards normal values by 28 dpi. Although GKO and CKO mice consistently trended towards fewer microglia than WT mice, post-hoc pairwise Bonferroni tests did not detect significant differences between genotypes at any time point. The low n per time/point genotype combined with inter-animal variation suggested underpowered comparisons given the relatively small effect sizes (always smaller than 21% difference during the raising phase of microgliosis from 3 to 14 dpi). Power analyses (G*Power version 3.1.9.7) indicated that n's would need to be increased to 40 animals per genotype/time point, which is unfeasible. The differences among genotypes are therefore small, if any, and the percentage increase in cell numbers from 3 to 14 dpi was similar in all three genotypes (WT 68%; GKO 66%; CKO 56%). We therefore concluded that TREM2 KO had little, if any, effect on microglia proliferation in the spinal cord ventral horn after PNI. This conclusion differs from other

pathologies/injuries in which TREM2 was reported to strongly modulate microglia proliferation (Cantoni et al., 2015; S. Wang et al., 2020; Zheng et al., 2017). Thus, we conclude that TREM2 makes a very small contribution, if any, to the CSF1-dependent microglia proliferation that occurs in the spinal cord ventral horn after PNI (Pottorf et al., 2022; Rotterman et al., 2019).

We confirmed this conclusion using Ki-67 antibodies as a direct marker of cell-cycling microglia in the same animals and section samples. In all genotypes, Ki-67 peaked at 3dpi, with much less proliferation occurring at 7dpi (**Figure 7C,D**). Two-way ANOVA showed significant differences for time after injury ($p<0.0001$) but not among genotypes ($p=0.1156$) (**Supplemental Statistical Table 11**). At 3 dpi, Ki-67 was detected in 25.4% ±3.0, 33.0% ±17.4, and 15.8% ±8.8 (±SD) microglial cells in WT, GKO, and CKO. This percentage was greatly reduced at 7 dpi to 1.3% ±0.5, 3.7% ±2.9, and 0.9% ±0.9 (±SD) in WT, GKO, and CKO. Thereafter, less than 1% of microglial cells showed Ki-67. This result agrees with our previous report showing ventral horn microglia proliferation restricted to the first week after injury and being higher at 3 dpi compared to 7dpi, while the increase in microglia numbers during the second week depends on migration and/or contributions from the periphery (Rotterman et al., 2019). TREM2 deletion did not alter microglia proliferation intensity or time course. Intriguingly, while most Ki-67+ microglia at 3dpi *were not* contacting MN cell bodies, the microglia that remained cell-cycling at 7dpi *were* contacting MN cell bodies (**Figure 7E**). TREM2 content in proliferating On MN microglia increased from 3 to 7 dpi (**Supplemental Figure 5**). For quantification, ventral horn microglia were categorized by cell location into microglia not contacting MNs, On MNs, in DCs, or in the White Matter. In WTs, 76% to 93% (86.5% ±7.9 (SD)) of Ki-67+ ventral microglia were found in the grey matter at 3 dpi and all (100%) at 7 dpi. Around a third of proliferating Ki-67+ microglia were found On MN at 3 dpi, but this percentage increased to 75.3% ±29.0 at 7 dpi, a very large change. This data suggests that interactions with MNs may lengthen the proliferation time course, although this is not causally related to increases in TREM2 content from 3 to 7 dpi. Death clusters rarely contained any proliferating Ki-67+ cells in any animal of any genotype (**Figure 7E,F**). This observation further suggests that death clusters form by coalescence of On MN microglia when the MN degenerates, and not by local proliferation.

We next investigated whether TREM2 is necessary for the formation of death clusters. The number of death clusters at 3, 7, 14, 21, and 28 dpi was compared in WT versus GKO and CKO. In each spinal cord, we counted death clusters in all Lumbar 1 to 6 showing microgliosis in each animal. This number was normalized to the number of sections collected and multiplied by 100 to estimate the total number of death clusters in a 5 mm length (100 x 50 mm thick sections) of the lumbosacral enlargement. This region corresponds to the column of injured

sciatic MNs, which encompasses Lumbar 4 to 6. In WT mice (Tmem119^{eGFP}), the number of death clusters peaked at 14 dpi (**Figure 7G**), coinciding with the peak of the number of microglia (**Figure 7B**). Although GKO and CKO tended to have fewer death clusters than WT mice, two-way ANOVA for time after injury and genotype showed no significant differences between WT, GKO, and CKO for the number of death clusters at any time point. These results were confirmed with estimation statistics. Comparing the number of death clusters at the peak 14 dpi resulted in non-significant differences (WT vs GKO Hedges' g =-1.2, 95% CI -3.3, +1.4, permutation t-test p=0.1176; WT vs CKO Hedges' g= 0.1, 95% CI -1.3, +1.4, permutation t-test p=0.801) (**Figure 7G**). We also compared the number of death clusters between 14 dpi cut-ligation (non-regenerating MNs) and 14 dpi cut-repair animals (motor axon regeneration allowed). TREM2 WT and CKO mice did not have significantly different amounts of death clusters between the two surgery models (p>0.9999, One-Way ANOVA with Bonferroni's multiple comparisons, N=14 WT and 8 CKO cut-ligation; N=4 cut-repair per genotype) (**Supplemental Figure 6A-B**). GKO mice, however, had fewer death clusters following a cut-repair compared to a cut-ligation (p=0.043 via One-Way ANOVA with Bonferroni's multiple comparisons, and Hedges' g of 1.073 [95.0%CI -1.93, -0.30], permutation p=0.0652) (**Supplemental Figure 6A-B**). This may indicate that peripheral TREM2 may have some modulation on death cluster formation that may require further investigation in the future.

TREM2 KO alters microglia morphology mainly in Death Cluster microglia, with little effect on the number of microglia-MN interactions.

Once we showed no effects of TREM2 KO on microglia proliferation or death cluster formation, we asked whether the morphology of activated microglia or their migration towards/interactions with injured MNs were unchanged. We compared microglia morphologies in contralateral and On MN and DC microglia 14 days after sciatic nerve-cut ligations (n=30 cells in WT and 30 in GKO for each microglia category, 5 cells per animal N=6 WTs and 6 GKO animals, equal sexes). GKO microglia process densities and lengths estimated by Sholl intersections were no different to WTs in contralateral and On MN microglia (p=0.1016 and 0.3120, respectively following two-way ANOVAs that tested for Sholl distance and genotype; all were highly significant for Sholl distance p<0.0001). However, a significant difference was detected in GKO DC microglia (p=0.0014). Specifically, there was a 34%, 83% and 105% increase in intersections, respectively at 10, 20, and 30 μm Sholl distances, although only the increase at 20 μm reached significance using Bonferroni post-hoc pair-wise comparisons

(p=0.0187) (**Figure 8A-B, Supplemental Statistical Table 13**). We conclude that TREM2 is minimally involved in the morphological changes that occur in activated microglia On MNs but partially prevents process retraction in DC microglia.

TREM2 activity modulates microglia migration and microglia-neuron interactions in other neuropathologies (Jairaman et al., 2022; Mazaheri et al., 2017; Sayed et al., 2018); therefore, we estimated in all three genotypes the number of microglia in contact with MNs in sham controls and 14 days after PNI (in this case, a sciatic nerve cut and ligation). Note that in sham control animals, most contacts with MNs occurred via microglia processes, while after PNI, microglia and MN cell bodies frequently apposed each other in either the On MN or DC configuration. Analyses were performed on Fast Blue+ MNs retrogradely labeled from LG muscle and contacted by either eGFP (WT and GKO) or tdTomato (CKO) labeled microglia. We analyzed 8 WT (equal sex), 7 GKO (4 male /3 female), and 5 CKO (2 male /3 female) animals with sham surgeries and 8 WT (equal sex), 8 GKO (equal sex), and 7 CKO (4 male /3 female) animals after PNI. We did not detect significant sex differences (**Supplemental Figure 4D**). After sham surgeries, the number of microglia contacting MNs was 1.6 ±0.6 (±SD) in WT, 1.7 ±0.7 in GKO, and 1.1 ±0.5 in CKO, but after PNI, this number increased to 5.3 ±2.4, 5.7 ±0.9, 4.4 ±0.7 microglia On MN and 6.3 ±1.7, 6.7 ±1.8, 6.6 ±2.0 in DC microglia. The number of MNs analyzed per animal (excluding outliers) was 7 to 10 for sham or On MN microglia (9.7 ±1.0 across all three phenotypes). However, the number of death clusters found and analyzed per animal was less (1 to 10, for an average of 3.9 ±1.0). Thus, the total number of MNs analyzed in each group was 75 WT, 69 GKO, and 58 CKO in animals with a sham surgery, and 77 WT, 66 GKO, and 78 CKO MNs after PNI (On MN phenotype), and 33 WT, 22 GKO, and 29 CKO death clusters. Data was analyzed in “Cell” and “Animal” data sets. Average numbers of microglia associated with each MN (sham or On MN) or in DC microglia in “Cell” data were similar to those calculated for “Animal” averages, but as expected, there was higher variance (**Figures 8C,D**). We compared microglia associations in sham, On MN, and DC microglia for each genotype and the number of microglia associations in each experimental condition (sham, On MN or DC) across genotypes (**Figure 8C**). The results are summarized in **Supplemental Statistical Table 14**. As expected, the increase in the number of microglia associations with MNs after PNI comparing On MN and DC microglia to the sham condition was highly significant in all three genotypes in both “Animal” and “Cell” data sets (p<0.0001 in all cases; one-way ANOVAs followed by pair-wise Bonferroni post-hoc tests for “Animal” data, Kruskal-Wallis followed by Dunns tests for “Cell” data). This conclusion was confirmed with estimation statistics and g values were large: they ranged from 3.3 to 5.3 in “Animal” data and 2.6 to 3.7 in “Cell”

data. Second, we detected a small decrease in associated microglia in the CKO genotype compared to WT and GKO in both sham and On MN experimental conditions. This difference reached significance in the “Cell” data set but not in the “Animal” data . Estimation statistics confirmed the significance obtained with “Cell” data but also showed that effect sizes were small (g varied from 0.44 to 0.63). Given the small effect and the fact that the GKO condition did not replicate CKO results, we conclude that this small difference is most likely derived from the smaller and fewer processes revealed with tdTomato genetic labeling of microglia in CKO animals. Accordingly, no difference in the number of microglia associations was observed across genotypes in death clusters in which the efficiency of process labeling is irrelevant.

In conclusion, TREM2 KO (global or microglia-specific) had only small effects on the morphological changes that occur in microglia from surveying to activated On MNs or DC microglia. No significant effects were detected on microglia migration or associations with injured MNs. Overall, the results indicate that in our PNI models, TREM2 is not necessary for microglia proliferation, migration towards or enwrapping injured MNs, or the evolution of microglia interactions from the On MN phenotype towards death cluster formation.

Death Clusters display the greatest phagocytic capacity assessed by CD68. TREM2 KO reduces CD68 expression, but this is selective to females.

DC microglia are morphologically similar to Disease-Associated Microglia (DAM), commonly found surrounding amyloid plaques in Alzheimer’s disease, as well as in other neurodegenerative conditions (Deczkowska et al., 2018; Keren-Shaul et al., 2017; Sasaki et al., 1997; Sobue et al., 2021; Streit et al., 1999). Single-cell RNA transcriptomics have shown that DAM have elevated levels of *trem2* (Keren-Shaul et al., 2017; Olah et al., 2020; Pettas et al., 2022; Zhong et al., 2019). Further, DAM are typically regarded as highly phagocytic (Keren-Shaul et al., 2017; Streit et al., 1999). Thus, we questioned 1) if DC microglia, which have elevated levels of TREM2, also display increased phagocytosis tested by CD68 expression, and 2) if TREM2 regulates CD68 expression. We analyzed CD68 expression in microglia 14 days after a sciatic cut-ligation. Like our experiments on microglia morphology, we only compared WTs to GKO mice because differences in microglia process labeling in CKO mice due to differences in genetic labeling efficiencies (i.e., Tmem119^{eGFP} vs. Tmem119^{tdTomato}) can bias results. Representative images (all from male mice) are shown in **Figure 9A** and demonstrate an increase in CD68 labeling in DC microglia with respect to surveying microglia (sham and contralateral) and activated On MN microglia, and a reduction in CD68 labeling, especially in death clusters from GKO mice compared to WT.

To quantify this result, we analyzed 8 WTs (4 male / 4 female) and 7 GKOs (4 male / 3 female) in sham surgery animals and 7 WTs (4 males / 3 female) and 8 GKOs (4 male / 4 females) 14 days after PNI (in this case a sciatic cut-ligation). In each animal, we analyzed between 17 to 26 microglia at each of the four locations (sham, contralateral, On MN and DC) for a total of 464 IMARIS 3D reconstructed microglia in WTs and 488 in GKO animals. After identifying outliers final sample sizes for each experimental condition are as reported in **Supplementary Statistical Table 15**. We calculated the proportion of microglia volume occupied by CD68 granules (**Figure 9B, Figure 10A,D**), the number of CD68 granules per microglia (**Figure 9C, Figure 10B,E**), and the maximum size of detected CD68 granules in each cell (**Figure 9D, Figure 10C,F).** We used maximum size instead of average size as an indicator of differences in phagocytic activity because all microglia contained mostly small granules, sometimes below optical resolution limits (<0.2 μm), and these populations of small size granules overwhelmed average size estimations. As before, we generated "Cell" and "Animal" data, but for simplicity, we report statistical tests on "Cell" data. We noted important, significant sex differences in WTs (**Figure 9B; Supplementary Statistical Table 16**). Two-way ANOVAs in WT "Cell" data for microglia type and sex showed significance for both ($p<0.0001$) in total volume and number of granules in sham, contralateral, and On MN microglia. Females had more CD68 granules, and overall, CD68 granules occupied more volume in surveying (sham and contralateral) and activated (On MN) microglia in females compared to males ($p<0.0001$, pairwise Bonferroni tests confirmed by estimation statistics, **Supplemental Statistical Table 16).** The percentage of microglia cell volume occupied by CD68 granules in WT female sham, contralateral, On MN and DC microglia was respectively 10.0% ±7.9 (SD), 8.4% ±5.3, 9.4% ±5.1 and 37.5% ±20.0 and in WT male microglia 3.2% ±2.0 (SD), 3.8% ±3.2, 6.7% ±7.3 and 29.2% ±23.2.CD68. Thus, female microglia had two-to-three times more CD68 granules and total CD68 volume in surveying and activated On MN microglia, with Hedges' g values ranging from 1.0 to 2.0. In contrast, granule maximum size did not show consistent differences according to sex in sham, contralateral, and On MN microglia (Bonferroni tests), although they reached significance when compared using estimation statistics and permutation t-tests (**Supplemental Statistical Table 16).** Nevertheless, estimated differences in granule size were relatively small and more variable from animal to animal (Female to Male Hedges's g=1.2 in sham, 0.8 contralateral, 0.4 On MN microglia). DC microglia with greater CD68 expression compared to On MN, contralateral or sham microglia showed little sex differences.

To test the role of TREM2, we compared CD68 content in WT and GKO animals in all four microglia types (sham, contralateral On MN and DC) and separated the data according to

sex (**Figure 10, Supplemental Statistical Table 17**). Two-way ANOVAs on total volume occupied by CD68 granules in "Cell" data detected significant changes according to animal genotype, microglia phenotype, and their interaction in both sexes (**Supplemental Statistical Table 17**). This was paralleled by significant changes in CD68 granule numbers and maximum sizes. "Animal" data statistics generally agreed (**Supplemental Statistical Table 17).** Within each sex and genotype DC microglia maximally expressed CD68. CD68 granule volume occupancies significantly increased by 286% and 925% in DC microglia of different sexes and genotypes compared to sham microglia of the corresponding genotype and sex ($p<0.0001$ in all comparisons, Bonferroni t-tests; **Figure 10, Supplemental Statistical Table 18)**. These differences were driven by a very large increase in the maximum size of CD68 granules (usually over 1,000% compared to sham, $p<0.0001$ in all comparisons; **Figure 10, Supplemental Statistical Table 20**) while changes in CD68 granule numbers were less intense and frequently did not reach significance (**Figure 10, Supplemental Statistical Tables 19).** Generally, differences between sham and contralateral and On MN microglia were smaller, more variable or non-significant (**Figure 10, Supplemental Statistical Tables 18, 19, and 20).** Thus, CD68 granules in DC microglia are much larger, confirming a different phagocytic behavior.

The effects of TREM2 in these patterns of CD68 granule expression were analyzed by both Bonferroni tests and estimation statistics (**Figure 10, Supplemental table 21**). TREM2 deletion had different effects in females (**Figure 10A-C)** and males (**Figure 10D-F)**. In females, we estimated a decrease in total CD68 granule volume that was relatively similar in effect size in sham (76.3% reduction, $g=-1.4$), contralateral (69%, $g=-1.6$), On MN (47.1%, $g=-1.0$) and DC microglia (69.1%, $g=-2.3$). Decreases were always significant ($p<0.0001$ Bonferroni tests, and similar p values were obtained with permutation t-tests, except for the difference in DC microglia $p=0.0004$). These decreases correspond with parallel reductions in granule number and maximum sizes. Granule numbers were reduced in TREM2 GKOs from 28.8% in sham ($p=0.0289$, Bonferroni, $g=-0.5$, $p=0.0026$ permutation t-test) to 70.6% in DC microglia ($p=0.0028$, Bonferroni, $g=-2.1$ $p=0.0014$ permutation t-test). Maximum size reductions ranged from 67.2% in sham microglia ($p=0.0723$ Bonferroni, $g=-1.4$, $p<0.0001$ permutation t-test) to 86.9% in DC microglia ($p<0.0001$ Bonferroni, $g=-2.2$, $p=0.0054$ permutation t-test). Consistently, Hedge's g effect size estimations were larger in female DC microglia for all CD68 content parameters measured when compared to the other microglia types. The results in males were more complex. Total CD68 volume was reduced in TREM2 GKO DC microglia (45.7%, $g=-0.7$), but the results were inconsistent between Bonferroni testing ($p<0.0001$) and permutation t-tests ($p=0.1284$). Parallel reductions in CD68 granule numbers (52.0% $g=-1.7$) and maximum size

(21.2%, g=-0.2) in male TREM2 GKO DC microglia were calculated, but they were generally non-significant by both Bonferroni and permutation t-tests. However, we did find a consistent increase in CD68 granule number in sham (86.2%, g=1.0), contralateral (97.1%, g=1.0) and On MN (76.3%, g=1.0) microglia of TREM2 GKO males that was always significant compared to WT controls ($p<0.001$ for all comparison with both Bonferroni and permutation t-tests). A change in granule max size in the opposite direction did not reach significance but seemed to counteract granule numbers, such that overall, there is no change in male microglia in the total occupancy of the microglia volume by CD68 granules.

Collectively, our data shows that DC microglia are phagocytic hubs compared to individualized On MN microglia interacting with regenerative MNs and surveying microglia located contralaterally and in sham littermates. CD68 granules were dysregulated in both female and male TREM2 GKO mice, but while the lack of TREM2 greatly affected phagocytic capacity in females, and particularly in DC microglia, the effects were milder in males. Male GKO microglia outside death clusters consistently showed more granules but without significant changes in total volume, suggesting the excess CD68 granules were generally smaller. In contrast, DC microglia in males were not significantly affected by the lack of TREM2. The restriction of TREM2 GKO effects to female DC microglia may be a consequence of their larger expression of *trem2* mRNA and p-SYK signaling compared to males.

Microglia TREM2 is necessary for normal motoneuron cell body swelling during the chromatolytic reaction following axotomy.

Adult MNs undergo significant changes following nerve injury and axotomy to transform gene expression and metabolism towards a regenerative phenotype that allows for motor axon regrowth and synaptic reinnervation of muscle (Zhu et al., 2023). Early neuroanatomists hinted at these changes in the cell body in what they defined as the “retrograde” or “chromatolytic” reaction (reviewed in (Fu & Gordon, 1997)). This involves the reorganization of the Nissl substance (composed of ribosomes and the rough endoplasmic reticulum), changing the way the neuron stains with basophilic dyes (thus, chromatolytic). In addition, the nucleus migrated towards the periphery of the cell, and the nucleolus became enlarged, all together suggesting changes in gene expression and RNA metabolism. These changes are associated with a transient cell body swelling of variable time-course and intensity depending on injury type, severity, and location. All these changes were thought to reflect a healthy regenerative response and correlate with the exponential increase in RNA and protein synthesis and the associated modification of metabolic pathways necessary for regeneration (Fu & Gordon, 1997;

Lieberman, 1971). Persistent chromatolysis, however, is thought to precede cell death (Johnson & Sears, 1992). Both the degree of chromatolysis and cell death (analyzed independently) depend on injury severity, proximity to the spinal cord, and nerve type (Brushart & Mesulam, 1980; Fu & Gordon, 1997; Johnson et al., 1985; Johnson & Sears, 1992; Johnson et al., 1993; Lieberman, 1971; Liu & Wang, 2020; Moon, 2018; Pottorf et al., 2022; Seddon, 1943). Because, in mice, transient cell swelling is the most prominent anatomical change informing about changes in the cell body associated with regeneration we quantified cell body cross-sectional areas of Fast Blue nerve-soak-labeled sciatic MNs at 3, 7, 14, 21, and 28 days post-cut-repair and tested whether TREM2 was involved in modulating a normal cell body "retrograde" reaction.

Mouse MNs exhibit a bimodal distribution of cell sizes that combines their small γ-MN and large α-MN populations (Shneider et al., 2009). These two populations can be distinguished by their NeuN-immunoreactivity (Shneider et al., 2009), which corresponds with expression of RBFOX3 or the RNA binding fox-1 homolog splicing factor (Kim et al., 2009), and it is low in γ-MNs and high in α-MNs. We confirmed this distribution in WT naïve mice (N=3; 1 male, 2 females). Lumbar 5 sections from each mouse were immunostained with Choline Acetyltransferase (ChAT) and Neuronal Nuclei (NeuN) antibodies. ChAT+ MNs in the region corresponding to the sciatic motor pool were imaged, classified as low or high NeuN, and quantified (**Figure 11A, Supplemental Statistical Table 22**). Five sections were analyzed per animal, averaging 145.3 ±3.2 (SD) MNs per animal. In these samples, on average, 33.5% ±7.9% were low-NeuN MNs. To obtain cell size distributions, the raw area measurements (see methods) were binned in 50 μm^2 increments for all MNs and, independently, for low and high NeuN MNs (**Figure 11B**). Cell size distributions were fitted to Gaussian curves (**Supplemental Statistical Table 22)**. For model fitting, we pooled together all MNs sampled from the three animals (n=436 MNs, 290 high-NeuN, and 146 low-NeuN). Optimal correlations were obtained with bimodal (n=2) models: 0.8280 for all-MNs, 0.8377 for low-NeuN MNs, and 0.8286 for high-NeuN MNs. The low- and high-size peaks in the all-MN distribution correlated with the low-NeuN and high-NeuN populations, reflecting γ- and α-MNs. The γ-MN peak was estimated at a cross-sectional area of 289.8 μm^2 ±8.4 (SEM). The average area independently estimated for low-NeuN MNs in the three animals was higher (348.4 ±34.1, N=3), and this difference can be best explained by a population of low-NeuN MNs that skew towards larger sizes. The estimated cross-sectional area of the α-MN peak was 738.0 μm^2 ±14.7, which was no different from the average value of all high-NeuN MNs in the three animals (797.6 ±42.7, ±SEM, N=3). These data perfectly replicate our previously published data using different sets of markers for γ-MNs and α-

MNs (Shneider et al., 2009), and were used to compare Fast Blue-labeled sciatic MNs at different times after nerve injury and axotomy.

We used the same WT, GKO, and CKO animals with genetically labeled microglia (**Figure 11B**) from previous analyses, and that underwent nerve injuries and Fast Blue labeling of axotomized MNs from the nerve stumps (N=4, 2 male / 2 female at all time points and genotypes, except for GKO at 28 dpi in which N=3, 1 male and 3 females, and CKO at 21 dpi N=2 females, total N=57 mice). We could not include a sham control group because a nerve cut is necessary to retrogradely label MNs with Fast Blue. We could not test NeuN-immunoreactivity because axotomy downregulates NeuN expression in MNs, and it is not recovered until MNs reinnervate muscles (Alvarez et al., 2011). For this analysis, we constructed cell-size distributions that were then analyzed for the presence of peaks and overall distributions (**Figure 11E, Supplemental Figure 7**). Thereafter, the data was transformed into cumulative plots to statistically test for differences using Kolmogorov-Smirnov (K-S) tests (**Figure 11F**). We compared changes in cell size at 3-, 7-, 14-, 21-, and 28-days post-injury. In all animals, the cell size distributions differed from normal in that the double peak distribution was more smeared, suggesting changes in size in all types of axotomized MNs, as early as 3dpi (**Supplemental Figure 7**). In WTs, we noted a relative reduction in the size of the lower-size peak and a shift of the whole distribution towards larger sizes from 3 to 14 dpi, and then a return at 28 days towards the 3-day distribution. Thus, estimates of average sizes increased from 3 to 14 dpi by 17.3% in the low peak and 24.4% in the high peak, returning towards the 3 days value at 28 days (low size peak: 3 dpi, 394.2 ±15.2; 7 dpi, 424.1 ±18.1; 14 dpi 462.3 ±40.0; 21 dpi, 271.6 ±6.5; 28 dpi 310.7 ±16.5; high size peak: 3 dpi, 823.9 ±18.6; 7 dpi, 893.2 ±52.5; 14 dpi 1024.8 ±35.9; 21 dpi, 805.8 ±18.8' 28 dpi 779.9 ±22.2, all in μm^2). These changes were blunted in GKO and CKO animals (at 14 dpi the low peak estimates were 359.0 ±17.6 in GKO and 261.0 ±7.3 in CKO mice; the high peak estimates were 893.7 ±30.1 in GKO and 755.3 ±15.6 in CKO mice; **Supplementary Statistical Table 23**). Correspondingly, K-S tests indicated that cell size distributions at 7 and 14 days were significantly different from all others in WTs, but not in GKO or CKO animals (**Figure 11F**; **Supplementary Statistical Table 24**).

Examination of the size distributions suggested that a major change occurred in cells larger than 1,000 μm^2 in cell area and corresponding to cell swelling in the α-MN group. Thus, we calculated the percentage of MNs with areas larger than 1,000 μm^2 in all animals and tested for significant differences according to time after injury (dpi) and genotype (**Figure 11D**). A two-way ANOVA for both variables returned statistical differences for both ($p<0.0001$), and post-hoc Bonferroni tests found statistically significant differences from 3 dpi to 7 and 14 dpi in WTs

returning towards baseline at 21 and 28 dpi (**Supplementary Statistical Table 25**). In contrast, the change in cell size was less in GKO and CKO, in which significance was only detected between extreme post-injury times (3 and 28 dpi compared to 14 dpi (**Figure 11D** and **Supplementary Statistical Table 25**). The change in the percentage of MNs with cross-sectional areas larger than 1,000 μm^2 between 3 to 14 dpi was large in WTs (g=4.4) and smaller in GKO (g=0.9) and CKO (g=2.1). Consequently, significant differences in the magnitude of the change occurred when comparing the 14 dpi WTs to GKO and WTs to CKO ($p<0.0001$ in both cases), while there were no significant differences between GKO and CKO mice ($p>0.9999$) (**Figure 11D** and **Supplementary Statistical Table 25**).

In summary, MNs exhibited a transient change in cell size following axotomy, which coincided in time course with the microglial reaction, peaking at 14 days after injury. Moreover, microglial TREM2 modulates the changes in MN cell size, and similar effects were observed whether TREM2 was deleted globally or specifically in microglia prior to the injury.

TREM2 deficiency is detrimental to muscle reinnervation.

Generally, chromatolysis is a positive sign of regeneration initiation. Therefore, we questioned if TREM2 deficiency, which prevented MN cell body swelling, also diminished the degree of muscle reinnervation at eight weeks post-sciatic cut-repair or sham surgeries. To assess muscle innervation, we performed immunohistochemistry for Neurofilament Heavy Chain (NFH), Vesicular Acetylcholine Transporter (VAChT), and alpha Bungarotoxin (α-BTx). Then we quantified the neuromuscular junction (NMJ) area coverage of VAChT (axon terminal) per α-BTx (motor end plate) in the ipsilateral LG muscle (**Figure 12A**). NMJs with over 50% VAChT/ α-BTx were considered fully innervated due to variability in immunohistochemical staining. To estimate the muscle innervation, we calculated the percentage of fully innervated NMJs from 50 NMJs per animal. No sex differences were identified, so males and females were pooled (data not shown). WT and GKO “controls” consisted of sham mice, whereas CKO “controls” were a mix of two sham and one naïve animal to increase the N for statistical analysis (N= 6 WT, 4 GKO, 3 CKO). No significant difference was found between the WT control and cut-repair (N=5) mice for NMJ innervation (p= 6630 via unpaired Two-Way ANOVA with Bonferroni’s post hoc multiple comparison, mean difference = -3.13, -1% difference, hedges’ g= 0.30 [95.0%CI -1.24, 1.42], permutation p = 0.5706) (**Figure 12B-C, Supplemental Statistical Table 26**). This implies that, as expected at this time point (Rotterman et al., 2024), NMJs have been reinnervated following regeneration of motor axons in peripheral nerves.

GKO cut-repair LG muscle had 23% less fully innervated NMJs compared to GKO control animals (N=6 cut-repair; p=0.0525 via unpaired Two-Way ANOVA with Bonferroni's post hoc multiple comparison, mean difference = -15.50, hedges' g = -0.97 [95.0% CI -2.17, 0.24], permutation p= 0.127) (**Figure 12B, Supplemental Statistical Table 26**). CKO cut-repair LG muscle had 54% less fully innervated NMJs compared to CKO control animals (N= 4 cut-repair; p= 0.0005 via unpaired Two-Way ANOVA with Bonferroni's post hoc multiple comparison, mean difference = -36.67, hedges' g=-2.97 [95.0%CI -4.13, -2.32], permutation p<0.0001) (**Figure 12B, Supplemental Statistical Table 26**). When comparing cut-repair LG muscle reinnervation between genotypes, GKO had 37% less, and CKO had 56% less fully innervated NMJs than WT mice (WT versus GKO: p= 0.0022 via Two-Way ANOVA with Bonferroni's post hoc multiple comparisons, mean difference= -27.80, hedges' g= -2.19 [95.0% CI -3.87, -0.83], permutation p = 0.007; WT versus CKO: p= 0.0002 via Two-Way ANOVA with Bonferroni's post hoc multiple comparisons, mean difference= -38.80, hedges' g= -3.68 [95.0%CI -5.35, -2.65], permutation p<0.0001) (**Figure 12B, Supplemental Statistical Table 26**). No significant difference was found between GKO and CKO cut-repair LG muscles for NMJ innervation (p=0.4798 via Two-Way ANOVA with Bonferroni's post hoc multiple comparisons, mean difference = -11.00, -20% difference, hedges' g = -0.747 [95.0% CI -2.01, 0.59], permutation p = 0.2014). These results suggest that in WT mice, NMJs are successfully reinnervated following sciatic cut-repair, but in the absence of TREM2, either globally or microglia-specific, NMJ reinnervation is possibly delayed but definitively diminished at eight weeks post-injury.

Discussion

In this study, we investigated how TREM2 contributed to the microglia heterogeneous interactions with the cell bodies of MNs that have been axotomized as a consequence of nerve injuries. Surprisingly, we found that TREM2 deletions, either globally throughout development or microglia specific just before the nerve injury, did not significantly affect microglia activated morphologies, proliferation, migration towards MN cell bodies, number of interactions with MNs undergoing regeneration or the formation of microglia clusters surrounding dying MNs ("death clusters"). TREM2 knockout did, however, reduce the phagocytic phenotype of microglia in death clusters preferentially in females. It also prevented the cell body swelling characteristic of MNs undergoing regeneration-associated metabolic changes and this correlated with a delay in

muscle reinnervation and NMJ re-occupancy reinnervation. Collectively, the results suggest that TREM2 has a dual function in two different microglia phenotypes associated with axotomized MNs: it promotes regenerative mechanisms in some MNs while facilitates the removal of others undergoing degeneration.

TREM2 deficiency preferentially decreased CD68 in microglia from females and in death clusters.

Our data confirms that TREM2 regulates CD68 expression in activated microglia around axotomized MNs but with interesting sex differences. Increasing evidence shows sexual dimorphisms in microglia from development through healthy aging and disease (Guillot-Sestier et al., 2021; Kang et al., 2024; Kerr et al., 2019; Lenz & McCarthy, 2015; Schwarz et al., 2012). Although males typically have more microglia during development, females exhibit greater pro-inflammatory profiles in adulthood and aging and more abundant DAM in disease models. Here, we present evidence of increased ventral horn microglia activation in females after PNI. In female death clusters, *trem2* mRNA expression and p-SYK levels were significantly higher than in males, suggesting females may have amplified signaling cascade response (**Supplemental Figures 1 & 3**). But regardless of microglia type or injury, female microglia generally showed more elevated CD68 compared to males. Consistent with our findings, Alzheimer's disease and aging rodent models also show that female microglia have higher levels of CD68, phagocytosis (of amyloid Beta), proinflammatory cytokines, and a shift towards glycolytic metabolism (Guillot-Sestier et al., 2021; Kang et al., 2024). We found that TREM2 GKO had a stronger effect on CD68 in death clusters and female microglia. CD68 volume per microglia across all phenotypes, regardless of injury or morphology; however, in males, GKO only decreased CD68 in death clusters. Recently, in a mouse sciatic nerve chronic constriction injury model, RNA sequencing data indicated that at seven days post-injury, dorsal horn female microglia heavily utilize TREM2 and Interferon-γ signaling. In contrast, male microglia predominantly utilize Interferon Regulatory Factor 3 and 7 (IRF3/IRF7) (Fiore et al., 2022). Furthermore, TREM2 activity is routinely reported to be involved in the development and function of DAM (Deczkowska et al., 2018; Keren-Shaul et al., 2017; Samant et al., 2024; H. Wang, 2021). Our results and these recent studies suggest that death clusters and female microglia more predominantly rely on TREM2 signaling to upregulate phagocytic activity while microglia in male may use alternative or parallel signaling mechanisms that compensate for the lack of TREM2 signaling.

TREM2 deficiency prevents motoneuron cell body swelling during the retrograde reaction to axotomy and slows down muscle reinnervation.

The exact significance of microglia enwrapping the cell bodies of MNs in the process of regenerating axons is not fully clear. Whether microglia interactions favor the regenerative properties of axotomized MNs and motor axon growth has been controversial. One early study noted that microglia surrounding axotomized MNs are enriched in MHC-II and proposed they promote regeneration by virtue of the capacity of MHC-II expressing microglia for releasing cytokines and growth factors (Gehrmann et al., 1991). This conclusion agrees with one study that diminished the microglia reaction around axotomized MNs by IL-6 deletion and found slower axon growth of facial motor axons after injury (Galiano et al., 2001). A more recent study suggested that microglia release Ciliary Neurotrophic Factor (CNTF) over axotomized hypoglossal MNs to promote their regeneration (Tanaka et al., 2017). Intriguingly, when CNS neurons (that regenerate poorly) were grafted to peripheral nerves their cell bodies became surrounded by microglia and in parallel axon growth was enhanced (Shokouhi et al., 2010). However other studies reached opposite conclusions. Reduction of the microglia reaction around axotomized MNs by preventing microglia proliferation, reduced CSF1-R expression (*op/op* mice) or tyrosine phosphatase SHP1, a CSF1-R adaptor molecule, all resulted in slower regeneration (Horvat et al., 2001; Kalla et al., 2001; Svensson & Aldskogius, 1993a). However, an alternative explanation is that these manipulations might have affected regulatory pathways that are in fact promoting regeneration. Our results suggest that microglia TREM2 is necessary for MN cell body swelling two weeks after injury which is part of the typical retrograde cell body reaction traditionally associated with increased RNA metabolism and protein synthesis (Lieberman, 1971). In parallel, there was reduced reinnervation of NMJs at eight weeks post-injury, suggesting possible delays in axon regeneration. The results were duplicated in TREM2 global knockouts or microglia cell-specific knockouts ruling out explanations based on the known function of TREM2 regulating Schwann cell regenerative phenotypes (Zhang et al., 2024). This suggests a pro-regenerative role for TREM2 mechanisms in microglia associated to regenerating MNs. However, we also noted that these microglia can transition into death cluster microglia and in this case TREM2 functions promoting MN removal. Therefore, microglia phenotypes and TREM2 function might be part of a continuum form pro-regenerative to pro-phagocytic depending on the health status signaled by the MN. One interesting study showed that pituitary adenylyl-cyclase-activating peptide (PACA) is unregulated in axotomized MNs and modulates the microglia reaction around them. Mice lacking PACA had an exaggerated

microglia reaction and in this case axon regeneration was impaired, although without increased MN loss (Armstrong et al., 2008)..

Microglia have been reported to monitor and modify neuronal bioenergetics. In healthy adult murine cortex, surveying microglia monitor neuronal health through specialized microglia-neuron junctions that form transiently. These are formed between Kv2.1 clusters on neuronal membranes and P2Y12 receptor clusters in microglia and sample the state of neuronal mitochondria (Cserép et al., 2020). Preventing the formation of these specialized microglia-neuron contacts through P2RY12 deficiency hampered mitochondrial function. Moreover, after an acute injury the numbers of microglia contacts increased and were shown to be neuroprotective by regulation of neuronal calcium homeostasis. The authors propose that microglia routinely monitor neuronal status via purinergic sampling, enabling rapid response and support to neurons following injury. Whether similar mechanisms operate on regenerating MNs is unknown, but microglial TREM2 has been shown to favor neuronal mitochondrial metabolism in developing murine hippocampal CA1 pyramidal neurons, as TREM2 deficiency causes deficits in neuronal bioenergetics, abnormal mitochondrial ultrastructure, and delayed maturation (Tagliatti et al., 2024).

Limitations of the Study

Our findings suggest that death cluster microglia surround and consume degenerating MNs; however, we did not examine which MNs are dying. In Amyotrophic Lateral Sclerosis and Spinal Muscular Atrophy, γ-MNs are spared from degeneration (Lalancette-Hebert et al., 2016; Powis & Gillingwater, 2016; Ragagnin et al., 2019). However, γ-MN survival during development is dependent on Glia-Derived Neurotrophic Factor (GDNF) released by muscle spindles (Shneider et al., 2009), suggesting that with prolonged denervation, γ-MNs may be more susceptible to cell death. If this was the case deletion of a subgroup if g-MNs would be a further mechanism disrupting proprioception after nerve injury. However, due to the downregulation of NeuN following axotomy in all MNs (Alvarez et al., 2011), we were unable to critically assess what specific subtypes were susceptible to cell death and targeted by microglia in death clusters. Future studies will be directed to specifically identify the nature of dying MNs.

The formation of microglia death clusters is TREM2-independent, but TREM2 deficiency alters death cluster phagocytic activity. The exact signals that regulate TREM2 promotion of phagocytosis in death cluster was not explored. TREM2 recognizes numerous neuronal apoptotic signals like ePtdSer and nucleic acids (Cannon et al., 2012; Kawabori et al., 2015; Kober et al., 2021; Shirotani et al., 2019; Wang et al., 2015). Future experimentation is needed

to determine what MN signals induce death cluster formation, and which injury ligands modulate TREM2 activity within this phagocytic hubs.

Conclusions

Collectively, we characterize two prominent microglia morphologies that arise depending on interacting with surviving or degenerating MNs following PNI. Although these different activated microglia phenotypes are not dependent on the presence of TREM2, their function seems modulated by TREM2. Microglia that form “death clusters” and surround dying/degenerated MNs have significantly greater levels of TREM2 and CD68 and TREM2 deficiency alters microglia phagocytic function specifically in death clusters and female microglia. Lastly, TREM2 deficiency disrupts the retrograde MN cell body recation to axotomy and slows the rate of muscle reinnervation. Our results lay the groundwork for developing therapeutic interventions for improved functional recovery following axotomy by demonstrating the complexity of microglia-MN interactions and TREM2 involvement.

Author Contributions

Conceptualization, T.S.P. and F.J.A.; methodology, T.S.P, Z.H-J., E.L.L., and F.J.A.; validation, T.S.P., P.C.T., and F.J.A.; formal analysis, T.S.P., E.L.L., D.N.U., V.A.S., and F.J.A.; investigation, T.S.P., E.L.L., Z.H-J., D.N.U., V.A.S., P.C.T., and F.J.A.; resources, F.J.A.; data curation, T.S.P, and F.J.A; writing – original draft, T.S.P., and F.J.A.; writing – review & editing, T.S.P., E.L.L., and F.J.A.; visualization, T.S.P, and F.J.A.; supervision, F.J.A.; project administration, F.J.A.; funding acquisition, T.S.P., and F.J.A.

Acknowledgments

This work was supported by NIH-NINDS grant R01NS111969 (F.J.A.), NIH Training Grant in Integrative Biology T32NS096050-26 (T.S.P.), and Ruth L.
Kirschstein NRSA fellowship F31NS130993 (T.S.P.). During this study, P.C.T. was a Summer Opportunity for Academic Research (SOAR) fellow supported by Emory University College. The two-photon microscope and some of the imaging analysis packages used in this study were made available by the Emory University Integrated Cellular Imaging Core, supported in part by NINDS Core facilities grant P30NS055077. We would also like to acknowledge Dr. Ronald Griffith (Emory University, Atlanta, GA, USA) for his training in surgery techniques, Dr. Srikant Rangaraju (Yale, New Haven, CT, USA) for donating the IBA1-rabbit antibody, Dr. Patricia (Jill) Ward (Emory University, Atlanta, GA, USA) for providing various reagents as needed, Dr. David Katz (Emory University, Atlanta, GA, USA) for providing the TREM2 GKO mouse (Jax #027197), Yu Bai (Katz lab) for performing PCR genotyping as needed, and Dr. Bruce Lamb (University of Indiana, Bloomington, IN, USA) for providing the TREM2 cre mouse (Jax #029853).

Disclosures

The authors disclose that there are no conflicts of interest.

Data Sharing

All the data described was included in the manuscript and a full report of statistics is found in Supplemental Statistical Tables. Once accepted for publication raw data for each analysis will be uploaded to EmoryDataverse

REFERENCES

Akhter, E. T., Rotterman, T. M., English, A. W., & Alvarez, F. J. (2019). Sciatic nerve cut and repair using fibrin glue in adult mice. *Bio-protocol*, *9*(18), e3363-e3363.

Alvarez, F. J., Bullinger, K. L., Titus, H. E., Nardelli, P., & Cope, T. C. (2010). Permanent reorganization of Ia afferent synapses on motoneurons after peripheral nerve injuries. *Annals of the New York Academy of Sciences*, *1198*, 231-241. https://doi.org/10.1111/j.1749-6632.2010.05459.x

Alvarez, F. J., Rotterman, T. M., Akhter, E. T., Lane, A. R., English, A. W., & Cope, T. C. (2020). Synaptic Plasticity on Motoneurons After Axotomy: A Necessary Change in Paradigm [Review]. *Frontiers in Molecular Neuroscience*, *13*(68). https://doi.org/10.3389/fnmol.2020.00068

Alvarez, F. J., Titus-Mitchell, H. E., Bullinger, K. L., Kraszpulski, M., Nardelli, P., & Cope, T. C. (2011). Permanent central synaptic disconnection of proprioceptors after nerve injury and regeneration. I. Loss of VGLUT1/IA synapses on motoneurons. *Journal of Neurophysiology*, *106*(5), 2450-2470. https://doi.org/10.1152/jn.01095.2010

Armstrong, B. D., Abad, C., Chhith, S., Cheung-Lau, G., Hajji, O. E., Nobuta, H., & Waschek, J. A. (2008). Impaired nerve regeneration and enhanced neuroinflammatory response in mice lacking pituitary adenylyl cyclase activating peptide. *Neuroscience*, *151*(1), 63-73. https://doi.org/10.1016/j.neuroscience.2007.09.084

Berg, A., Zelano, J., Thams, S., & Cullheim, S. (2013). The extent of synaptic stripping of motoneurons after axotomy is not correlated to activation of surrounding glia or downregulation of postsynaptic adhesion molecules. *PLoS One*, *8*(3), e59647. https://doi.org/10.1371/journal.pone.0059647

Bilimoria, P. M., & Stevens, B. (2015). Microglia function during brain development: New insights from animal models. *Brain Research*, *1617*, 7-17. https://doi.org/https://doi.org/10.1016/j.brainres.2014.11.032

Blinzinger, K., & Kreutzberg, G. (1968). Displacement of synaptic terminals from regenerating motoneurons by microglial cells. *Z Zellforsch Mikrosk Anat*, *85*(2), 145-157. http://www.ncbi.nlm.nih.gov/pubmed/5706753

Brown, G. C. (2024). Cell death by phagocytosis. *Nat Rev Immunol*, *24*(2), 91-102. https://doi.org/10.1038/s41577-023-00921-6

Brown, G. C., & Vilalta, A. (2015). How microglia kill neurons. *Brain Research*, *1628*, 288-297. https://doi.org/https://doi.org/10.1016/j.brainres.2015.08.031

Bruce-Keller, A. J. (1999). Microglial–neuronal interactions in synaptic damage and recovery. *Journal of Neuroscience Research*, *58*(1), 191-201. https://doi.org/https://doi.org/10.1002/(SICI)1097-4547(19991001)58:1<191::AID-JNR17>3.0.CO;2-E

Brushart, T. M., & Mesulam, M.-M. (1980). Alteration in connections between muscle and anterior horn motoneurons after peripheral nerve repair. *Science*, *208*(4444), 603-605.

Butler, C. A., Popescu, A. S., Kitchener, E. J. A., Allendorf, D. H., Puigdellivol, M., & Brown, G. C. (2021). Microglial phagocytosis of neurons in neurodegeneration, and its regulation. *J Neurochem*, *158*(3), 621-639. https://doi.org/10.1111/jnc.15327

Cannon, J. P., O'Driscoll, M., & Litman, G. W. (2012). Specific lipid recognition is a general feature of CD300 and TREM molecules. *Immunogenetics*, *64*, 39-47.

Cantoni, C., Bollman, B., Licastro, D., Xie, M., Mikesell, R., Schmidt, R., Yuede, C. M., Galimberti, D., Olivecrona, G., & Klein, R. S. (2015). TREM2 regulates microglial cell activation in response to demyelination in vivo. *Acta neuropathologica*, *129*, 429-447.

Cattin, A.-L., Burden, J. J., Van Emmenis, L., Mackenzie, F. E., Hoving, J. J., Calavia, N. G., Guo, Y., McLaughlin, M., Rosenberg, L. H., & Quereda, V. (2015). Macrophage-induced blood vessels guide Schwann cell-mediated regeneration of peripheral nerves. *Cell*, *162*(5), 1127-1139.

Chen, B., Chen, Q., Parkinson, D. B., & Dun, X.-p. (2019). Analysis of Schwann cell migration and axon regeneration following nerve injury in the sciatic nerve bridge. *Frontiers in Molecular Neuroscience*, *12*, 308.

Chen, Y., Kou, Y., Ni, Y., Yang, H., Xu, C., Fan, H., & Liu, H. (2025). Microglia efferocytosis: an emerging mechanism for the resolution of neuroinflammation in Alzheimer's disease. *Journal of Neuroinflammation*, *22*(1), 96.

Colonna, M. (2023). The biology of TREM receptors. *Nature Reviews Immunology*, 1-15.

Cserép, C., Pósfai, B., Lénárt, N., Fekete, R., László, Z. I., Lele, Z., Orsolits, B., Molnár, G., Heindl, S., Schwarcz, A. D., Ujvári, K., Környei, Z., Tóth, K., Szabadits, E., Sperlágh, B., Baranyi, M., Csiba, L., Hortobágyi, T., Maglóczky, Z., Martinecz, B., Szabó, G., Erdélyi, F., Szipőcs, R., Tamkun, M. M., Gesierich, B., Duering, M., Katona, I., Liesz, A., Tamás, G., & Dénes, Á. (2020). Microglia monitor and protect neuronal function through specialized somatic purinergic junctions. *Science*, *367*(6477), 528-537.

Deczkowska, A., Keren-Shaul, H., Weiner, A., Colonna, M., Schwartz, M., & Amit, I. (2018). Disease-associated microglia: a universal immune sensor of neurodegeneration. *Cell*, *173*(5), 1073-1081.

Dukkipati, S. S., Chihi, A., Wang, Y., & Elbasiouny, S. M. (2017). Experimental Design and Data Analysis Issues Contribute to Inconsistent Results of C-Bouton Changes in Amyotrophic Lateral Sclerosis. *eNeuro*, *4*(1). https://doi.org/10.1523/eneuro.0281-16.2016

Ennerfelt, H., Frost, E. L., Shapiro, D. A., Holliday, C., Zengeler, K. E., Voithofer, G., Bolte, A. C., Lammert, C. R., Kulas, J. A., & Ulland, T. K. (2022). SYK coordinates neuroprotective microglial responses in neurodegenerative disease. *Cell*, *185*(22), 4135-4152. e4122.

Filipello, F., Morini, R., Corradini, I., Zerbi, V., Canzi, A., Michalski, B., Erreni, M., Markicevic, M., Starvaggi-Cucuzza, C., & Otero, K. (2018). The microglial innate immune receptor TREM2 is required for synapse elimination and normal brain connectivity. *Immunity*, *48*(5), 979-991. e978.

Fiore, N. T., Yin, Z., Guneykaya, D., Gauthier, C. D., Hayes, J. P., D'Hary, A., Butovsky, O., & Moalem-Taylor, G. (2022). Sex-specific transcriptome of spinal microglia in neuropathic pain due to peripheral nerve injury. *Glia*, *70*(4), 675-696. https://doi.org/10.1002/glia.24133

Fu, S. Y., & Gordon, T. (1997). The cellular and molecular basis of peripheral nerve regeneration. *Molecular neurobiology*, *14*, 67-116.

Galiano, M., Liu, Z. Q., Kalla, R., Bohatschek, M., Koppius, A., Gschwendtner, A., Xu, S., Werner, A., Kloss, C. U., Jones, L. L., Bluethmann, H., & Raivich, G. (2001). Interleukin-6 (IL6) and cellular response to facial nerve injury: effects on lymphocyte recruitment, early microglial activation and axonal outgrowth in IL6-deficient mice. *Eur J Neurosci*, *14*(2), 327-341. https://doi.org/10.1046/j.0953-816x.2001.01647.x

Gehrmann, J., Monaco, S., & Kreutzberg, G. W. (1991). Spinal cord microglial cells and DRG satellite cells rapidly respond to transection of the rat sciatic nerve. *Restor Neurol Neurosci*, *2*(4), 181-198. https://doi.org/10.3233/RNN-1991-245605

Gibbons, H. M., & Dragunow, M. (2006). Microglia induce neural cell death via a proximity-dependent mechanism involving nitric oxide. *Brain Research*, *1084*(1), 1-15. https://doi.org/https://doi.org/10.1016/j.brainres.2006.02.032

Gordon, T. (2020). Peripheral Nerve Regeneration and Muscle Reinnervation. *Int J Mol Sci*, *21*(22). https://doi.org/10.3390/ijms21228652

Guan, Z., Kuhn, J. A., Wang, X., Colquitt, B., Solorzano, C., Vaman, S., Guan, A. K., Evans-Reinsch, Z., Braz, J., & Devor, M. (2016). Injured sensory neuron–derived CSF1 induces microglial proliferation and DAP12-dependent pain. *Nature Neuroscience*, *19*(1), 94-101.

Guillot-Sestier, M. V., Araiz, A. R., Mela, V., Gaban, A. S., O'Neill, E., Joshi, L., Chouchani, E. T., Mills, E. L., & Lynch, M. A. (2021). Microglial metabolism is a pivotal factor in sexual dimorphism in Alzheimer's disease. *Commun Biol*, *4*(1), 711. https://doi.org/10.1038/s42003-021-02259-y

Ho, J., Tumkaya, T., Aryal, S., Choi, H., & Claridge-Chang, A. (2019). Moving beyond P values: data analysis with estimation graphics. *Nature methods*, *16*(7), 565-566.

Hong, S., Beja-Glasser, V. F., Nfonoyim, B. M., Frouin, A., Li, S., Ramakrishnan, S., Merry, K. M., Shi, Q., Rosenthal, A., & Barres, B. A. (2016). Complement and microglia mediate early synapse loss in Alzheimer mouse models. *Science*, *352*(6286), 712-716.

Horvat, A., Schwaiger, F., Hager, G., Brocker, F., Streif, R., Knyazev, P., Ullrich, A., & Kreutzberg, G. W. (2001). A novel role for protein tyrosine phosphatase shp1 in controlling glial activation in the normal and injured nervous system. *J Neurosci*, *21*(3), 865-874. https://doi.org/10.1523/JNEUROSCI.21-03-00865.2001

Hsieh, C. L., Koike, M., Spusta, S. C., Niemi, E. C., Yenari, M., Nakamura, M. C., & Seaman, W. E. (2009). A role for TREM2 ligands in the phagocytosis of apoptotic neuronal cells by microglia. *J Neurochem*, *109*(4), 1144-1156. https://doi.org/10.1111/j.1471-4159.2009.06042.x

Jairaman, A., McQuade, A., Granzotto, A., Kang, Y. J., Chadarevian, J. P., Gandhi, S., Parker, I., Smith, I., Cho, H., & Sensi, S. L. (2022). TREM2 regulates purinergic receptor-mediated calcium signaling and motility in human iPSC-derived microglia. *Elife*, *11*, e73021.

Jay, T. R., von Saucken, V. E., & Landreth, G. E. (2017). TREM2 in neurodegenerative diseases. *Molecular neurodegeneration*, *12*, 1-33.

Jay, T. R., von Saucken, V. E., Muñoz, B., Codocedo, J. F., Atwood, B. K., Lamb, B. T., & Landreth, G. E. (2019). TREM2 is required for microglial instruction of astrocytic synaptic engulfment in neurodevelopment. *Glia*, *67*(10), 1873-1892.

Johnson, I., Pullen, A., & Sears, T. (1985). Target dependence of Nissl body ultrastructure in cat thoracic motoneurones. *Neuroscience letters*, *61*(1-2), 201-205.

Johnson, I., & Sears, T. (1992). Differences in the ultrastructure of Nissl bodies in cat thoracic motoneurons after exposing intercostal nerves to different peripheral environments. *Journal of Anatomy*, *180*, 377.

Johnson, I., Simaika, Y., & Sears, T. (1993). Ultrastructure of γ-motoneurons after temporary or permanent interruption of peripheral target contact. *Brain Research*, *631*(2), 337-344.

Kaiser, T., & Feng, G. (2019). Tmem119-EGFP and Tmem119-CreERT2 transgenic mice for labeling and manipulating microglia. *eNeuro*, *6*(4).

Kalla, R., Liu, Z., Xu, S., Koppius, A., Imai, Y., Kloss, C. U., Kohsaka, S., Gschwendtner, A., Moller, J. C., Werner, A., & Raivich, G. (2001). Microglia and the early phase of immune surveillance in the axotomized facial motor nucleus: impaired microglial activation and lymphocyte recruitment but no effect on neuronal survival or axonal regeneration in macrophage-colony stimulating factor-deficient mice. *J Comp Neurol*, *436*(2), 182-201. https://www.ncbi.nlm.nih.gov/pubmed/11438923

Kang, S., Ko, E. Y., Andrews, A. E., Shin, J. E., Nance, K. J., Barman, P. K., Heeger, P. S., Freeman, W. M., Benayoun, B. A., & Goodridge, H. S. (2024). Microglia undergo sex-dimorphic transcriptional and metabolic rewiring during aging. *J Neuroinflammation*, *21*(1), 150. https://doi.org/10.1186/s12974-024-03130-7

Kawabori, M., Kacimi, R., Kauppinen, T., Calosing, C., Kim, J. Y., Hsieh, C. L., Nakamura, M. C., & Yenari, M. A. (2015). Triggering receptor expressed on myeloid cells 2 (TREM2) deficiency attenuates phagocytic activities of microglia and exacerbates ischemic damage in experimental stroke. *Journal of Neuroscience*, *35*(8), 3384-3396.

Keren-Shaul, H., Spinrad, A., Weiner, A., Matcovitch-Natan, O., Dvir-Szternfeld, R., Ulland, T. K., David, E., Baruch, K., Lara-Astaiso, D., & Toth, B. (2017). A unique microglia type associated with restricting development of Alzheimer's disease. *Cell*, *169*(7), 1276-1290. e1217.

Kerr, N., Dietrich, D. W., Bramlett, H. M., & Raval, A. P. (2019). Sexually dimorphic microglia and ischemic stroke. *CNS Neurosci Ther*, *25*(12), 1308-1317. https://doi.org/10.1111/cns.13267

Kim, K. K., Adelstein, R. S., & Kawamoto, S. (2009). Identification of neuronal nuclei (NeuN) as Fox-3, a new member of the Fox-1 gene family of splicing factors. *J Biol Chem*, *284*(45), 31052-31061. https://doi.org/10.1074/jbc.M109.052969

Kober, D. L., Stuchell-Brereton, M. D., Kluender, C. E., Dean, H. B., Strickland, M. R., Steinberg, D. F., Nelson, S. S., Baban, B., Holtzman, D. M., & Frieden, C. (2021). Functional insights from biophysical study of TREM2 interactions with apoE and Aβ1-42. *Alzheimer's & Dementia*, *17*(3), 475-488.

Konishi, H., & Kiyama, H. (2018). Microglial TREM2/DAP12 Signaling: A Double-Edged Sword in Neural Diseases [Review]. *Frontiers in Cellular Neuroscience*, *12*(206). https://doi.org/10.3389/fncel.2018.00206

Lai, A. Y., & Todd, K. G. (2008). Differential regulation of trophic and proinflammatory microglial effectors is dependent on severity of neuronal injury. *Glia*, *56*(3), 259-270. https://doi.org/https://doi.org/10.1002/glia.20610

Lalancette-Hebert, M., Sharma, A., Lyashchenko, A. K., & Shneider, N. A. (2016). Gamma motor neurons survive and exacerbate alpha motor neuron degeneration in ALS. *Proceedings of the National Academy of Sciences*, *113*(51), E8316-E8325.

Lee, J.-W., Lee, I.-H., Iimura, T., & Kong, S. W. (2021). Two macrophages, osteoclasts and microglia: from development to pleiotropy. *Bone Research*, *9*(1), 11. https://doi.org/10.1038/s41413-020-00134-w

Lenz, K. M., & McCarthy, M. M. (2015). A starring role for microglia in brain sex differences. *Neuroscientist*, *21*(3), 306-321. https://doi.org/10.1177/1073858414536468

Lieberman, A. (1971). The axon reaction: a review of the principal features of perikaryal responses to axon injury. *International review of neurobiology*, *14*, 49-124.

Liu, Y., & Wang, H. (2020). Peripheral nerve injury induced changes in the spinal cord and strategies to counteract/enhance the changes to promote nerve regeneration. *Neural Regeneration Research*, *15*(2), 189-198. https://doi.org/10.4103/1673-5374.265540

Marin-Teva, J. L., Sepulveda, M. R., Neubrand, V. E., & Cuadros, M. A. (2024). Microglial Phagocytosis During Embryonic and Postnatal Development. *Adv Neurobiol*, *37*, 151-161. https://doi.org/10.1007/978-3-031-55529-9_9

Matteoli, M. (2024). The role of microglial TREM2 in development: A path toward neurodegeneration? *Glia*, *72*(9), 1544-1554. https://doi.org/https://doi.org/10.1002/glia.24574

Mazaheri, F., Snaidero, N., Kleinberger, G., Madore, C., Daria, A., Werner, G., Krasemann, S., Capell, A., Trümbach, D., & Wurst, W. (2017). TREM 2 deficiency impairs chemotaxis and microglial responses to neuronal injury. *EMBO reports*, *18*(7), 1186-1198.

Moon, L. D. F. (2018). Chromatolysis: Do injured axons regenerate poorly when ribonucleases attack rough endoplasmic reticulum, ribosomes and RNA? *Dev Neurobiol*, *78*(10), 1011-1024. https://doi.org/10.1002/dneu.22625

Nimmerjahn, A., Kirchhoff, F., & Helmchen, F. (2005). Resting microglial cells are highly dynamic surveillants of brain parenchyma in vivo. *Science*, *308*(5726), 1314-1318. https://doi.org/10.1126/science.1110647

Olah, M., Menon, V., Habib, N., Taga, M. F., Ma, Y., Yung, C. J., Cimpean, M., Khairallah, A., Coronas-Samano, G., & Sankowski, R. (2020). Single cell RNA sequencing of human microglia uncovers a subset associated with Alzheimer’s disease. *Nature communications*, *11*(1), 6129.

Olsson, Y., & Sjöstrand, J. (1969). Origin of macrophages in Wallerian degeneration of peripheral nerves demonstrated autoradiographically. *Experimental Neurology*, *23*(1), 102-112.

Pereira-Iglesias, M., Maldonado-Teixido, J., Melero, A., Piriz, J., Galea, E., Ransohoff, R. M., & Sierra, A. (2025). Microglia as hunters or gatherers of brain synapses. *Nat Neurosci*, *28*(1), 15-23. https://doi.org/10.1038/s41593-024-01818-w

Pettas, S., Karagianni, K., Kanata, E., Chatziefstathiou, A., Christoudia, N., Xanthopoulos, K., Sklaviadis, T., & Dafou, D. (2022). Profiling microglia through single-cell RNA sequencing over the course of development, aging, and disease. *Cells*, *11*(15), 2383.

Piccioni, G., Mango, D., Saidi, A., Corbo, M., & Nisticò, R. (2021). Targeting microglia-synapse interactions in Alzheimer's disease. *International journal of molecular sciences*, *22*(5), 2342.

Pottorf, T. S., Rotterman, T. M., McCallum, W. M., Haley-Johnson, Z. A., & Alvarez, F. J. (2022). The Role of Microglia in Neuroinflammation of the Spinal Cord after Peripheral Nerve Injury. *Cells*, *11*(13), 2083.

Powis, R. A., & Gillingwater, T. H. (2016). Selective loss of alpha motor neurons with sparing of gamma motor neurons and spinal cord cholinergic neurons in a mouse model of spinal muscular atrophy. *J Anat*, *228*(3), 443-451. https://doi.org/10.1111/joa.12419

Qu, W., & Li, L. (2020). Loss of TREM2 Confers Resilience to Synaptic and Cognitive Impairment in Aged Mice. *J Neurosci*, *40*(50), 9552-9563. https://doi.org/10.1523/jneurosci.2193-20.2020

Ragagnin, A. M. G., Shadfar, S., Vidal, M., Jamali, M. S., & Atkin, J. D. (2019). Motor Neuron Susceptibility in ALS/FTD. *Front Neurosci*, *13*, 532. https://doi.org/10.3389/fnins.2019.00532

Rajendran, L., & Paolicelli, R. C. (2018). Microglia-mediated synapse loss in Alzheimer's disease. *Journal of Neuroscience*, *38*(12), 2911-2919.

Rios, R., Jablonka-Shariff, A., Broberg, C., & Snyder-Warwick, A. K. (2021). Macrophage roles in peripheral nervous system injury and pathology: Allies in neuromuscular junction recovery. *Molecular and Cellular Neuroscience*, *111*, 103590.

Rotterman, T. M., Akhter, E. T., Lane, A. R., MacPherson, K. P., García, V. V., Tansey, M. G., & Alvarez, F. J. (2019). Spinal Motor Circuit Synaptic Plasticity after Peripheral Nerve Injury Depends on Microglia Activation and a CCR2 Mechanism. *The Journal of Neuroscience*, *39*(18), 3412-3433. https://doi.org/10.1523/jneurosci.2945-17.2019

Rotterman, T. M., & Alvarez, F. J. (2020). Microglia dynamics and interactions with motoneurons axotomized after nerve injuries revealed by two-photon imaging. *Scientific Reports*, *10*(1), 1-22.

Rotterman, T. M., Haley-Johnson, Z., Pottorf, T. S., Chopra, T., Chang, E., Zhang, S., McCallum, W. M., Fisher, S., Franklin, H., & Alvarez, M. (2024). Modulation of central synapse remodeling after remote peripheral injuries by the CCL2-CCR2 axis and microglia. *Cell reports*, *43*(2).

Rueda-Carrasco, J., Sokolova, D., Lee, S. E., Childs, T., Jurčáková, N., Crowley, G., De Schepper, S., Ge, J. Z., Lachica, J. I., Toomey, C. E., Freeman, O. J., Hardy, J., Barnes, S. J., Lashley, T., Stevens, B., Chang, S., & Hong, S. (2023). Microglia-synapse engulfment via PtdSer-TREM2 ameliorates neuronal hyperactivity in Alzheimer's disease models. *Embo j*, *42*(19), e113246. https://doi.org/10.15252/embj.2022113246

Salvany, S., Casanovas, A., Piedrafita, L., Tarabal, O., Hernandez, S., Caldero, J., & Esquerda, J. E. (2021). Microglial recruitment and mechanisms involved in the disruption of afferent synaptic terminals on spinal cord motor neurons after acute peripheral nerve injury. *Glia*, *69*(5), 1216-1240. https://doi.org/10.1002/glia.23959

Samant, R. R., Standaert, D. G., & Harms, A. S. (2024). The emerging role of disease-associated microglia in Parkinson's disease [Mini Review]. *Frontiers in Cellular Neuroscience*, *Volume 18 - 2024*. https://doi.org/10.3389/fncel.2024.1476461

Sasaki, A., Yamaguchi, H., Ogawa, A., Sugihara, S., & Nakazato, Y. (1997). Microglial activation in early stages of amyloid β protein deposition. *Acta neuropathologica*, *94*, 316-322.

Sayed, F. A., Telpoukhovskaia, M., Kodama, L., Li, Y., Zhou, Y., Le, D., Hauduc, A., Ludwig, C., Gao, F., & Clelland, C. (2018). Differential effects of partial and complete loss of TREM2 on microglial injury response and tauopathy. *Proceedings of the National Academy of Sciences*, *115*(40), 10172-10177.

Schwarz, J. M., Sholar, P. W., & Bilbo, S. D. (2012). Sex differences in microglial colonization of the developing rat brain. *J Neurochem*, *120*(6), 948-963. https://doi.org/10.1111/j.1471-4159.2011.07630.x

Scott-Hewitt, N., Perrucci, F., Morini, R., Erreni, M., Mahoney, M., Witkowska, A., Carey, A., Faggiani, E., Schuetz, L. T., Mason, S., Tamborini, M., Bizzotto, M., Passoni, L., Filipello, F., Jahn, R., Stevens, B., & Matteoli, M. (2020). Local externalization of phosphatidylserine mediates developmental synaptic pruning by microglia. *Embo j*, *39*(16), e105380. https://doi.org/10.15252/embj.2020105380

Seddon, H. (1943). Three types of nerve injury. *Brain*, *66*(4), 237-288.

Sessa, G., Podini, P., Mariani, M., Meroni, A., Spreafico, R., Sinigaglia, F., Colonna, M., Panina, P., & Meldolesi, J. (2004). Distribution and signaling of TREM2/DAP12, the receptor system mutated in human polycystic lipomembraneous osteodysplasia with sclerosing leukoencephalopathy dementia. *Eur J Neurosci*, *20*(10), 2617-2628. https://doi.org/10.1111/j.1460-9568.2004.03729.x

Shirotani, K., Hori, Y., Yoshizaki, R., Higuchi, E., Colonna, M., Saito, T., Hashimoto, S., Saito, T., Saido, T. C., & Iwata, N. (2019). Aminophospholipids are signal-transducing TREM2 ligands on apoptotic cells. *Scientific Reports*, *9*(1), 7508.

Shneider, N. A., Brown, M. N., Smith, C. A., Pickel, J., & Alvarez, F. J. (2009). Gamma motor neurons express distinct genetic markers at birth and require muscle spindle-derived GDNF for postnatal survival. *Neural development*, *4*(1), 1-22.

Shokouhi, B. N., Wong, B. Z., Siddiqui, S., Lieberman, A. R., Campbell, G., Tohyama, K., & Anderson, P. N. (2010). Microglial responses around intrinsic CNS neurons are correlated with axonal regeneration. *BMC Neurosci*, *11*, 13. https://doi.org/10.1186/1471-2202-11-13

Sierra, A., de Castro, F., del Río-Hortega, J., Rafael Iglesias-Rozas, J., Garrosa, M., & Kettenmann, H. (2016). The “Big-Bang” for modern glial biology: Translation and comments on Pío del Río-Hortega 1919 series of papers on microglia. *Glia*, *64*(11), 1801-1840.

Sobue, A., Komine, O., Hara, Y., Endo, F., Mizoguchi, H., Watanabe, S., Murayama, S., Saito, T., Saido, T. C., & Sahara, N. (2021). Microglial gene signature reveals loss of homeostatic microglia associated with neurodegeneration of Alzheimer’s disease. *Acta neuropathologica communications*, *9*, 1-17.

St-Pierre, M.-K., Šimončičová, E., Bögi, E., & Tremblay, M.-È. (2020). Shedding light on the dark side of the microglia. *ASN neuro*, *12*, 1759091420925335.

Stevens, B., Allen, N. J., Vazquez, L. E., Howell, G. R., Christopherson, K. S., Nouri, N., Micheva, K. D., Mehalow, A. K., Huberman, A. D., Stafford, B., Sher, A., Litke, A. M., Lambris, J. D., Smith, S. J., John, S. W., & Barres, B. A. (2007). The classical complement cascade mediates CNS synapse elimination. *Cell*, *131*(6), 1164-1178. https://doi.org/10.1016/j.cell.2007.10.036

Streit, W. J., Walter, S. A., & Pennell, N. A. (1999). Reactive microgliosis. *Progress in neurobiology*, *57*(6), 563-581.

Sun, H., Feng, J., & Tang, L. (2020). Function of TREM1 and TREM2 in liver-related diseases. *Cells*, *9*(12), 2626.

Svensson, M., & Aldskogius, H. (1993a). Regeneration of hypoglossal nerve axons following blockade of the axotomy-induced microglial cell reaction in the rat. *Eur J Neurosci*, *5*(1), 85-94. https://doi.org/10.1111/j.1460-9568.1993.tb00208.x

Svensson, M., & Aldskogius, H. (1993b). Synaptic density of axotomized hypoglossal motorneurons following pharmacological blockade of the microglial cell proliferation. *Exp Neurol*, *120*(1), 123-131. https://doi.org/10.1006/exnr.1993.1046

Szepesi, Z., Manouchehrian, O., Bachiller, S., & Deierborg, T. (2018). Bidirectional Microglia-Neuron Communication in Health and Disease. *Front Cell Neurosci*, *12*, 323. https://doi.org/10.3389/fncel.2018.00323

Tagliatti, E., Desiato, G., Mancinelli, S., Bizzotto, M., Gagliani, M. C., Faggiani, E., Hernández-Soto, R., Cugurra, A., Poliseno, P., Miotto, M., Argüello, R. J., Filipello, F., Cortese, K., Morini, R., Lodato, S., & Matteoli, M. (2024). Trem2 expression in microglia is required to maintain normal neuronal bioenergetics during development. *Immunity*, *57*(1), 86-105.e109. https://doi.org/https://doi.org/10.1016/j.immuni.2023.12.002

Takahashi, K., Rochford, C. D., & Neumann, H. (2005). Clearance of apoptotic neurons without inflammation by microglial triggering receptor expressed on myeloid cells-2. *J Exp Med*, *201*(4), 647-657. https://doi.org/10.1084/jem.20041611

Tanaka, T., Murakami, K., Bando, Y., Nomura, T., Isonishi, A., Morita-Takemura, S., Tatsumi, K., Wanaka, A., & Yoshida, S. (2017). Microglia support ATF3-positive neurons following hypoglossal nerve axotomy. *Neurochem Int*, *108*, 332-342. https://doi.org/10.1016/j.neuint.2017.05.007

Tomlinson, J. E., Žygelytė, E., Grenier, J. K., Edwards, M. G., & Cheetham, J. (2018). Temporal changes in macrophage phenotype after peripheral nerve injury. *Journal of Neuroinflammation*, *15*(1), 1-17.

Vecchiarelli, H. A., Bisht, K., Sharma, K., Weiser Novak, S., Traetta, M. E., Garcia-Segura, M. E., St-Pierre, M.-K., Savage, J. C., Willis, C., & Picard, K. (2024). Dark Microglia Are Abundant in Normal Postnatal Development, where they Remodel Synapses via Phagocytosis and Trogocytosis, and Are Dependent on TREM2. *bioRxiv*, 2024.2010. 2015.618087.

Wang, H. (2021). Microglia heterogeneity in Alzheimer's disease: insights from single-cell technologies. *Frontiers in Synaptic Neuroscience*, *13*, 773590.

Wang, P. L. (2021). *Peripheral Nerve Macrophages and Their Implications in Neuroimmunity* Washington University in St. Louis].

Wang, P. L., Yim, A. K., Kim, K.-W., Avey, D., Czepielewski, R. S., Colonna, M., Milbrandt, J., & Randolph, G. J. (2020). Peripheral nerve resident macrophages share tissue-specific programming and features of activated microglia. *Nature communications*, *11*(1), 2552.

Wang, S., Mustafa, M., Yuede, C. M., Salazar, S. V., Kong, P., Long, H., Ward, M., Siddiqui, O., Paul, R., & Gilfillan, S. (2020). Anti-human TREM2 induces microglia proliferation and reduces pathology in an Alzheimer's disease model. *Journal of Experimental Medicine*, *217*(9), e20200785.

Wang, S., Sudan, R., Peng, V., Zhou, Y., Du, S., Yuede, C. M., Lei, T., Hou, J., Cai, Z., & Cella, M. (2022). TREM2 drives microglia response to amyloid-β via SYK-dependent and-independent pathways. *Cell*, *185*(22), 4153-4169. e4119.

Wang, X., Wang, Y., Yang, L., Zhang, Y., & Yang, L. (2025). TREM2+ macrophages: a key role in disease development [Review]. *Frontiers in Immunology*, *Volume 16 - 2025*. https://doi.org/10.3389/fimmu.2025.1550893

Wang, Y., Cella, M., Mallinson, K., Ulrich, J. D., Young, K. L., Robinette, M. L., Gilfillan, S., Krishnan, G. M., Sudhakar, S., Zinselmeyer, B. H., Holtzman, D. M., Cirrito, J. R., & Colonna, M. (2015). TREM2 lipid sensing sustains the microglial response in an Alzheimer's disease model. *Cell*, *160*(6), 1061-1071. https://doi.org/10.1016/j.cell.2015.01.049

Weinhard, L., di Bartolomei, G., Bolasco, G., Machado, P., Schieber, N. L., Neniskyte, U., Exiga, M., Vadisiute, A., Raggioli, A., Schertel, A., Schwab, Y., & Gross, C. T. (2018). Microglia remodel synapses by presynaptic trogocytosis and spine head filopodia induction. *Nat Commun*, *9*(1), 1228. https://doi.org/10.1038/s41467-018-03566-5

Wilton, D. K., Dissing-Olesen, L., & Stevens, B. (2019). Neuron-Glia Signaling in Synapse Elimination. *Annu Rev Neurosci*, *42*, 107-127. https://doi.org/10.1146/annurev-neuro-070918-050306

Witzel, C., Rohde, C., & Brushart, T. M. (2005). Pathway sampling by regenerating peripheral axons. *Journal of Comparative Neurology*, *485*(3), 183-190.

Wood, Ryan L., Calvo, Paula M., McCallum, William M., English, Arthur W., & Alvarez, Francisco J. (2025). GABA and Glycine Synaptic Release on Axotomized Motoneuron Cell Bodies Promotes Motor

Axon Regeneration. *European Journal of Neuroscience*, *61*(5), e70045. https://doi.org/https://doi.org/10.1111/ejn.70045

Ydens, E., Cauwels, A., Asselbergh, B., Goethals, S., Peeraer, L., Lornet, G., Almeida-Souza, L., Van Ginderachter, J. A., Timmerman, V., & Janssens, S. (2012). Acute injury in the peripheral nervous system triggers an alternative macrophage response. *Journal of Neuroinflammation*, *9*, 1-17.

Yu, C.-J., Wang, M., Li, R.-Y., Wei, T., Yang, H.-C., Yin, Y.-S., Mi, Y.-X., Qin, Q., & Tang, Y. (2023). TREM2 and microglia contribute to the synaptic plasticity: from physiology to pathology. *Molecular neurobiology*, *60*(2), 512-523.

Zhang, N., Ji, Q., Chen, Y., Wen, X., & Shan, F. (2024). TREM2 deficiency impairs the energy metabolism of Schwann cells and exacerbates peripheral neurological deficits. *Cell Death & Disease*, *15*(3), 193. https://doi.org/10.1038/s41419-024-06579-9

Zheng, H., Jia, L., Liu, C.-C., Rong, Z., Zhong, L., Yang, L., Chen, X.-F., Fryer, J. D., Wang, X., & Zhang, Y.-w. (2017). TREM2 promotes microglial survival by activating Wnt/β-catenin pathway. *Journal of Neuroscience*, *37*(7), 1772-1784.

Zhong, L., Sheng, X., Wang, W., Li, Y., Zhuo, R., Wang, K., Zhang, L., Hu, D.-D., Hong, Y., & Chen, L. (2023). TREM2 receptor protects against complement-mediated synaptic loss by binding to complement C1q during neurodegeneration. *Immunity*.

Zhong, L., Xu, Y., Zhuo, R., Wang, T., Wang, K., Huang, R., Wang, D., Gao, Y., Zhu, Y., & Sheng, X. (2019). Soluble TREM2 ameliorates pathological phenotypes by modulating microglial functions in an Alzheimer's disease model. *Nature communications*, *10*(1), 1365.

Zhu, Y., Luan, C., Gong, L., Gu, Y., Wang, X., Sun, H., Chen, Z., Zhou, Q., Liu, C., & Shan, Q. (2023). SnRNA-seq reveals the heterogeneity of spinal ventral horn and mechanism of motor neuron axon regeneration. *Iscience*, *26*(8).

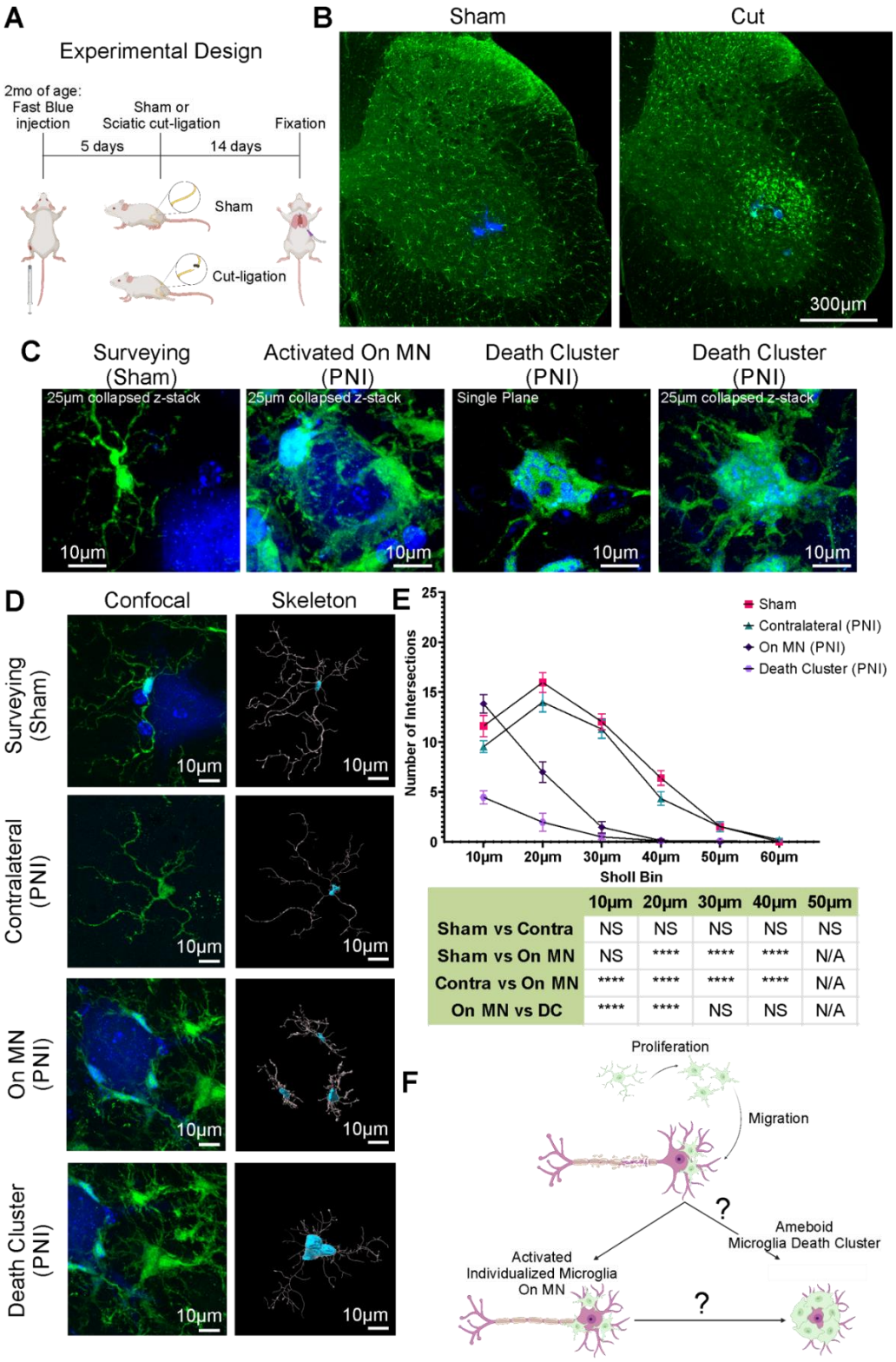

	10µm	20µm	30µm	40µm	50µm
Sham vs Contra	NS	NS	NS	NS	NS
Sham vs On MN	NS	****	****	****	N/A
Contra vs On MN	****	****	****	****	N/A
On MN vs DC	****	****	NS	NS	N/A

Figure 1. Activated microglia display distinct morphologies depending on the health state of the motoneuron they interact with after nerve injury. A) Experimental design. The lateral gastrocnemius muscle of Tmem119^{eGFP} mice was injected with Fast Blue (FB) five days before sciatic nerve surgeries, and the animals were analyzed 14 days post-surgery. We prepared sham and cut-ligation mice (N=6 mice each, equal sex). **B**) Representative low magnification z-stack 2D projection images of lumbar 5 (L5) spinal cord 50 µm thick sections from sham or cut-ligation mice. eGFP microglia (green) proliferate and surround FB+ motoneurons (MN) after nerve injury, but not in sham animals. **C**) High-magnification 2D projections (25 µm thick z-stacks) of microglia (green) close to FB+ MNs in a sham animal, or after PNI on an injured MN or in a death cluster. The interior of the death cluster is also shown in a single confocal plane. **D**) High magnification confocal images and cell skeletonizations of surveying microglia in shams and contralateral cut-ligation animals, and On MN and DC microglia ipsilateral to cut-ligation animals. **E**) Sholl analysis of microglia in each group showing average number of intersections in each Sholl bin ±SEM (n=30 microglia per group, 5 per animal). Processes are retracted in On MN microglia and more so in DC microglia. Summary of two-way ANOVA comparisons for Sholl distance and microglia type ($p<0.0001$ for both) followed by Bonferroni multiple comparisons. Table shows some relevant comparisons; ***$p<0.001$, ***$p<0.0001$. Further details are in **Supplemental Statistical Table 1**. **F**) Alternative hypotheses on the development of different microglia interactions with injured MNs. After activation, microglia proliferate and migrate to the MN cell body surface. On MN and DC microglia phenotypes could be independently triggered on different MNs or alternatively, DC microglia could be an evolution of On MN microglia over a subset of degenerating MNs.

Figure 2

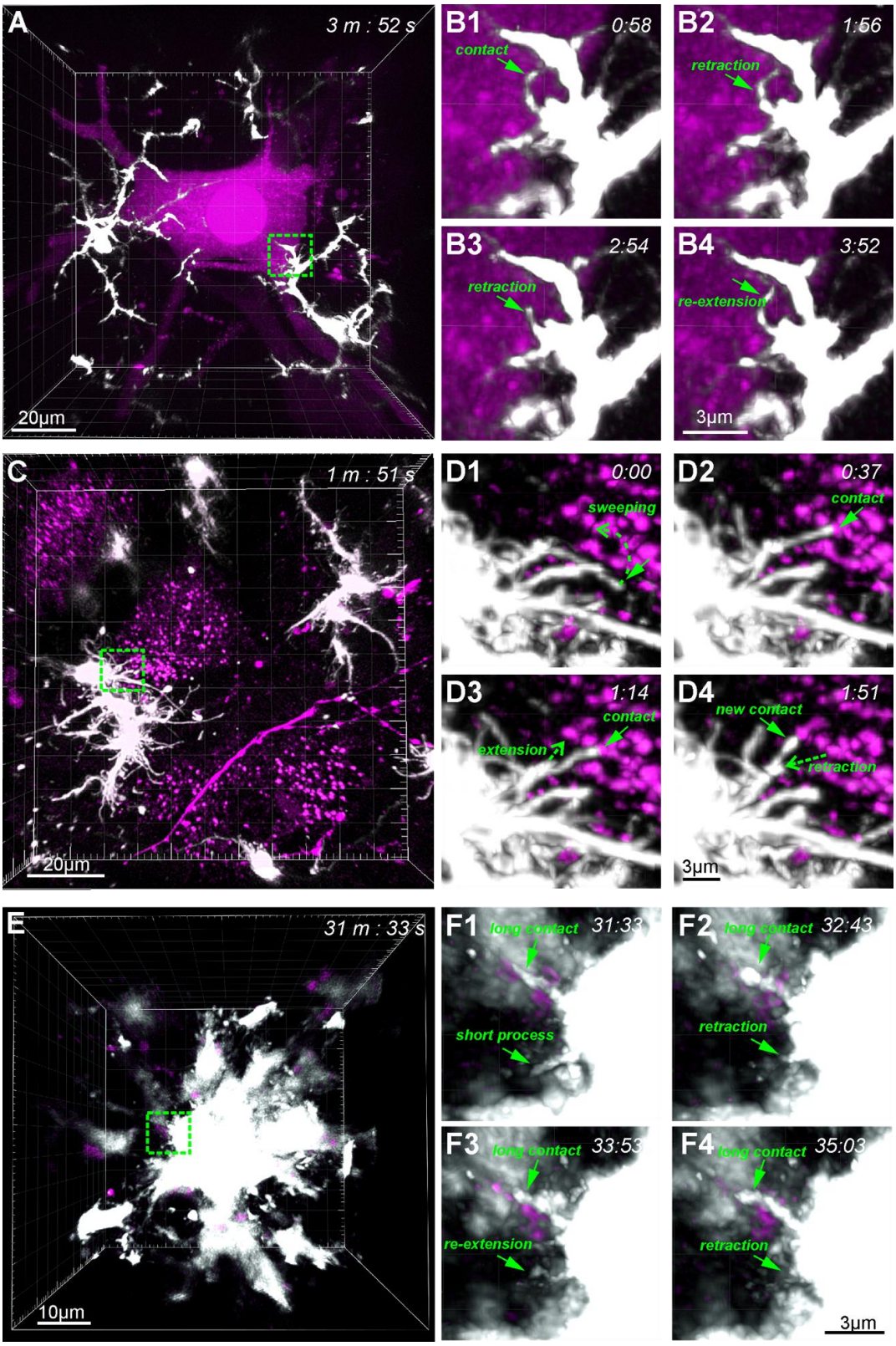
A
3 m : 52 s
20µm
B1
0:58
contact
B2
1:56
retraction
B3
2:54
retraction
B4
3:52
re-extension
3µm
C
1 m : 51 s
20µm
D1
0:00
sweeping
D2
0:37
contact
D3
1:14
contact
extension
D4
1:51
new contact
retraction
3µm
E
31 m : 33 s
10µm
F1
long contact
31:33
short process
F2
long contact
32:43
retraction
F3
long contact
33:53
re-extension
F4
long contact
35:03
retraction
3µm

Figure 2. Two-photon time-lapse microscopy reveals distinct microglia-motoneuron process dynamics depending on the health state of the motoneuron at 14 days post-nerve injury and axotomy. Single frames of time-lapse sequences obtained from *ex vivo* spinal cord slices from the lower lumbar region of CX3CR1^{eGFP} mice imaged at 25x magnification with 4.5-7.5x zoom after sham (**A-B**) or sciatic nerve cut and ligation (**C-F**). Time-lapse sessions lasted for 45 to 60 minutes, and images were collected at a rate of 30 sec to 1 min 25 sec frames per minute. Frame rates depend on the volume imaged and the necessary number of optical sections collected per frame. Lateral gastrocnemius motoneurons (MN) were retrogradely labeled with AAV1-tdTomato (magenta). **A, C, E**) Snapshot images from surveying microglia (**A**), and On MN microglia (**C**) and a death cluster (**E**). Time stamps are indicated in top right corners. **B, D, F**) Examples of microglia process motions magnified from areas indicated in A, C, and E, respectively (yellow dashed boxes). In all cases, four consecutive frames, but at different frame rates: 58 sec in B, 37 sec in D, and 1 min 10 sec in F. The interactions of surveying microglia processes with uninjured MNs are few and short-lived in sham mice (arrows in B1-4). Microglia are closer to injured MNs, and their shorter processes make longer sweeping motions over the MN surface. Dashed curved arrow in D1 shows the motion of one process from frame D1 to D2, and arrows in D2 and D3 indicate a transient contact followed by retraction (dashed line in D4). Resolution of microglia processes was more difficult in DC microglia because of the clusters' high fluorescence. Some examples are shown in F1 to F4.

Figure 3

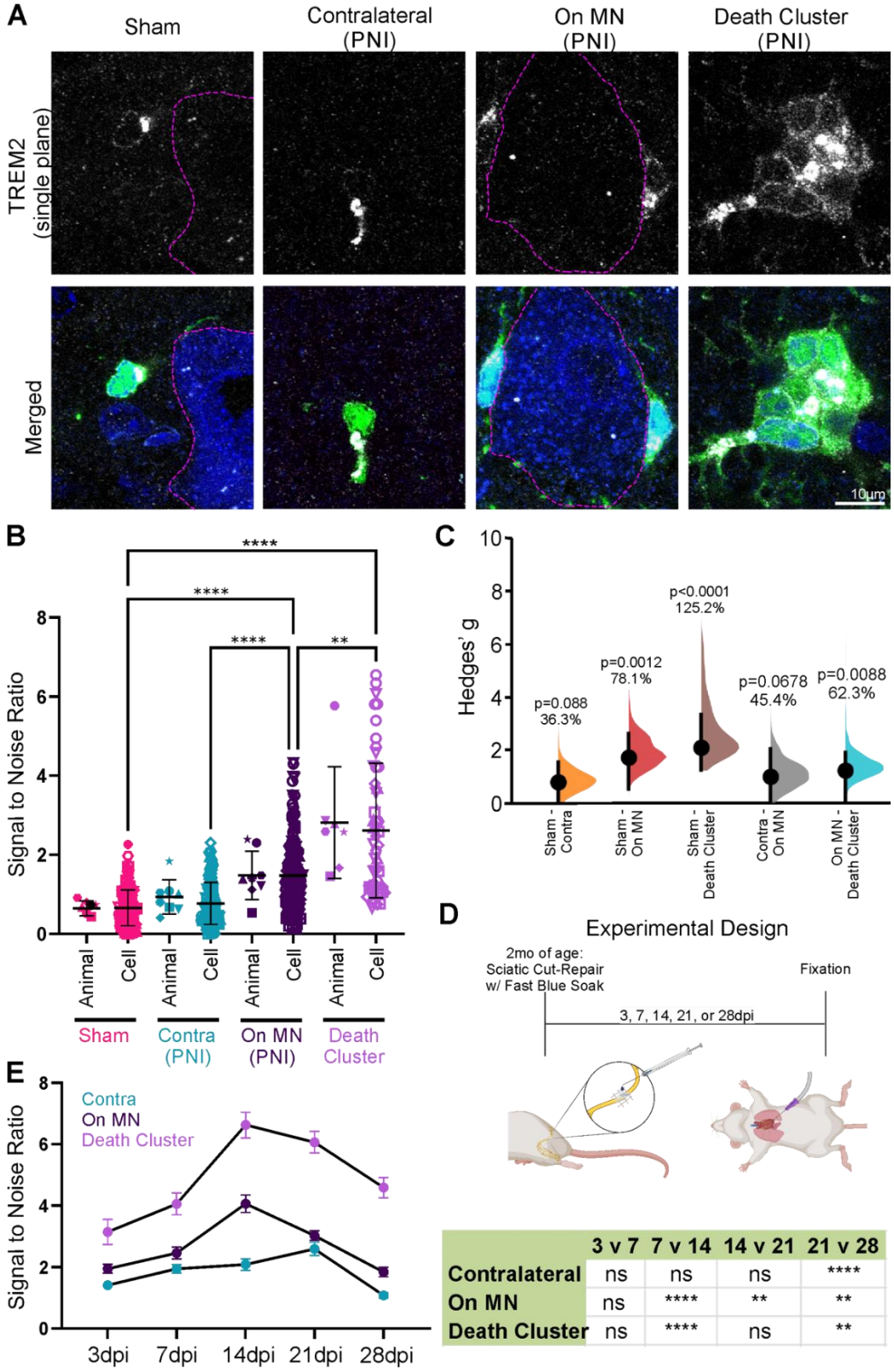

	3 v 7	7 v 14	14 v 21	21 v 28
Contralateral	ns	ns	ns	****
On MN	ns	****	**	**
Death Cluster	ns	****	ns	**

Figure 3. TREM2 expression is highest at 14 days post-injury and in Death Cluster microglia. A) Single plane confocal images of Tmem119^{eGFP} microglia (green) immunolabeled for TREM2 (white) and close to Fast Blue motoneurons (MNs). All microglia display high TREM2 in a patch juxtaposed to the nucleus corresponding to the Golgi (Sessa et al., 2004). Cytoplasmic and membrane TREM2 immunofluorescence increased in activated microglia and was maximal in DC microglia. **B**) TREM2 signal calculated in the membrane and cytosol, corrected for background noise. Individual microglia (Cell) and animal (Animal) averages are shown (n=17-26 microglia per animal and condition, N=8 mice (equal sex) per condition). Each symbol represents one animal or microglia cell. Symbol shapes identify individual animals. Mean±SD are represented. For simplicity, only the most salient Dunn's post-hoc multiple comparisons of Cell data are shown (**p<0.01, ****p<0.0001) (see **Supplemental Statistical Table 2** for other details). **C**) Animal averages analyzed with estimation statistics. Hedge's g of mean differences represented by Cumming plots with bootstrap sampling distributions. Dots show means; vertical error bars 95% confidence intervals. Percentage differences and significance (permutation t-tests) are indicated on each graph. **D**) Experimental design for time course analysis of TREM2 expression. These animals had regeneration allowed after a sciatic nerve cut and repair surgery. N=4 animal at each dpi, n=20 microglia analyzed per animal for On MN and contralateral MNs. Each time point includes 72 to 79 microglia. Death cluster recovery varied: 3 dpi n=16, N=1; 7 dpi n=29, N=2; 14 dpi n=80, N=4; 21 dpi n=48 N=3; 28 dpi n=37, N=2. **E**) TREM2 immunofluorescence at different days post injury (dpi) in microglia located in the contralateral ventral horn, or ipsilateral On MN and DC microglia. Mean±SEM of the Cell data. Ipsilateral to nerve injuries, TREM2 expression peaks at 14 dpi and DC microglia exhibit higher TREM2 and takes longer to decay. Two-way ANOVA (type of microglia and dpi) showed significance for both variables (p<0.001). Table at right shows significance at different time points by Bonferroni tests (details of samples and statistics in **Supplemental Statistical Table 3**).

Figure 4

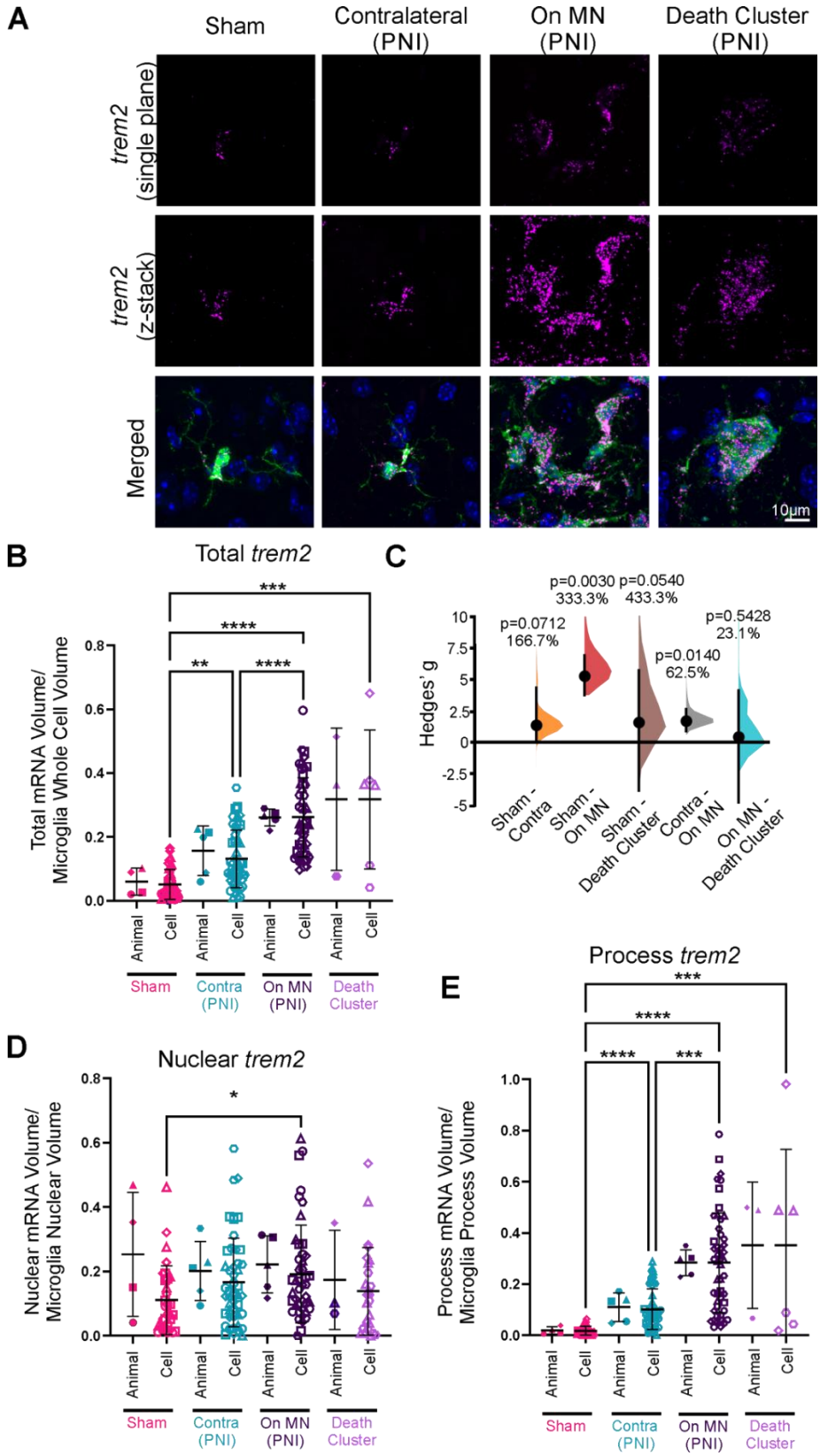
A
Sham
Contralateral (PNI)
On MN (PNI)
Death Cluster (PNI)
trem2 (single plane)
trem2 (z-stack)
Merged
10µm
B
Total trem2
Total mRNA Volume/ Microglia Whole Cell Volume
Animal
Cell
Sham
Contra (PNI)
On MN (PNI)
Death Cluster
C
Hedges' g
p=0.0712 166.7%
p=0.0030 333.3%
p=0.0540 433.3%
p=0.0140 62.5%
p=0.5428 23.1%
Sham - Contra
Sham - On MN
Sham - Death Cluster
Contra - On MN
On MN - Death Cluster
D
Nuclear trem2
Nuclear mRNA Volume/ Microglia Nuclear Volume
E
Process trem2
Process mRNA Volume/ Microglia Process Volume

Figure 4. *trem2* mRNA expression is highest in activated microglia regardless of sub-phenotype at 14 days post-injury. A) High magnification single plane confocal images from detection of *trem2* mRNA (magenta, RNAscope) in CX3CR1^{eGFP} microglia (green, immunocytochemistry amplified eGFP) with DAPI (blue) delineating nuclei. Microglia, *trem2*, and nuclei were reconstructed in IMARIS and analyzed as volumetric 3D objects. **B**) Occupancy of total *trem2* mRNA signal in the eGFP microglia volume including cell body, processes and nucleus (Total *trem2*). Individual microglia (Cell) and animal (Animal) averages are presented (n=10 microglia per animal per condition, N=4 sham (equal sex), 5 cut-ligation (2 males, 3 females). Each symbol represents one animal or microglia cell with symbol shapes identifying individual animals. Mean±SD are represented. For simplicity only statistical comparisons from Dunn's post hoc multiple comparisons for Cell data shown (**p<0.01, ***p<0.001, ****p<0.0001) (see **Supplemental Statistical Table 4** for further details). **C**) Total *trem2* comparison in animal data using estimation statistics. Cumming estimation plot of Hedges' g estimates from bootstrap sampling distributions. Black dots represent estimates average g and vertical bars 95% confidence intervals. Estimated percentage change and significance from permutation t-tests indicated in each comparison. Animals' values for DC microglia bootstrapping were affected by a low n (n=3). All other comparisons confirm results in B. **D**) Analysis of *trem2* in nuclei delimited by DAPI. No significant differences were detected Cell comparison: Kruskal-Wallis p=0.0501; Animal comparison: One-way ANOVA p=0.8716, (**Supplemental Statistical Table 5** for details). **E)** Same analyses as in B and D for *trem2* in microglia processes. The conclusions in processes mirror total *trem2* data. Dunns comparison on Cells indicated **p<0.01, ***p<0.001, ****p<0.0001 (see **Supplemental Statistical Table 6** for details).

Figure 5

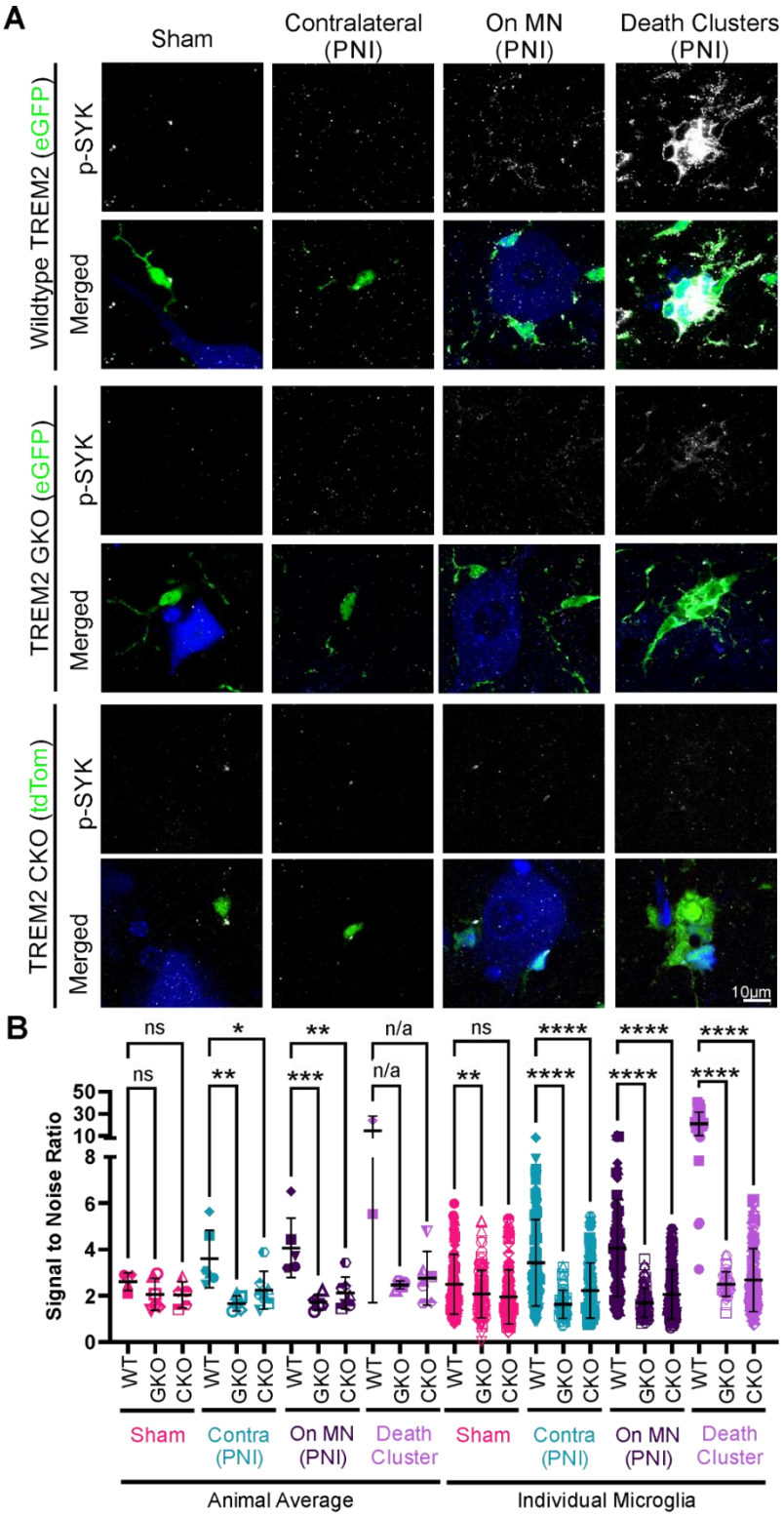
A
Sham
Contralateral (PNI)
On MN (PNI)
Death Clusters (PNI)
Wildtype TREM2 (eGFP)
TREM2 GKO (eGFP)
TREM2 CKO (tdTom)
p-SYK
Merged
10µm
B
Signal to Noise Ratio
ns
*
**
n/a
****
WT
GKO
CKO
Sham
Contra (PNI)
On MN (PNI)
Death Cluster
Animal Average
Individual Microglia

Figure 5. Phospho-SYK (p-SYK) increases with microglia activation 14 days post-cut-ligation and is diminished by TREM2 Knock Out. A) High magnification single plane confocal images of microglia close to retrogradely labeled Fast Blue (FB) motoneurons (MNs) in sham mice or On MN and DC microglia in PNI mice. Microglia in the contralateral lamina IX of PNI mice are also shown. Top rows correspond to p-SYK immunolabeling (white), and lower rows show in addition, genetically labeled microglia (green) and FB+ MNs (blue). In wildtype (WT) and GKO microglia genetic labeling corresponds to Tmem119^{eGFP}. In conditional KO (CKO) mice, genetic labeling is tdTomato (Tmem119^{creERT2}:: Ai9 R26-lsl-tdTomato). For consistency, all microglia are pseudocolored green. p-SYK immunolabeling increases in activated microglia and more so in DC microglia. This reaction is suppressed in GKO and CKO mice. **B**) Quantification of p-SYK on microglia surfaces normalized to background (signal-to-noise ratio). Animal averages at left (each data point is one animal average) and Cell averages at right (each data point is one individual microglia) show p-SYK depletions in GKO and CKO mice, particularly in activated microglia. One-way ANOVAs followed by Bonferroni pairwise comparisons were used to compare animal averages. Individual microglia Cell data was compared by Kruskal-Wallis followed by Dunn tests (n=17-20 microglia per condition per animal, N=4 WT female sham, 6 WT cut-ligation (equal sex), 6 GKO sham (4 males, 2 females), 5 GKO cut-ligation (3 males, 2 females), 5 CKO sham (2 males, 3 females), 7 CKO cut-ligation (4 males, 3 females). Significance reported for each pairwise comparison: *$p<0.05$, **$p<0.01$, ***$p<0.001$, ****$p<0.0001$; no comparisons were performed for Death Cluster animal averages because low n in WTs (n/a). Details can be found in **Supplementary Statistical Table 7**.

Figure 6

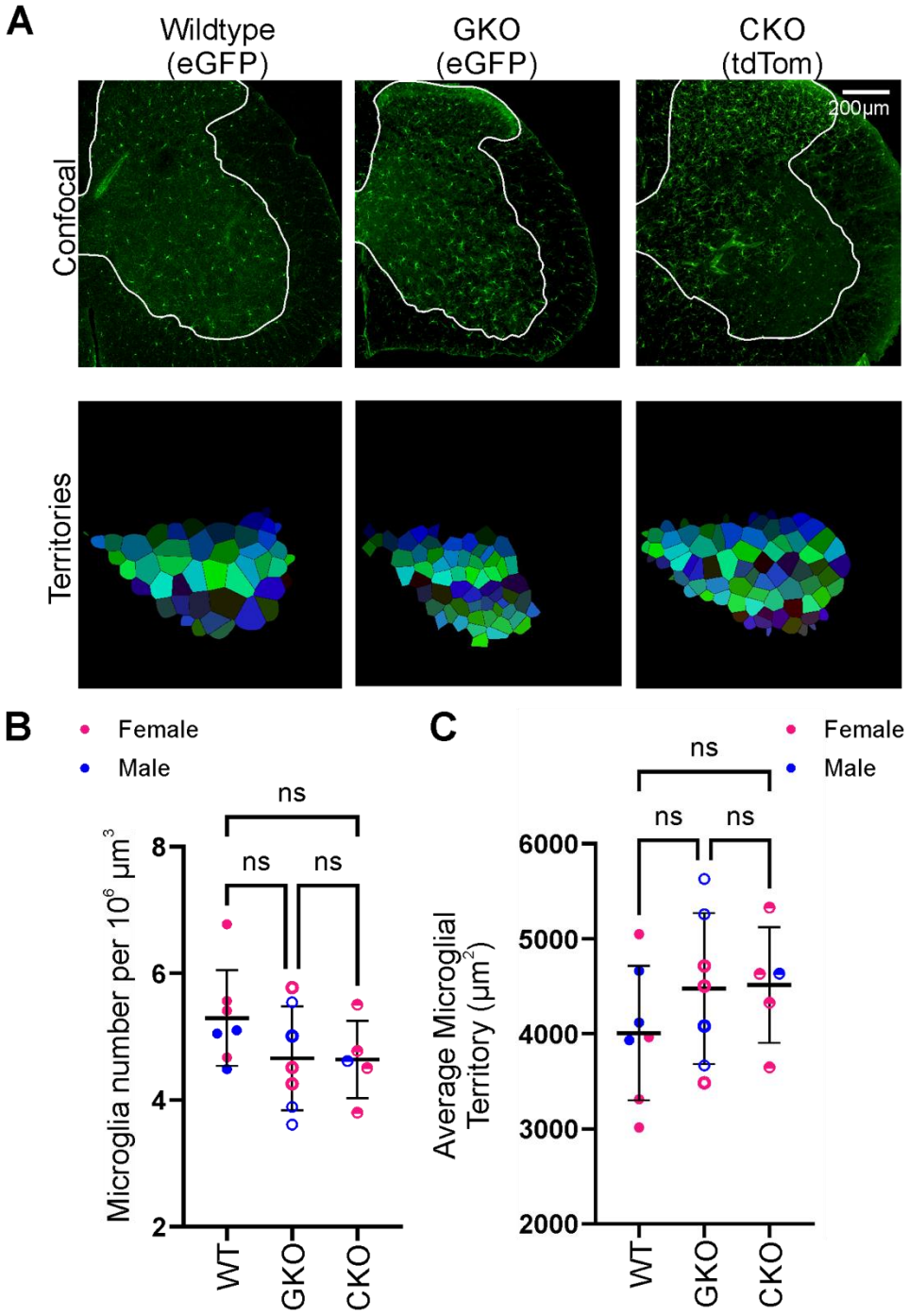

Figure 6. TREM2 knockout (KO) does not affect microglial numbers or their territories in sham controls. A) Representative low magnification collapsed z-stack confocal images (50 µm thick sections) from Tmem119 ^{eGFP} "wildtype" (WT), Tmem119^{eGFP} TREM2 global KO (GKO), and conditional Tmem119^{CreERT2} td-Tomato microglia conditional KO (CKO) (microglia all in green for consistency). All animals had sham surgery. The grey matter is outlined in white. Each ventral horn microglia soma was selected as an ROI and used for Voronoi analysis in ImageJ to identify

microglia territories shown below. The territory colors are arbitrary and only used to aid in individual territory distinction. **B**) Number of ventral horn microglia per ventral horn 100 μm side cube-volumes (10^6 μm^3) did not change in TREM2 GKO or CKO. Each dot represents one animal. Mean±SD indicated. Each animal estimated though 5 sections from the Lumbar 5 segment. N=7 mice for WT and GKO, N=5 for CKO. Red, females; blue, males. One-way ANOVA failed to detect significance (p=0.2246). Post-hoc Bonferroni tests are indicated in the figure (ns=non-significant). **C**) Same analyses for territories. No significant differences were detected by One-way ANOVA (p=03068) followed by pot-hoc Bonferroni tests (ns in graph). Details of statistical parameters in **Supplementary Statistical Tables 8 and 9**.

Figure 7

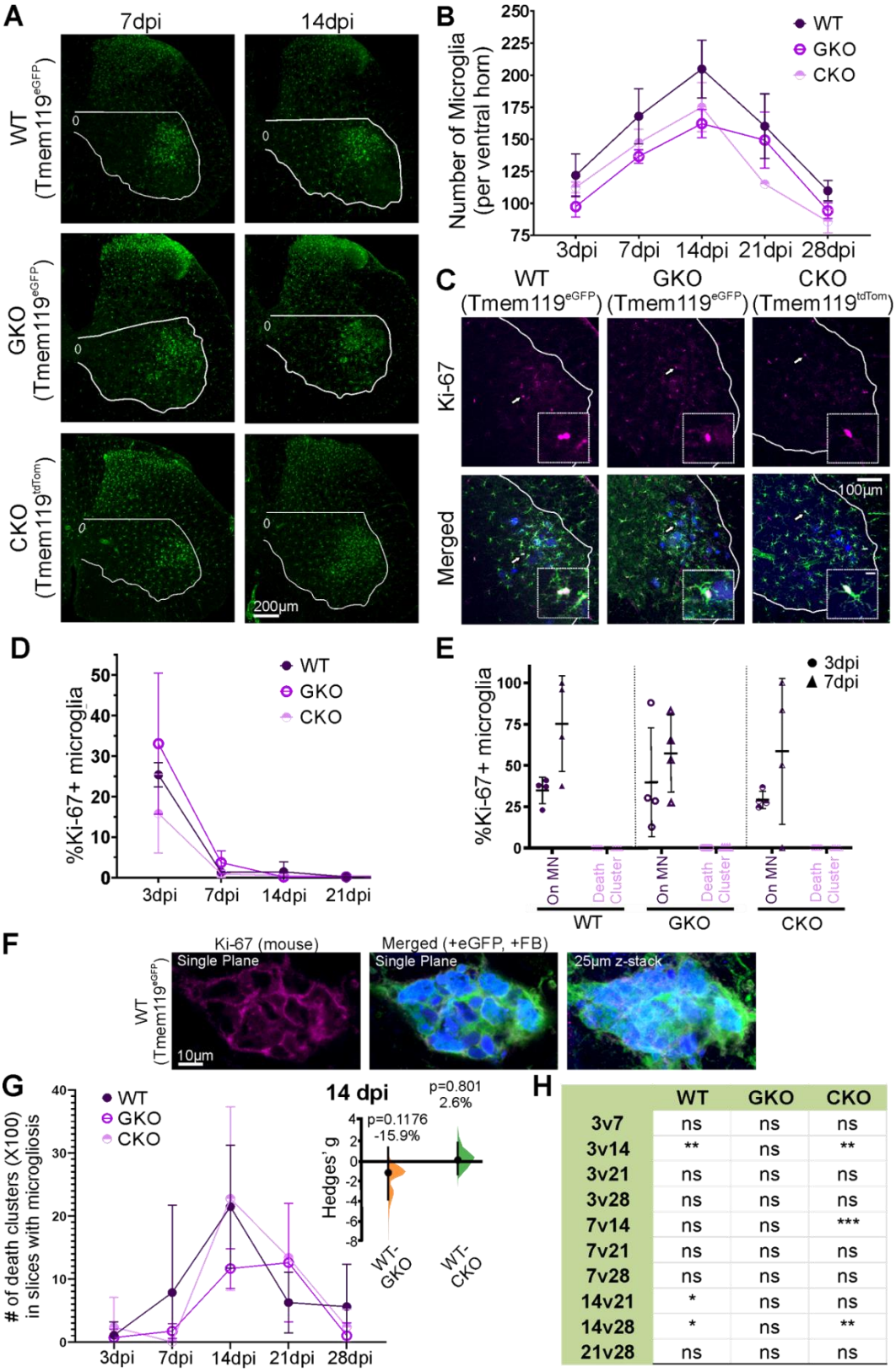

	WT	GKO	CKO
3v7	ns	ns	ns
3v14	**	ns	**
3v21	ns	ns	ns
3v28	ns	ns	ns
7v14	ns	ns	***
7v21	ns	ns	ns
7v28	ns	ns	ns
14v21	*	ns	ns
14v28	*	ns	**
21v28	ns	ns	ns

Figure 7. TREM2 Knockout (KO) does not significantly alter the time course of proliferation or the total number of ventral horn microglia. A) Confocal image stacks of lumbar 5 sections (50 µm thick) from WT, GKO, and CKO mice with genetically labeled microglia amplified with immunohistochemistry against fluorescent reporter proteins (eGFP for WT and GKO and tdTomato for CKO, all shown in green). White outlines label the ventral horn and the central canal. **B**) Average total number of grey matter ventral horn microglia in WT, GKO, and CKO at different times post-injury. Error bars=SEM. N=4 mice (equal sex) for each time point genotype, except 21 dpi CKO in which N=2, both females. Each animal estimate was obtained from five Lumbar 5 sections. Two-way ANOVA revealed statistical significance according to time after injury ($p<0.0001$) and genotype ($p=0.0157$), although post-hoc Bonferroni tests did not detect significances across genotypes at any time point. Details in **Supplementary Statistical Table 10**. **C**) Similar 2D projections confocal images showing immunolabeling for Ki-67 (white), microglia (green), and Fast Blue motoneurons (MNs) in WT, GKO, and CKO mice at 3dpi. White arrows point to Ki-67+ microglia examples featured in the zoomed-in images (white squares). **D**) Percent of total ventral horn microglia that are Ki-67+ at different times post-injury in the three genotypes. Error bars=SD. Sample sizes as in A. Two-way ANOVA revealed significant differences according to time after injury ($p<0.0001$) but not genotypes ($p=0.1156$). Details in **Supplementary Statistical Table 11**. **E**) Location of ventral horn Ki-67+ microglia at 3 and 7 dpi in each genotype. Ki67 is not expressed by DC microglia, and On MN microglia express more Ki-67 at 7 than 3 dpi in all three genotypes. TREM2 GKO or CKO did not change this pattern. Error bars=SD. **F**) DC microglia in a WT show no nuclear Ki-67+ labeling (magenta). Microglia are genetically labeled in Tmem119^{eGFP} mice (green). Fast Blue originates in the degraded MN underneath. Ki-67+ labeling is apparent on microglia membranes but likely represents binding of this mouse monoclonal antibody to Fc receptors upregulated in activated microglia. **G**) Number of death clusters at different post-injury times in WT, GKO, and CKO mice. The count represents all death clusters identified throughout the lumbar enlargement (Lumbar 1 to 6) divided by the number of sections analyzed and multiplied by 100. Error bars=SEM. Sample as in A. Two-way ANOVA detected significant differences according to time after injury ($p<0.0001$) with numbers peaking at 14 dpi, but not significant differences according to genotype ($p=0.3989$). Estimation statistics confirmed a lack of significant differences (Hedges' g comparisons shown for the 14dpi time point). **H**) Results of Bonferroni post-hoc comparisons for time after injury in each genotype; *$p<0.05$, **$p<0.001$, ***$p<0.001$. Details in **Supplementary Statistical Table 12**.

Figure9

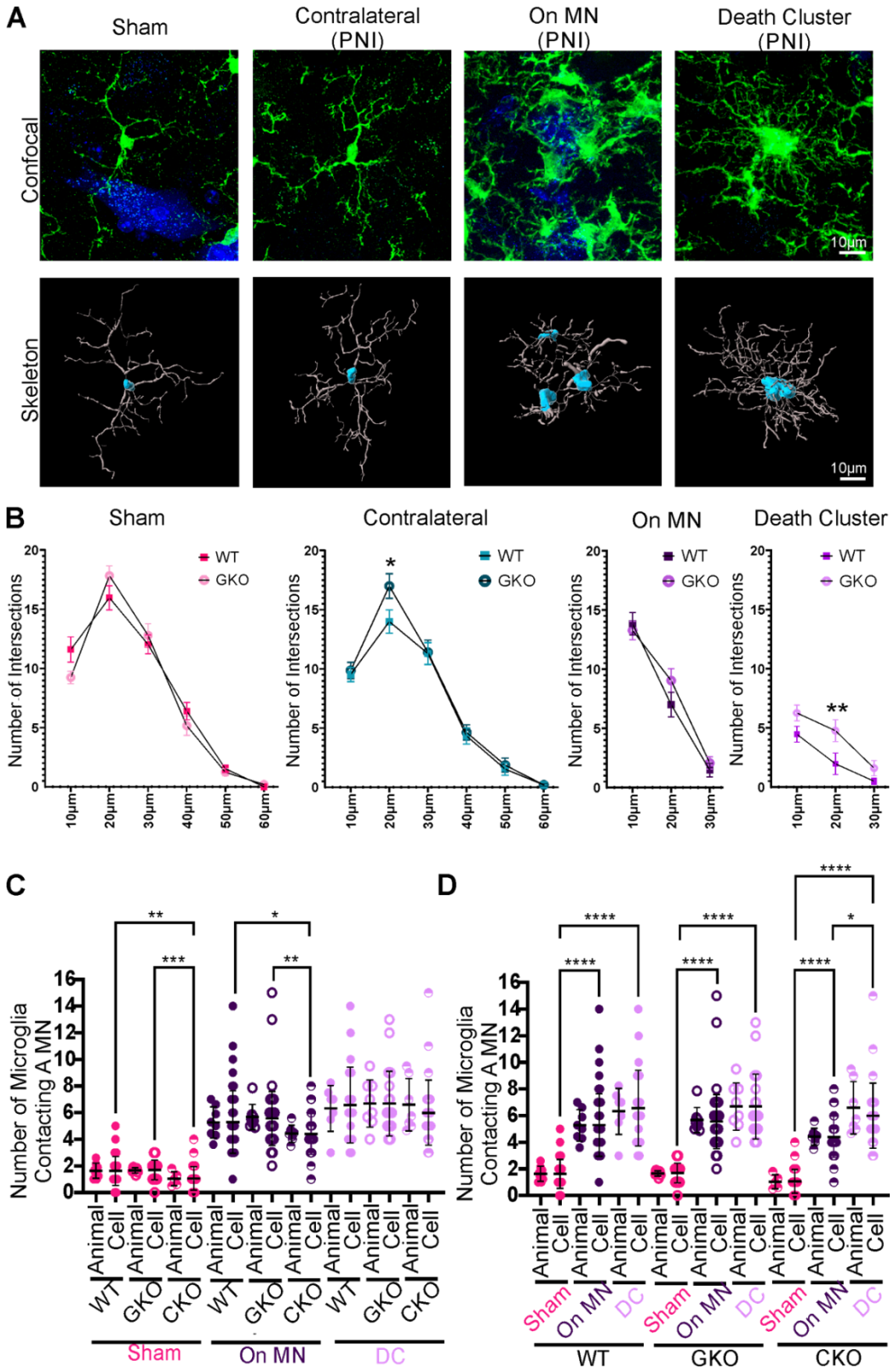
A
Sham
Contralateral (PNI)
On MN (PNI)
Death Cluster (PNI)
Confocal
Skeleton
10µm
B
Sham
Contralateral
On MN
Death Cluster
WT
GKO
Number of Intersections
10µm
20µm
30µm
40µm
50µm
60µm
C
Number of Microglia Contacting A MN
Animal
Cell
WT
GKO
CKO
Sham
On MN
DC
D
Number of Microglia Contacting A MN
Sham
On MN
DC
WT
GKO
CKO

Figure 8. Morphology of activated microglia in TREM2 Global Knockout (GKO) 14 days post-cut-ligation. A) Top row: 2D projections of confocal image z-stacks of Fast Blue MNs and microglia (green) in either surveying (sham and contralateral) or activated states (On MN and DC microglia). Bottom row: semi-automatically skeletonized microglia for Sholl analyses. **B**) Sholl analysis showed a small difference in DC microglia in the 20 µm bin (**p<0.01, Bonferroni post-hoc comparison WT vs GKO). Error Bars=SEM (pooled Cell data n=30 per genotype; n=5 microglia per condition per animal, N=6 mice (equal sex) per condition). **Supplementary Statistical Table 13. C,D)** Number of microglia in death clusters or contacting MNs in sham or injured mice, organized by microglia type in C or genotype in D. Animal and Cell data mean±SD. N=8 sham and 8 injured in WTs, 7 sham and 8 injured in GKO, and 5 sham and 7 injured in CKO. 10 MNs analyzed per animal for sham or On MN microglia; after removing outliers n=75,77 MNs for sham and On MN in WTs, n=69,67 in GKO, n=48,68 in CKO. Death cluster sampling was n=33, 22, and 29 in WT, GKO, and CKO. One-way ANOVAs (Animal data) and Kruskal-Wallis (Cell data) showed significant differences according to microglia location in WT, GKO, and CKO mice (p<0.0001 in all cases, Dunn's post-hoc comparisons for Cell data indicated in panel D). Comparisons across genotypes (panel C) revealed differences in sham and On MN in Cell data (p=0.0002, p=0.0017) but not in Animal data, which was underpowered (p=0.0635, p=0.0577). The number of microglia forming death clusters did not change in the three genotypes (p=0.9236 one-way ANOVA on Animal data and p=0.5729 Kruskal-Wallis on Cell data). Asterisk for Dunns pair-wise comparisons; *p<0.05, **p<0.001, ***p<0.001, ****p<0.0001. Further details in **Supplementary Statistical Table 14.**

Figure 9

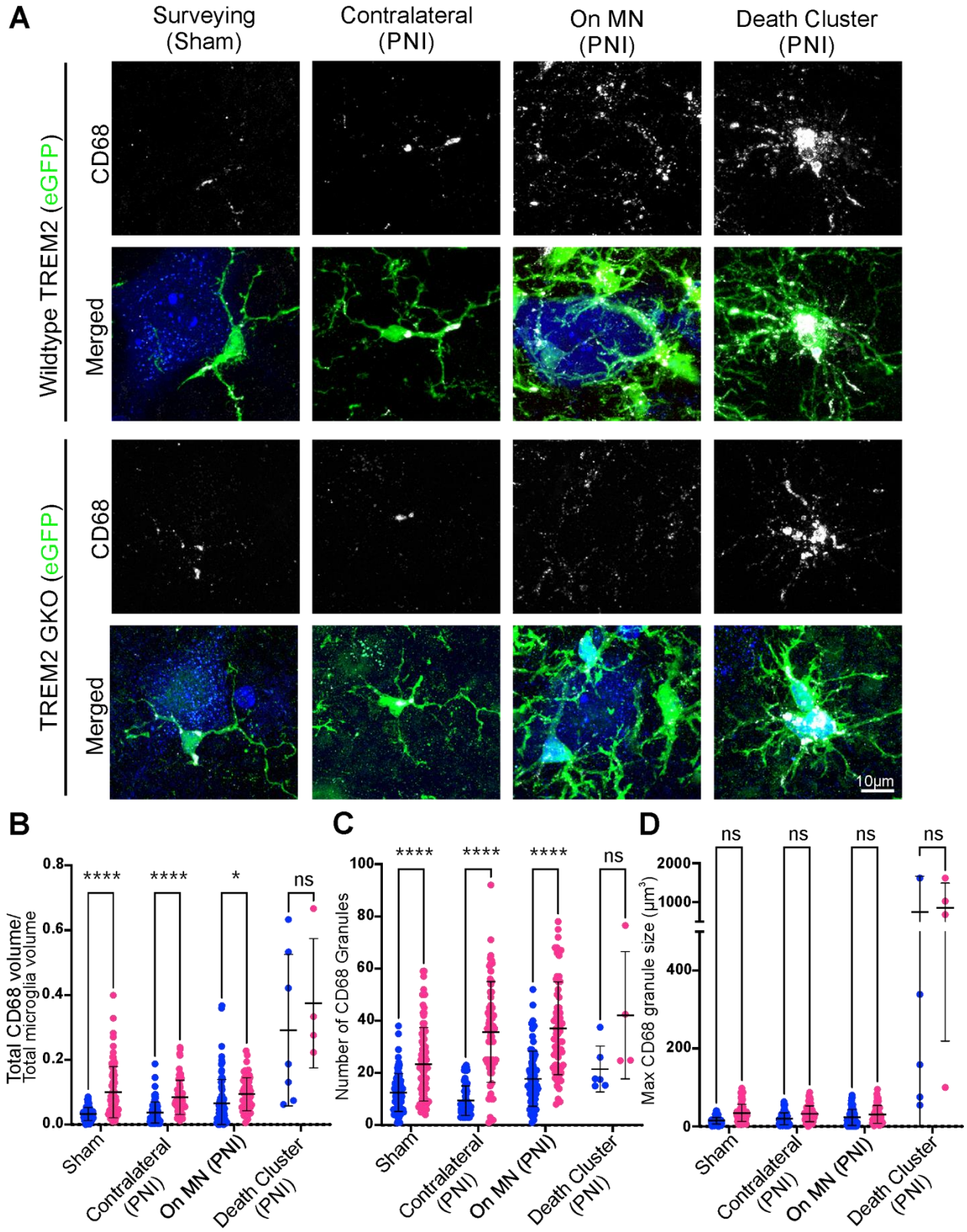
A
Surveying (Sham)
Contralateral (PNI)
On MN (PNI)
Death Cluster (PNI)
Wildtype TREM2 (eGFP)
CD68
Merged
TREM2 GKO (eGFP)
CD68
Merged
10µm
B
Total CD68 volume/ Total microglia volume
****
****
*
ns
Sham
Contralateral (PNI)
On MN (PNI)
Death Cluster (PNI)
C
Number of CD68 Granules
****
****
****
ns
Sham
Contralateral (PNI)
On MN (PNI)
Death Cluster (PNI)
D
Max CD68 granule size (µm³)
ns
ns
ns
ns
Sham
Contralateral (PNI)
On MN (PNI)
Death Cluster (PNI)

Figure 9. CD68 expression in microglia before and 14 days after injury and sex differences. A) High magnification confocal image z-stacks of microglia and Fast Blue (FB) MNs in WT and GKO mice after sham or injury (sciatic cut-ligation). Top rows CD68 immunolabeling (white); lower rows added genetically labeled microglia (green) and FB+ MNs (blue). CD68 increases in activated On MN microglia, and it is maximal in DC microglia, being reduced in GKO mice. **B,C,D**) CD68 expression sex differences. Sham surgeries mice: N=4 male and 4 female WTs and 4 males and 3 females GKOs. Nerve surgeries mice: N=4 male and 3 female WTs and 4 males and 4 females in GKO mice. 20-26 microglia sham, contralateral, and On MN analyzed per animal. After removing outliers n's ranged from 61 to 91 for each experimental group. DC microglia recovered at lower rates with n's between 4 and 13. Details in **Supplemental Statistical Table 15**. **B**) Total CD68 to microglia volume ratios. Two-way ANOVA for microglia type and sex on all microglia pooled (Cell data) detected significance for both ($p<0.0001$). Bonferroni pair-wise tests significance indicated *$p<0.05$, ****$p<0.0001$ and confirmed by estimation statistics (**Supplemental Statistical Table 16**). Except for DC microglia, females had higher CD68 content. **C**) Number of CD68 granules. Two-way ANOVA for microglia type and sex detected significance for both ($p<0.0001$). Bonferroni pair-wise test significance indicated, ****$p<0.0001$. Higher numbers of CD68 granules in sham, contralateral, and On MN female microglia were confirmed with estimation statistics. Sex differences in DC microglia did not reach significance with Bonferroni tests ($p=0.0555$) but did with estimation permutation t-tests ($p=0.0452$) (**Supplemental Statistical Table 16**). **D**) Maximum size of the largest CD68 granule measured in each microglia. Two-way ANOVA for type of microglia and sex detected significance for microglia type ($p<0.0001$) but not sex ($p=0.0504$). Post-hoc Bonferroni comparisons did not detect significance (ns). However, estimation permutation t-tests detected small but significant differences with females expressing larger granules in surveying microglia (sham and contralateral, both $p<0.0001$, $g=1.2$ and 0.7 respectively) and On MN microglia ($p=0.034$, $g=0.4$), but not in DC cluster microglia ($p=0.854$).

Figure 7

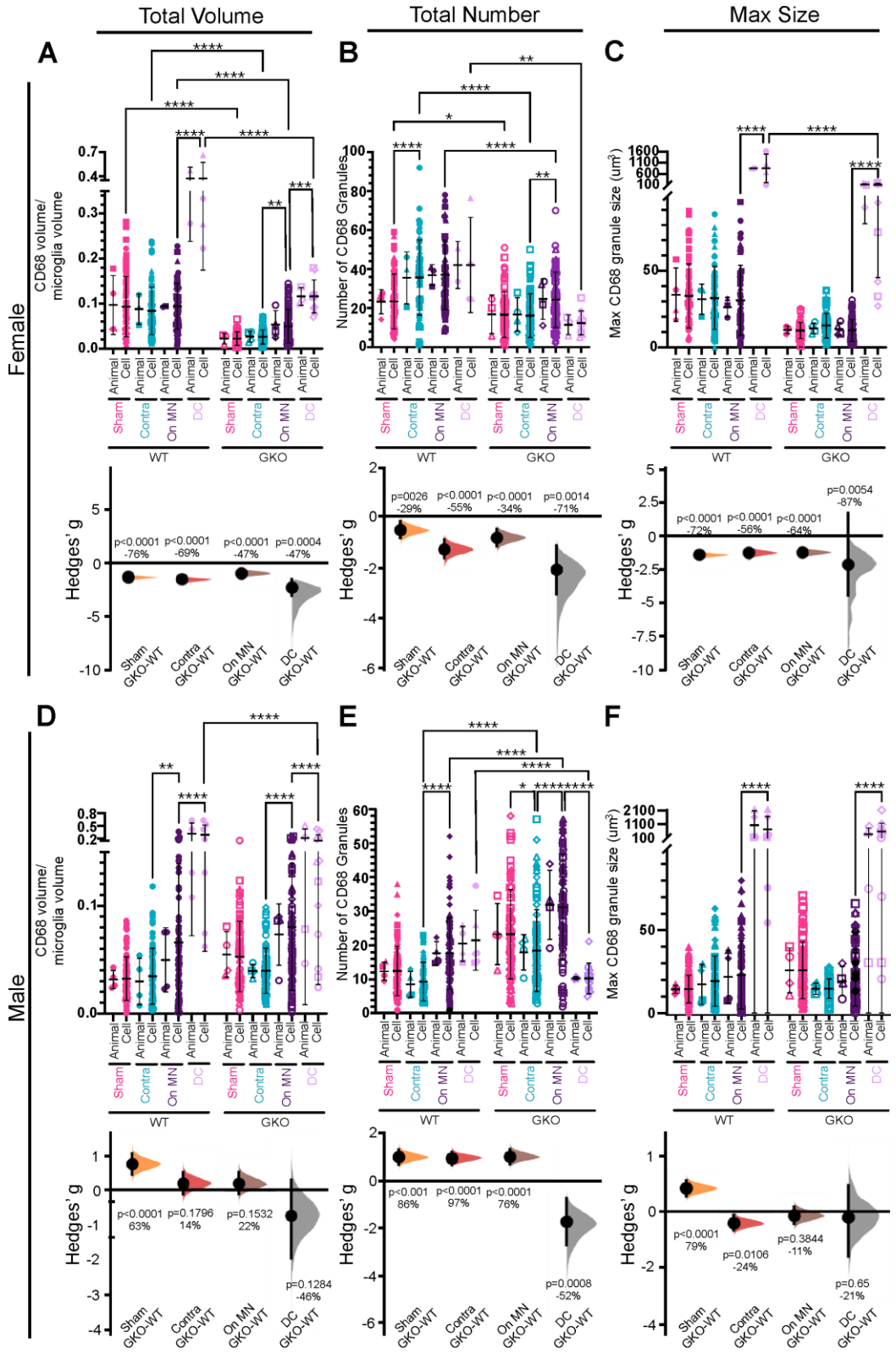
Total Volume
Total Number
Max Size
A
B
C
D
E
F
Female
Male
CD68 volume/ microglia volume
Number of CD68 Granules
Max CD68 granule size (um²)
Hedges' g
Animal
Cell
Sham
Contra
On MN
DC
WT
GKO
Sham GKO-WT
Contra GKO-WT
On MN GKO-WT
DC GKO-WT
p<0.0001 -76%
p<0.0001 -69%
p<0.0001 -47%
p=0.0004 -47%
p=0026 -29%
p<0.0001 -55%
p<0.0001 -34%
p=0.0014 -71%
p<0.0001 -72%
p<0.0001 -56%
p<0.0001 -64%
p=0.0054 -87%
p<0.0001 63%
p=0.1796 14%
p=0.1532 22%
p=0.1284 -46%
p<0.001 86%
p<0.0001 97%
p<0.0001 76%
p=0.0008 -52%
p<0.0001 79%
p=0.0106 -24%
p=0.3844 -11%
p=0.65 -21%

Figure 10. CD68 expression in different microglia types in wildtypes and TREM2 global knockouts before and after nerve injury. A,B,C) Female mice data for total CD68 volume, number of CD68 granules and maximum CD68 granule size. Top graph shows the "Animal" and "Cell" data (mean±SD) and the results of two-way ANOVAs for type of microglia and genetics in Cell data. Asterisks, *p<0.05, **p<0.001, ***p<0.001, ****p<0.0001 for post-hoc Bonferroni tests. Bottom graphs: estimation statistics, Hedge's g estimates of mean differences between WT and TREM2 GKO in all four microglia categories represented by Cumming plots with bootstrap sampling distributions. Dots show mean g estimates; vertical error bars are 95% confidence intervals. Percentage differences and significance (permutation t-tests) are indicated on each graph. Sample as in Figure 9B and summarized in **Supplemental Statistical Table 15. D,E,F**) Same as above, but for male mice. Summary results: female TREM2 GKO mice show significantly lower CD68 expression compared to WTs in all three parameters studied (total volume, number, and maximum size of CD68 granules) and in all microglia: surveying (sham and contralateral) or activated (on MN and DC microglia). Male mice did not show consistent significant differences, except for the increase in the number of granules in TREM2 GKOs in sham, controls, and On MN microglia. Details of two-way ANOVAS, Bonferroni tests, Hedges' g estimates, and permutation t-test are found in **Supplementary Statistical Tables 17, 18, 19 and 21** and the manuscript text.

Figure 11

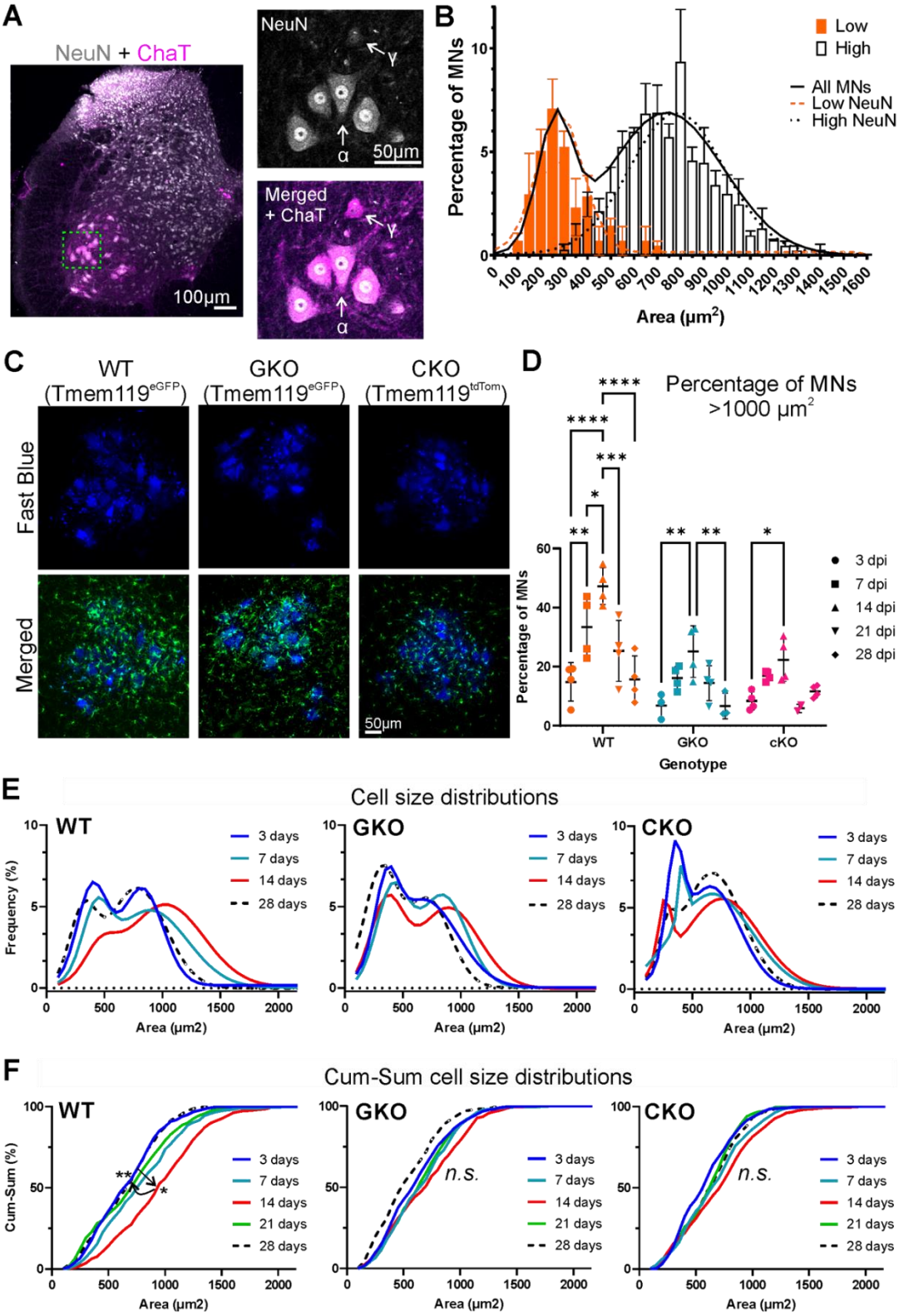
A
NeuN + ChaT
100µm
NeuN
γ
α
50µm
Merged
+ ChaT
γ
α
B
Percentage of MNs
Low
High
All MNs
Low NeuN
High NeuN
Area (µm²)
C
WT
(Tmem119eGFP)
GKO
(Tmem119eGFP)
CKO
(Tmem119tdTom)
Fast Blue
Merged
50µm
D
Percentage of MNs
>1000 µm²
Percentage of MNs
3 dpi
7 dpi
14 dpi
21 dpi
28 dpi
WT
GKO
cKO
Genotype
E
Cell size distributions
WT
GKO
CKO
Frequency (%)
3 days
7 days
14 days
28 days
Area (µm2)
F
Cum-Sum cell size distributions
WT
GKO
CKO
Cum-Sum (%)
3 days
7 days
14 days
21 days
28 days
n.s.
Area (µm2)

Figure 11. Effects of TREM2 deletion on the cell volume changes of regenerating motoneurons. A) Low magnification confocal image of NeuN immunoreactive neurons (grey) and ChAT-immunoreactivity (magenta). The boxed area on the left is magnified to show NeuN and NeuN merged with ChAT. α-MNs are ChAT+ and NeuN+; γ-MNs are ChAT+ and NeuN(-). **B**) cells distribution histogram in 50 μm^2 bins (N=3 animals. Bars indicate mean ±SEM). Continuous lines are the bimodal Gaussian fit to all MNs (n=436 MNs). The dashed curves represent fits to low NeuN MNs (n=146) and high NeuN MNs (n=290). Data details in **Supplemental Statistical Table 22**. **C**) Examples of the Fast Blue-labeled sciatic motor pools in WT, GKO, and CKO with microglia genetically labeled. **D**) Percentage of MNs with cross-sectional areas larger than 1000 μm^2. The large increase noted at 24 dpi in WTs is blunted in GKO and CKO mice. Each dot represents one animal (in this analysis, we discarded one data point from one GKO at 3 days because it was an outlier). Mean percentage ±SD is represented. Two-way ANOVA for time after injury (dpi) and genotype showed significance for both ($p<0.0001$). Bonferroni pair-wise comparisons are shown for time after injury in each genotype. *$p<0.05$, **$p<0.001$, ***$p<0.001$, ****$p<0.0001$. Statistical details and comparisons between genotypes at each time point are in **Supplemental Statistical Table 5. E**) Gaussian fits of cell size distributions of FB+ MNs at different time points in WTs, GKO and CKO. (n=437, 504, 475, and 419 MNs in WT at 3, 7, 14, and 28 dpi; n=435, 517, 563, and 429 in GKO, same time points; n=495, 467, 525, and 468 in CKO, same time points). There is a shift towards larger cells in WTs for 3 to 14 dpi, and also a reduction in the patency of the γ-MN and α-MN peaks. Both return at 28 dpi. These changes are unclear in GKO and CKO mice. Details on fits are in **Supplemental Statistical Table 23**. **F**) Cumulative plots of the same data compared with the Kolmogorov-Smirnov test. The shift towards larger values is apparent in WT data but not in GKO and CKO mice. Cell data distributions were significantly different only in the WT data between 3 days compared to 7 and 14 days (p=0.0150, 0.0282) and between 28 and 7 and 14 days (p=0037, p=0077). Details in **Supplemental Statistical Table 24**.

Figure 12

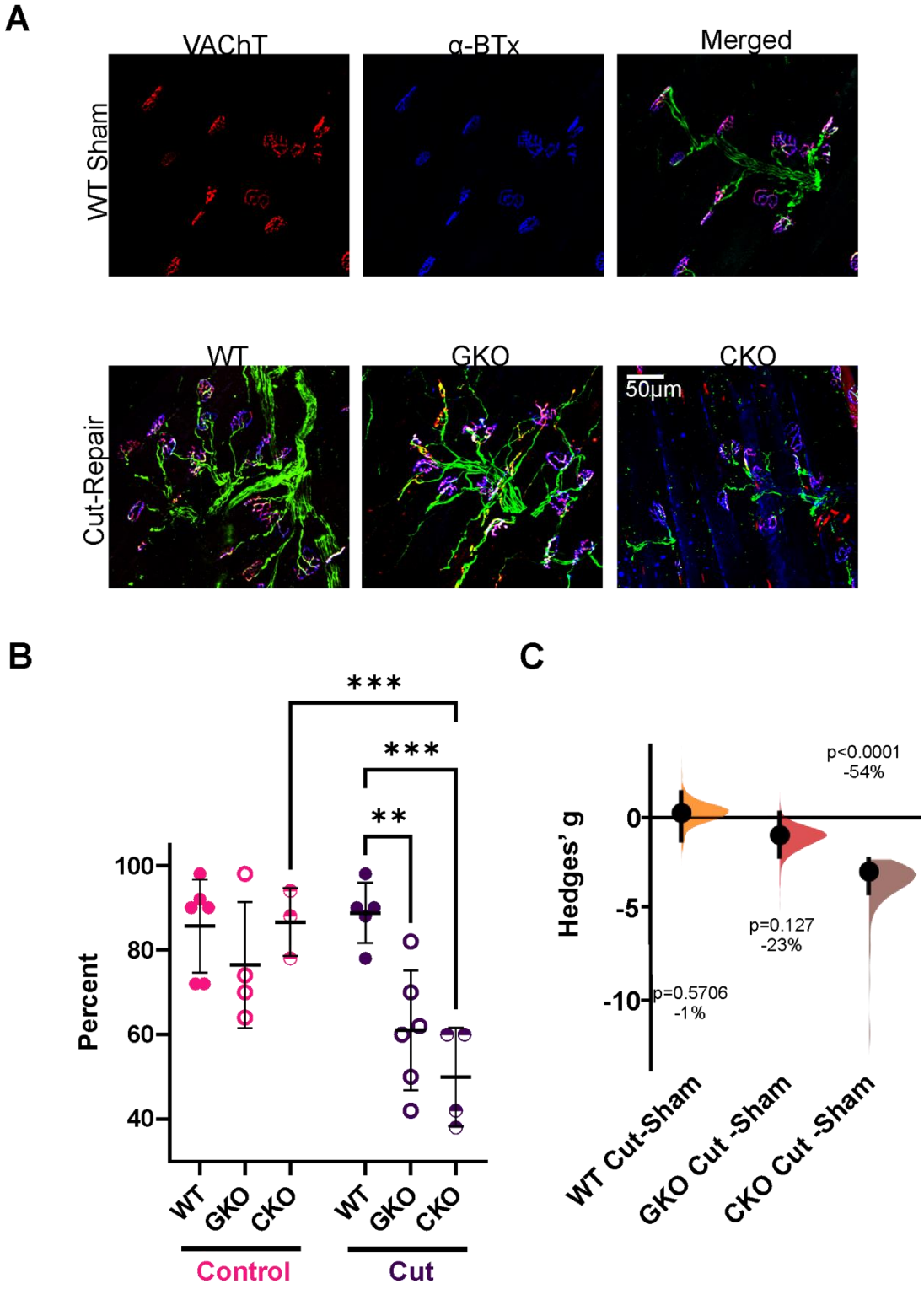

Figure 12. TREM2 deficiency reduced neuromuscular junction (NMJ) reinnervation eight weeks post sciatic cut-repair. A) Low magnification (20x/0.70 NA) confocal images of lateral gastrocnemius (LG) muscles with immunohistochemistry for Vesicular Acetylcholine Transporter

(VAChT, red) (labels axon terminals), α-Bungarotoxin (α-BTX, blue) (labels motor end plate), and Neurofilament Heavy Chain (NFH, green). **B)** The percent of fully innervated NMJs analyzed via Two-Way ANOVA with Bonferroni's post hoc multiple comparisons (each data point is one animal, n=50 per mouse, mean±SD are represented, WT vs GKO p=0.002, WT vs CKO p=0.0002, CKO control vs cut p=0.0005). **C)** NMJ innervation analyzed with estimation statistics. Hedges' g (Ho et al., 2019) of mean differences represented by Cumming plots with bootstrap sampling distributions. Dots show means; vertical error bars are 95% confidence intervals. Percentage differences and significance (permutation t-tests) are indicated on each graph.